Structured Material Generation and Chemical Handling Advancements in Microfluidic Platforms

by

Ramsey I. Zeitoun

A dissertation submitted in partial fulfillment
of the requirements for the degree of
Doctor of Philosophy
(Chemical Engineering)
in The University of Michigan
2011

Doctoral Committee:

Professor Mark A. Burns, Chair
Professor Joanna Mirecki Millunchick
Professor Michael J. Solomon
Associate Professor Joerg Lahann

dedicated to my family and friends

ACKNOWLEDGEMENTS

This Ph.D. and thesis represents the conclusion of my formal education and has been built from a culmination of what I have learned from my past 27 years. Although my education will continue until I am underground, I recognize completing my formal education as a significant accomplishment that I am proud of, and I am grateful to have experienced this. It is important to me to acknowledge the people that both supported me through this process and made it possible, and I will briefly touch on that here.

I would like to acknowledge my adviser, Professor Mark Burns for teaching me so much these past 5 years. I specifically appreciate him for his patience, for giving me the opportunity to explore interesting academic ideas and for giving me room to grow as intellectually and personally. He has many traits that I hope to take with me as I go forward in my life. I want to acknowledge two Professors I greatly academically respect: Professor Suljo Linic, with his academic competitiveness and Professor Ron Larson, who I believe truly embodies what it means to be an academic. Thank you to Mr. Narendar Dhallan, who first showed me that learning can actually be fun. I still seek his invaluable guidance and he acknowledge that he helped put me on a path that I am happy with both as a person and as an academic. Through research, I had the opportunity to collaborate with Thomas Westrich, and wanted to thank him for his optimistic personality, collegiate attitude and for being a great person to work with. I also had the pleasure to work with three undergraduates during my time here that added substantially to the project detailed in Chapter 2. These are Marcus

Goudie, Jacob Zwier and David Mahawili. Thank you for doing such an amazing job. Especially thank you Marc, if you decide to go through graduate school you are going to do a great job. Finally, thank you to my research group members and officemates for making it a pleasure to come into work and for teaching me so much. I especially include Irene Sinn, Dustin Chang, Brian Johnson, Jihyang Park, Eric Livak-Dahl, Jaesung Lee, Fang Wang, Alissa Kerner and Colin Jennings.

A few peers of mine fall into that category that I must acknowledge both personally and academically. These are people that I respect on many facets, have grown from by knowing and hope to have their guidance in the future. Most notably, I had the pleasure of being roommates with future Professor Phil Christopher for four of my five years here. To be brief, I gained so much from my interaction with Phil both on an academic and social level that it redefined me as a person here and made the experience all the more thorough. Academically and professionally, I believe that my interactions with Phil were almost as important as the actual lab work I did in the Dow Building. I must thank Professor Michael Senra for so many frequent interactions and teaching me a lot about academics and myself. Also, Sean Langelier and Siris Laursen are two intelligent and genuine people that have positively influenced me knowing them.

More personally: I have had two inspiration figures in my life and want to thank them for instilling the tools I needed to succeed. These are both my father, Dr. Ibrahim Zeitoun and my grandfather the late Mr. Donald Keagle. My Dad came to America from Egypt on an academic scholarship. Coming to America with little knowledge of English put him at an initial disadvantage. His hard work, and unyielding support of his family allowed him to snag a piece of the American dream. I will always attribute making it this far, in part, because of his hard work providing me opportunities and his constant source for wisdom and guidance. My grandfather, another source of inspiration, was diagnosed with polio when he was 13, and as a

result, had an uphill battle his whole life. He never missed a day of work in 25 years to provide for his family and never complained about his disability. This meant a lot to me, because it shows that I have been put in a fortunate position in life by perseverance of others and it is my obligation to work hard. By moving to Michigan I also been very fortunate to get to know my Grandfather on a more personal basis during the last years of his life. Thank you both.

My family has been supportive of me. My mother, Elaine Keagle, always supported me in everything I tried growing up, and made sure I was raised to be a polite and responsible individual. My sister, Amalie, has always been someone I competed with growing up and someone who always, without a doubt, been there for me no matter what. It meant a lot to me and wanted to deeply thank you both. In Michigan, I have also been close to family members including the late Ellen Keagle and Cheryl, Robert, Betsy, Stephanie and Cara Brewer. Both morale support and support in terms of weekly dinners at the Brewer's house have meant a lot to me and I will fondly reflect on these times and not soon forget your generosity and kindness. Also, special thanks to my family members Ed, Gail, Josh and Adam Keagle. Your support always means a lot to me. Especially Josh Keagle, growing up I always looked up to you and continue to do so.

I'd like to thank the friends I've had over the years for their support. Especially to my closest friends from high school and undergrad. Eby Kalantar, Blake Mease, Dr. Eric Shpritz and Clive Butler, helped me become the person I am. I deeply respect them as people and I always feel like I am truly home with them. Thanks to Amanda Spatz for her support through undergraduate and graduate school. I want to thank people who have been supportive of me during graduate school and made Michigan such an enjoyable place. These include, but are not limited to, Tony Huff, Jeffrey Huang, John Toth, Abhishek Julka and Seema Sanghavi. I've learned a lot from knowing you, look to your for advice and genuinely respect you as people. I hope

we keep in touch as we go our separate ways. Finally, I wanted to thank Yamasaki brazilian jiu jitsu and the various Michigan brazilian jiu jitsu associations (especially Rodrigo Nunes, Andrew Schwartz, Tony Visco and Brandon Anes) for being a home away from home, great distraction from graduate school and for helping me grow as a person.

TABLE OF CONTENTS

DEDICATION ii

ACKNOWLEDGEMENTS iii

LIST OF FIGURES x

ABSTRACT xvi

CHAPTER

I. Introduction 1

1.1 Microfluidics: Motivation and History 1
1.2 Microfluidic Traits 2
1.3 On-Chip Chemical Handling 4
1.4 Microfluidics for Complex Structures 5
1.5 Organization of this Dissertation 6

II. Control of Mass Transport to Nanoliter Droplets using Separated Convective Signal Flows 8

2.1 Introduction 8
2.2 Materials and Methods 10
2.2.1 Device fabrication 10
2.2.2 Droplet generation 10
2.2.3 Droplet size experiments 10
2.2.4 Water in Oil Concentration 11
2.2.5 COMSOL Simulations 11
2.2.6 Colloidal Crystallization 11
2.2.7 Chemical Functions 12
2.2.8 Small Molecule Delivery 12
2.3 Results and Discussion 12
2.3.1 Device Design 12
2.3.2 Basic Droplet Functions 13

2.3.3 Combined Operations 15
2.3.4 Mass Transport Analysis 16
2.3.5 Particle Packing 25
2.3.6 Chemical Processes 26
2.3.7 Transport of Small Molecules 30
2.4 Conclusions 30

III. Transverse Migration of dsDNA in Microchannel Gel Electrophoresis 32

3.1 Introduction 32
3.2 Materials and Methods 33
3.2.1 Microchannel Etching 33
3.2.2 Device Assembly 34
3.2.3 Channel Treatment 36
3.2.4 Gel Preparation 36
3.2.5 Sample Preparation 37
3.2.6 LabVIEW^{TM} Controlled Injection and Electrophoresis 37
3.2.7 Detection with Confocal Microscopy 38
3.2.8 Image Process and Data Analysis 38
3.2.9 Simulation of dsDNA Movement 38
3.3 Results and Discussion 39
3.3.1 Observation of Non-Uniform DNA Distribution . . . 39
3.3.2 Factors Influencing DNA Distribution 41
3.3.3 Simulation of DNAs Transverse Movement 43
3.4 Conclusion 47

IV. Selective Arraying of Complex Particle Patterns 49

4.1 Introduction 49
4.2 Materials and Methods 50
4.2.1 Device Fabrication and Construction 50
4.2.2 Fluidic Setup 53
4.2.3 FEM Simulations 53
4.2.4 Cell Culturing and Monitoring 54
4.3 Results and Discussion 54
4.3.1 Surface Patterned Device Concept 54
4.3.2 Rapid Arraying Capabilities 56
4.3.3 Accuracy and Precision in Object Placement 60
4.3.4 Particle Bonding 61
4.3.5 Positioning Complexity 63
4.3.6 Small Particle Aggregation 64
4.3.7 Miniaturization Limits 65
4.4 Conclusion 68

V. Flows with Tunable Micro- and Nano- Structure at Short Diffusion Timescales 70

5.1 Introduction 70
5.2 Materials and Methods 72
5.2.1 Microfluidic Device Fabrication 72
5.2.2 Fluid Delivery 73
5.2.3 Computational Fluid Dynamics 74
5.2.4 Imaging 74
5.2.5 Fiber Optic Characterization 74
5.3 Results and Discussion 74
5.3.1 Three-Dimensional Architecture 74
5.3.2 Active Co-Flow Control 77
5.3.3 Uniformity 78
5.3.4 Miniaturization 83
5.3.5 Stream Quality - Diffusion 85
5.3.6 Stream Quality - Dean Flow 91
5.4 Conclusions 93

VI. Conclusions and Continuing Work 94

6.1 Conclusions 94
6.2 Continuing Work 96
6.2.1 Particle Filter to Visually Detect DNA Hybridization 96
6.2.2 Continuous Separation and Infrared Detection of Nanoliter Samples 97
6.2.3 Integrated UV/vis Fiber Optic to Stream Flows . . 98

BIBLIOGRAPHY 100

LIST OF FIGURES

Figure

2.1 Method schematics and device design. Droplets are generated in a T-junction and then move to a channel with side-streams separated by a permeable wall. 12

2.2 Basic droplet operations. a) Droplet evaporation. A is area, A_o is initial area and t is time. b) Droplet growth and dilution. Droplets are highlighted in the second image. 14

2.3 Droplet signal input and output. a) Signal-response black box system concept. b) Droplet size stabilization. A is area, A_o is initial area and t is time. Droplet size stabilization at $t = 0, t = 500$ s, and no stabilization. c) Oscillation of a droplet undergoing size reduction and growth with a time resolved signal in the second image. 16

2.4 Diagram of transport with a droplet located in the channel. (a) Top view of droplet transport (b) Side view of droplet transport. 18

2.5 Evaporation rate of water versus projected area. (a) Droplet area versus time for large droplet sizes along with a fit based on Equation 2.6. (b) Rate of change of droplet area versus droplet area. 22

2.6 Evaporation rate of water measured at several different conditions. (a) Droplet evaporation rate versus temperature at a height of 75 μm, wall width, d, of 100 μm and 50 kPa air flow. (b) Droplet evaporation rate versus channel height with a wall width, d, of 100 μm and 50 kPa air flow (c) Droplet evaporation rate versus wall width with a channel height, h, of 35 μm and 50 kPa air flow (d) Droplet evaporation rate versus air flow with a channel height, h, of 75 μm and wall width, d, of 100 μm. 26

2.7 (a) Droplet shrinking initially concentrated with 0.2 wt% particles. (b) Droplet magnified prior to full evaporation. (c) Packed particles. (d) NaCl crystal. 27

2.8 Chemical functions using signal flows. a) Aqueous silver nitrate droplets surrounded by water and with diffusing sodium chloride to precipitate silver chloride crystals. b) Salt precipitates with air in the side channels but does not with water side-channels. c) Silver chloride is soluble in ammonia hydroxide and the crystals are extracted into the droplet. 28

2.9 Silver chloride precipitate formed in the PDMS wall from silver nitrate droplets and a sodium chloride convective flow. Scalebar is 50 μm. 29

2.10 (a) Transport of rhodamine B into droplets. Flowchart of experimental procedure used to transport rhodamine B into droplets. (b) Images corresponding to the flow chart. Droplet edges are highlighted. 30

3.1 Images of the microfabricated devices used in the study of DNA electrophoresis with CLSM: (a) Design I; (b) Design II; (c) Sketch of confocal microscopy scanning mode and cross-section of microchannel with definition of coordinates: x-; y-length of the channel, z-depth of the channel. 35

3.2 DNA distribution in the cross-sectional plane of the microchannel, and its net transverse movement as a function of y-distance (detected by moving the stage along DNA migration direction in 2min). . . . 39

3.3 Images of self-diffusion induced distribution change when the electric field turned off. The first image is taken right after the turn-off of the electric field (e.g. $t_d = 0$ minutes) and each image is taken 1 minute after the previous one (e.g. the last image represents the distribution at the moment $t_d = 4$ minutes). 40

3.4 (a) Center-concentrated DNA pattern as a 150V electric field is cycles. At the first image the electric field is shut off, and half-way through the field is reapplied. (b) Variance of the images versus time. Fluorescence intensity was integrated across the width of the channel, then variance was calculated from integrated width intensity with respect to the height of the channel. The dotted line represents reapplication of the electric field. 41

3.5 Various distribution patterns of dsDNA on the cross-sectional plane corresponding to the size of DNA strands and gel type. (a) 8%T 20 bp; (b) 8%T 100 bp; (c) 8%T 343 bp; (d) 8%T 462 bp; (e) 6% linear polyacrylamide 200bp. (a-d) are taken 1 cm downstream of starting point of the electrophoresis while (e) was chosen as a representative image. 42

3.6 Distribution images of DNA migrating through both 7%T and 8%T polyacrlyamide gel. (a) 7%T 1 cm after injection (b) 8%T 1 cm after injection (c) 7%T 2 cm after injection; (d) 8%T 2 cm after injection 43

3.7 Images of 100 strands of DNA after t = 5 seconds in (a) 5 nm pores; (b) 80 nm pores; (c) 80 nm pores (10 microns on the top and bottom of the channel) and 5 nm pores (occupying the center 30 microns) . 46

3.8 (a) DNA traveling through a stratified pore system over different time-lapses (×) 5 seconds; (•) 30 seconds; (○) 120 seconds. Dotted lines represent the large and small pore interface. (b) Number change fraction of DNA in large pores (⧫) and small pores (×) versus time. 47

4.1 Fabrication diagram for both classes of devices for creating single component patterns or multi-component patterns. Both fabrication layouts begin the same with etching the high-resolution drain features. 52

4.2 Overview and operation of the multilayer microfluidic device for positioning objects. (A) Diagram of the front and back of a multilayer microfluidic device. (B) Cross sections of selected areas from Figure 4.2A. (C) Magnified cross-section of the drains from both the side view and top. The top view image demonstrates the two-dimensional drain placement. (D) Several major operational modes. In loading, flow is restricted out the outlet which a majority of flow occurs at the inlet (positive pressure) and back side (vacuum). For clearing, flow is applied at the inlet while the outlet is opened to atmospheric pressure and the vacuum is constricted. Unloading, pressure is applied at the inlet and back side, while the outlet is open to atmospheric pressure. (E) Actual device image. 55

4.3 Characterization of fluid flow and drain loading. (A) Experimental fluid flow characterization graphs of flow ratio (top side flow versus back side flow) versus applied inlet pressure. Data compared devices with and without 20 μm particles positioned. The dotted line is COMSOL simulation data of a 2D system, diagramed in 2B. (B) COMSOL simulation layout diagramming simulation conditions. Zoomed in scenario with and without particles displays a pressure surface plot, while the overall schematic is a velocity surface plot. (C) Flow ratio in two systems be constricting topside and backside flow at varying flow conditions. 57

4.4 Loading particles in a 3x3 drain structure. (A) Stereoscope image of the array device and serpentine microchannel. (B) Enlarged image of the box showing arrayed 3x3 drain formation of 5 μm drains pre-particle loading. Drains are spaced 10, 20 and 40 μm apart. (C) Drains post particle loading with 10 μm polystyrene particles. Steric particle interactions result in additionally aggregated particles in the 10 μm spaced case. (D) Graph of fraction of 10 μm polystyrene particles loaded and unloaded versus time in a 3x3 array microfluidic device with respect to the viewing window. 18 drains are imaged in the loading case, and 27 drains are imaged in the unloading case. (E) Sample loading fraction from 40 sets of drains in a 3x3 drain system. (360 drains) Scale Bars: (A) 5 mm (B,C) 40 μm. 58

4.5 Procedure for precisely positioning particles in contact. (A) Computer design of different drains. (B) Drains fabricated on a silicon substrate (C) Particles (20 μm) convectively pulled into precise positions, forming tightly packed patterns. (D) Fused 20 μm polystyrene particles including a triangle, 5-mer zig zag and a ring. (E) Loading fraction in the case with 67 5-mer drain sets (335 drains). Scale Bar: 40 μm 61

4.6 Adjacent particle coalescence d/d_p measured as a function of the temperature of the particle. Inset particle pictures correspond to filled points. 62

4.7 Methodology and demonstration of controlling particles individually. (A) Design of the front and back side of the device. (B) Cross sections of the multi-control device demonstrating the ability to individually actuate two sets of drains. (C) Zig-zag drain and ring drain with the backside (large) and topside (small) demonstrating the independent control. Arrows represent fluid actuation. (D) Still device image. Scale Bars: (A) 1 cm (B-D) Drains - 40 μm, Backside - 80 μm . . . 64

4.8 Culturing S. Ludwigii yeast cells in an alternative fluidic arrangement. A) Alternative design of an open box flow design which was used to culture cells. (B) At $t = 0$ hrs, *S.Ludwigii* cells were loaded in a 3x3 array with a box top side fluidics. All top side and back side fluidics are closed and the cells are given time to grow and culture. Time progression shows areas of cell growth and stagnation. (C) Normalized intensity of cell (*S.Ludwigii*) growth for 3 sets of drain arrays on the same run. Sets 1 and 2 are images in (B). Scale Bars: 40 μm 66

4.9 Time to drain volume based on Equation 4.5. (a) Time versus drain packing density, R. (b) Time versus drain size, d. 68

5.1 Microfabrication diagram. (a) Silicon wafer. (b) Coasted with photoresist. (c) Deep reactive ion etch deep trenches for through holes. (d) Pattern and etch top channel network. (e) Back etching channels and reaching the through holes. (f) Anodic bond glass to top channel network. (g) UV glue back of the device to glass slide. 73

5.2 Device design for interdigitating fluid streams. (a) Front and back of a silicon wafer with bifurcating channels. Through holes connect and offset channels from the front and back of the wafer. (b) Assembled device, and schematic of flow constricting from the two inlets. (c) Computational fluid dynamics simulations of flow with inlets flow and resulting flows taken at different points in the channel. Scalebar: (i) 100 μm (ii) 50 μm. 76

5.3 Device design with labelled dimensions. 77

5.4 Active flow size scalability. (a) Images of streams shrunk at different ratios of buffer flow to inlet flow. Scalebar: 50 μm. (b) Measured stream width at different flow ratios and calculated streams width. . 79

5.5 Comparison of two possible flow paths by inlet flows. 80

5.6 Uniformity of stream widths. (a) Calculated stream width uniformity. (b) Experimental stream intensity versus x-position (y-position held constant) after constriction. 82

5.7 Stream number increase and stream miniaturization. (a) Screenshot of a 64 streams device. 47 streams are shown in this image. Scalebar: 100 μm (b) Imaged constriction with flowing streams. Scalebar: 50 μm. (c) Stream showing clear structure before full miniaturization and clear structure on expansion. Scalebar: 50 μm. 84

5.8 Structured flow around a cylinder imaged with a stereoscope and color CCD camera. (a) Flow at R = 0. (b). Flow at R = 2 with magnified sections around the side of the cylinder and after passing the cylinder. Scalebar: 250 μm. 85

5.9 Sectioned and labelled device, separated into 4 quarters for separate integration to find predicted diffusion. 88

5.10 Stream quality from diffusion. (a) Images of constant sized streams blurring with decreasing flow rates and increased residence time. (b) Calculated and measured diffusion percentages for streams of varying size versus flow rate. 90

5.11 The relative effect of channel geometry on diffusion with a changing constriction angle. 91

5.12 Dean flow. (a) Images stitched together from three frames of ethanol and benzaldehyde flowing through a constriction at 240 mL/hr, with R = 2 in a 70 μm high device. Ethanol is highlighted with fluorescein. Scalebar: 50 μm (b) Curvature of the streams at R = 1. Scalebar: 50 μm (c) Decreasing flowrate with a constant R value changing the clarity of the streams as diffusion increases. 92

6.1 Bead-based array to separate and place particles based on sizes. (a) Design of particles flowing from large holes to small holes. (b) Visual readout of the system. 97

6.2 Nanoliter sample interrogation using an infrared fiber optic integrated to a microfluidic device. (a) Concepts of the device, where droplets will flow and permeate through a thin wall and contents will travel into a nitrogen channel. Between the droplet and nitrogen channel is a detection chamber which is bounded by source and detector fibers. (b) Image of the microfabricated device with fiber optics. 98

6.3 Integrated UV/vis fiber optic. (a) Image of microfabricated device with cleaved source and detector fiber placed across the path length. (b) Diagram of a sample experiment where methylene blue stream is measured based and signal is changed based on the stream width. (c) Transmission results of varying width methylene blue streams which can be predicted from the Beer-Lambert absorption law. 99

ABSTRACT

Structured Material Generation and Chemical Handling Advancements in Microfluidic Platforms

by

Ramsey I. Zeitoun

Chair: Mark A. Burns

Microfluidic technology was developed, in part, to miniaturize chemical analysis techniques. However, difficulties remain in functionality. Several microfluidic techniques were developed to enhance microfluidic functionality and study phenomena that occur in microfluidic systems.

Handling nanoliter chemical volumes in microchannels was addressed by integrating a permeable polymer wall separating nanoliter droplets, where droplet contents could actively be manipulated by diffusion. Droplets were actively manipulated through a user-defined chemical flow to deliver solvents, reagents for reactions, perform separations and dissolve solid precipitate. Transport occurring in these systems was also analyzed and characterized, and transport rates from hundreds of fL/s to pL/s were achieved.

Microscale separations of double-stranded DNA during polyacrylamide gel electrophoresis were studied in a microchannel with confocal laser scanning microscopy (CLSM), allowing DNA migration to be imaged at a plane normal to its migration direction. dsDNA displays a net transverse migration and concentrates at the top and

bottom of the polyacrylamide gel. This phenomena is analyzed and explained with both experimental results and simulations. An imhonogenous pore size is attributed to be responsible for the observed migration.

Using a three-dimensional microfabrication method, both 10 μm particles and yeast cells were positioned on microfabricated 5 μm through-holes using convective flow. This method is shown to be rapid to create accurate two dimensional patterns in around 2 seconds, and was subsequently used to fuse microparticle clusters and to cuture cells from a predefined two-dimensional pattern. The device was further expanded to be able to precisely position two particle types by independently controlling drains.

Finally, the properties of miniaturized laminar co-flows were investigated. Through-holes were used to create an alternating co-flow structure where the number of co-flowing streams could be scaled up to 64, 750 nm streams. Fluidic effects that arise and can interfere with the quality of co-flows were investigated and conclusions were drawn that are applicable to future designs. Effects that were investigated include stream uniformity caused by non-uniform path lengths, diffusion, and Dean flow caused by quickly constricting flows at high Dean numbers.

CHAPTER I

Introduction

1.1 Microfluidics: Motivation and History

Microfluidics describe a growing field involving the manipulation of femtoliter to nanoliter volumes of fluids, and the subsequent design of such microsystems to manipulate these fluids [1]. Historically, the need to manipulate small amounts of fluids grew from a desire to perform analytical measurements with small amounts of reagents more quickly and efficiently than could previously be done [2]. For instance, The Human Genome project, started in 1998, was an ambitious project to sequence the 3.3 billion base-pairs that make up the human genome [3]. This task was accomplished under-cost and ahead of time, partially because of the contribution from microseparation systems like capillary electrophoresis, where charged species are separated in a 50 μm in diameter fused silica capillary [4]. In addition to electrophoresis separations, chromatography has been theoretically and experimentally demonstrated to increase performance as size scales are miniaturized and as a result, makes up some of the earliest microfluidic separation systems [5].

As microscale analytical methods unequivocally demonstrated the advantage of microfluidic systems, the microfabriction field, which was developed for generating microelectromechanimcal systems (MEMS) was mature and had a rich base with which to create microfluidic systems. This base had developed techniques and instru-

mentation for precise glass and silicon etching to make channels, deposit thin metal films to create sensors and heaters, and other technologies to make moving parts and integrated optics [6, 7]. Microfabrication has been further exploited by microfluidic researchers through soft-lithography. Flexible polymer components are cast against microfabricated molds to create microchannels [8]. The flexible substrates have also been demonstrated to make active fluid components like valves and pumps [9].

1.2 Microfluidic Traits

Lab on a chip systems are used to miniaturize the benchtop components of a common lab (including purification, reaction, separation and detection) into a self-contained microchip [10]. By manipulating fluid on-chip, sample can remain free from outside contamination and be processed in an automated and inexpensive fashion. Some of the earliest results were simple micro total analysis systems (μTAS) where DNA was amplified, digested and separated on a fully integrated system [11]. Since then, microfluidics has been developed to create many bioanalytical tools. For instance, DNA analysis devices were developed utilizing a multitude of reactions including polymerease chain reaction (PCR) and strand displacement amplification (SDA) [12, 13]. Other systems, like nanoliter viscometers, are used to assess fluid's physical properties [14]. Chemical sensors, like immunoassays, have been developed with different detection methods, including fluorescence, electrochemical and surface plasmon resonance [15, 16]. However, simply miniturizing current reaction technologies will not generate a robust lab on a chip. These systems must be developed by accounting for many of the unique qualities present in microfluidic systems [17].

Micron length scales are fundamental to microfluidic systems and imposes a unique set of parameters on fluid and chemical operations. By understanding and utilizing these properties, microfluidic functionality can be enhanced and potential problems can be addressed [18, 19]. First, microfluidics utilize small volumes, which can re-

duce reagent costs. By decreasing the volume of an analytical reaction from 10 μL to 1 nL, the cost per reaction is reduced 10,000 times [20]. Also, with smaller volumes, transport times are decreased because the thermal mass (which is proportional to volume) of a nanoliter sample is much smaller than a microliter sample. When compared to macro-scale volumes, microfluidic volumes have higher surface area per unit volume. so, heat and mass can be more efficiently transferred [21]. This can be directly advantageous for biochemical reactions. For instance, PCR is used to amplify DNA. This reaction has been shown to have intrinsically fast kinetics and amplification time is limited by thermocycling time [13]. By creating systems that can efficiently thermocycle, PCR reaction time has been decreased. Also, high surface area give equal volumes more surface interaction. This trait has been used to enhance immunoassays with increased interactions between the analytes and surface probes [16, 22]. Also, fluid flow in these microsystems is stable and laminar at most flow conditions because it is tightly bounded by microchannel walls. As a result, flow follows predictable streamlines and only mixes via diffusion. This property of laminar flow has been used to create co-flows, micromixers and diffusion based separation systems [23–25].

In certain cases, the advantages of decreased volume, increased surface area, and laminar flow can also be problematic. First, reducing reaction volumes results in decreased signals. If the concentrations of analytes are in pM, then a 1 nL sample, on average, only contains 100 molecules. This can be below noise and detection limits [26]. Also, if target molecules are low enough in concentration, such as with cells samples, then samples will follow Poisson statistics, and detection of targets can be missed [27]. Raising surface area per unit volume can be disadvantageous in cases where surface interaction is not desired. For example, with PCR, additional polymerase must be added to perform the reaction because polymerase binds to channel surfaces removing it from the bulk sample [28]. This undesired binding can also

foul surfaces and channels which will ultimately reduce or stop microfluidic performance [29]. Finally, since laminar flow mixes only via diffusion, mixing time can be prohibitively slow. Therefore mixing must be separately addressed and micromixer technology has been developed for these cases [30].

1.3 On-Chip Chemical Handling

When dealing with small volumes of reagents, performing sequential processes is a difficult and potentially time consuming process. Volumes are microscopic, contained in microchannels and are subject to steep and sensitive pressure gradients. To perform reactions on small scales, nanoliter droplets (aqueous droplets in a continuous oil phase) are generated to make isolated chemical reactors. Many ways to alter droplets contents after generation exist. These methods include diffusive transport between droplets and the environment, merging droplets or using picoinjectors [31, 32]. These methods are potentially powerful for certain applications, but are either slow, inflexible or a passive process with no feedback and user defined control. This leaves few ways open to perform complex or sequential processes. This is further complicated when performing high-throughput chemical processes. Aside from simply adding reagents, removing reactants and separating components from nanoliter systems is still a difficult process. This has been identified in a recent review as a potential turning point for microchemical analysis technologies and some advancements have been made coupling microseparations with nanoliter chemical technologies [33]. There have been successful attempts to address this issue with electrophoresis and chrotography [34, 35]. However, the demand for these technologies still greatly outweighs the availability of available and robust methods for chemical handling.

Processing microchemical systems through separation and detection is a critical step to complete chemical analysis. It is likely that analysis will need to be performed on-chip since transporting nanoliter volumes from the microscale to the macroscale

is currently impossible. Therefore, enhancing analytical methods in the microscale is important for improving the accuracy and resolution of microfluidic analytical techniques. In addition, separations must be efficient for appropriate detection because of the small total amounts of separated species. For instance, electrophoresis involves separating charged species based on their electrophoretic mobility and requires a certain distance for this separation to occur [36]. If the distance required is long relative to the dimensions of the microfluidic system (on the order of centimeters) than microfluidic systems may lose their unique advantage of being a small, portable lab on a chip [37]. Therefore, unique properties that are exist in microfluidic systems must be accounted for when developing microfluidic separation systems.

1.4 Microfluidics for Complex Structures

Precisely manufactured channels can be used to direct and steer fluid along predefined paths. In the case of a pressure driven flow, flow travels from a high pressure to a low pressure, and will proportionally follow a path of least resistance [21]. Using this property, multiphase flows, containing particles or cells suspended in fluid have been steered into microfabricated wells. An appropriately placed microobject will block flow through the well, increasing fluidic resistance and reducing flow [38]. Subsequent flow will be steered around the well. This idea has been used to pattern large arrays of particles and cells quickly with high reproducibility. This has been used to isolate single cells and particles, pair cells and create bead-based microarrays [39, 40]. Developing methods to pattern more complex structures in terms of shape, number and composition with further proliferate this technology.

Laminar flow has been used to specifically control flows down to micro size scales. Since mixing occurs between streamlines through diffusion, flows mix slowly and fluid elements flow streamlines that can often persist for distances much greater than the length of flow. Using this property, microfluidic systems have been designed

to capitalize on the predictable flow differences between microobjects of different sizes to create cell separation systems with deterministic ratchets, distinct co-flowing streams, micro-structured fibers and to perform layer-by-layer deposition [41–43]. From a functional standpoint, optics have been integrated with continuous laminar flows to create both geometric and gradient index lenses as well as fluid core-cladding waveguides [44]. The properties of laminar flow have been used to create interesting fluid structures for material, chemical and physical purposes. By further developing of the range of control of laminar streams for further control the size, shape and pattern, laminar co-flows have the potential to increase the range and functionality of co-flowing systems.

1.5 Organization of this Dissertation

This dissertation investigates new methods of nanoliter chemical handling and detection in microfluidic systems and also explores the potential of generating structures in microfluidic systems from particles, cells and fluids. In, Chapter 2, a method for actively controlling nanoliter droplets' chemical composition is introduced. This simple method is used to continuously control nanoliter chemical systems by integrating a time-resolved convective flow signal across a permeable membrane wall. With this method the volume and concentration of nanoliter-sized drops can be controlled without direct convective contact between droplets and the continuous flow. Mass transfer properties are quantified and fluid introduction and removal rates are achieved ranging from .23 to 4.0 pL/s. Furthermore, this method is expanded to perform chemical processes. Silver chloride was precipitated using a flow signal of sodium chloride and silver nitrate droplets. From there, sodium chloride reactants were separated with a water flow signal and silver chloride solids were dissolved with an ammonia hydroxide flow signal. Finally, this system was used to deliver large molecules and perform physical processes like crystallization and particle packing.

Non-uniform distrubtion of dsDNA oligomers during polyacrylamide gel electrophoresis (PAGE) in a microfabricated system is explored in Chapter 3. Confocal Laser Scanning Microscopy (CLSM) was used to image fluorescently labeled DNA during electrophoretic migration. The distribution of dsDNA larger than 100 bp is observed to transition from a center-biased motion on the transverse plane 1 cm downstream from injection to an edge-biased motion 2 cm downstream. While this distribution increased with increasing dsDNA size in a cross-linked gel, no similar distribution was found with the same dsDNA molecules in a linear polyacrylamide solution (6% LPA). Simulations of DNA distribution in gels suggest that DNA distribution nonuniformities may be caused by biased electrophoretic migration resulting from motion in an inhomogeneous gel system.

In Chapter 4, a two-dimensional micro-object positioning methods is introduced. This method is a non-planer microfluidic device which uses laminar convective flow to actively position particles into any desired, two-dimensional, predesigned pattern. Objects including 10 μm polystyrene particles and *Saccharomycesludwigii* cells are rapidly (2 s) loaded onto vacuum-actuated holes, allowing us to both generate anisotropic particles and culture *S.ludwigii* cells. The device was further modified to individually control two sets of holes, adding control of pattern composition. With rapid, precise and adaptable operation, multilayer microfluidic devices should greatly assist in research where precise object placement and proximity is necessary.

Finally, in Chapter 5, a three-dimensional microfluidic device architecture has been designed to scale and actively miniaturize co-flowing streams to desired dimensions. This architecture allowed for devices to scale both the size and number of co-flows with few independent design parameters. This was used to generate submicron streams by constricting 64 streams in a single microchannel. Finally, the quality of produced co-flows was investigated with respect to uniformity, diffusion and Dean flow.

CHAPTER II

Control of Mass Transport to Nanoliter Droplets using Separated Convective Signal Flows

2.1 Introduction

Nanoliter droplet emulsions formed in microfluidic channel networks are used to create discrete chemical and biological systems with uniform and controlled contents [1]. Droplets are an ideal platform with which to perform high-throughput analysis because they require minimal reagents and allows for thousands of nanoliter droplets to be produced per second, which can respectively reduce cost and time to perform analytical experiments [45]. Once confined to microfluidic channels, droplets can be isolated and monitored as individual chemical or biological systems. Droplets have been used for directed evolution in microbial systems by culturing single cells to remove bulk averaging from cell populations, for optimization of chemical reactions by controlling reagent concentrations and reaction times, and for amplification of DNA with PCR using fast thermocycling times [28, 46–49]. In a recent review of microdroplets, Theberge, et. al. asserted that further proliferation of droplet technology will be facilitated by integrating droplet processes, such as separations and reactions, and is currently limited by researchers ability to control droplets environments and contents [33]. The idea of unifying droplet operations is an appealing concept and

has been investigated by combining chemical reactions in droplets and continuous flow separations on a chip [35]. However, the technology to control the contents of droplets and interface this technology with other chemical systems does not yet exist in a mature form [50].

Simple methods to control droplet contents are important to the development of droplet technology from a user and application oriented viewpoint. Convection and diffusion-based mass transfer have been used to control droplets after generation. Convection uses hydrodynamic flow to control droplets by splitting, pairing and merging them [32]. For example, merging droplets can create controlled reactions and has been used to produce CdS nanoparticles, poly(lactide-co-glycoide) and magnetic iron oxide nanoparticles [51–53]. However, hydrodynamic systems operating with discrete fluid volumes, are sensitive to flow conditions and require optimization of operational parameters to behave properly. Vapor diffusion between microdroplets can be used to continuously manipulate droplets, and in two cases, conditions for molecular and protein crystallization were rapidly screened [54, 55]. Controlled mass transfer mitigates fluidic design constraints, compared to systems operating with hydrodynamic droplet manipulation. However, mass transfer methods operate from initial conditions and cannot quickly or continuously manipulate droplet conditions and compositions. By combining active control of droplet conditions using convective transport with the ease of use of mass transfer to droplets, the range of control for droplet systems can be expanded to allow for the integration for chemical reactions, separations and dilutions in a single system. Use of a permeable membrane, first developed in 2007, is explored to transport both water and ethanol to crystallize proteins and salts [55, 56]. This method used a multilayer fluidic device and would create large volume changes in droplets in a matter of several hours.

2.2 Materials and Methods

2.2.1 Device fabrication

Poly(dimethylsiloxane) (PDMS) microfluidic devices were casted from either a 10, 35 or 75 μm SU-8 mold (measured from a surface profilometer) and bonded to glass slides after oxygen plasma treatment [57]. Channels were treated with siloxane solution (Rain-X Original, Unelco) overnight to ensure all surfaces in the device were hydrophobic.

2.2.2 Droplet generation

Two VSO-EP electronic pressure controllers (Baker) were used to control the inlet pressures of oil and water from an external pressure source. Pressure was applied to generate droplets in a previously developed oil-water T-junction design [58]. The continuous phase was made from solutions of fluorinated oil (FMS-121, Fluka) premixed with surfactant (1H,1H,2H,2H-Perfluorooctanol, Alfa Aesar) at 5% v/v surfactant to oil. Droplet solutions were made from either deionized water or from premixed deionized water-ethanol solutions.

2.2.3 Droplet size experiments

Flow was stopped and stationary droplets were measured for all measurements to ensure consistency. For the stability measurements, YPD (Yeast Peptone Dextrose) solution was used as a droplet phase. The fluidic signals were applied to our channels through either a syringe with the desired liquid, or a hose connected to a nitrogen tank controlled again by a VSO-EP electronic pressure controller. During liquid extraction experiments, dry nitrogen was applied to the side channels at $P = 50 - 60$ kPa. When growing droplets, the side channel was flushed every two minutes to ensure the channel was filled and pure. Droplets were monitored using a stereoscope and droplets were

analyzed using ImageJ software. The area of the droplets was approximated with an ellipse for a spherical droplet and with the geometry tool if the droplet was deformed.

2.2.4 Water in Oil Concentration

To determine the concentration of water in FMS-121 fluorinated oil a 25 mL picnometer was used. Constant density was assumed between the water and oil phases. Oil density was measured in two situations, after being dessicated and baked, and after being submerged in water. All measurements were performed in a clean room at a uniform environmental temperature and humidity.

2.2.5 COMSOL Simulations

Droplet evaporation simulations were performed in COMSOL Multiphysics v3.4. The two-dimensional, steady-state diffusion simulations were used. Thermodynamic discontinuities were used based on solubility concentrations. At the droplet/oil interface water is assumed to be at saturation and air is assumed to be water free. The saturation concentrations of water in oil, PDMS and air used were 1,300, 40 and 1.3 mol/m^3. Air diffusion used was 1e-5 m^2/s and oil/PDMS diffusion used was 1e-9 m^2/s.

2.2.6 Colloidal Crystallization

For colloidal packing experiments, Polybead polystyrene red dyed microspheres (3 μm diameter) were diluted with deionized water to 0.2 wt% and sonicated for 15 minutes to disperse possible particle aggregates. The particle solution was then used to create droplets. Once liquid was extracted, the particle clusters were imaged in situ under a Zeiss Axioskop with a 40x microscope objective and enhanced in Adobe Photoshop CS3.

2.2.7 Chemical Functions

For reactions/separation/extraction experiments, 3M aqueous NaCl solution was used for all the experiments and 1M $AgNO_3$ solution was mixed with water and produced in droplets. For liquid extraction, 20% ammonia hydroxide solution was used for the side channels.

2.2.8 Small Molecule Delivery

Side stream solutions of rhodamine B (Fluka)-water and rhodamine B-ethanol solutions were flowed into the side streams for a desired time period. Droplet images were captured on a Zeiss Axioskop with a 10x objective and a dichroic filter to resolve the fluorescence signal.

2.3 Results and Discussion

2.3.1 Device Design

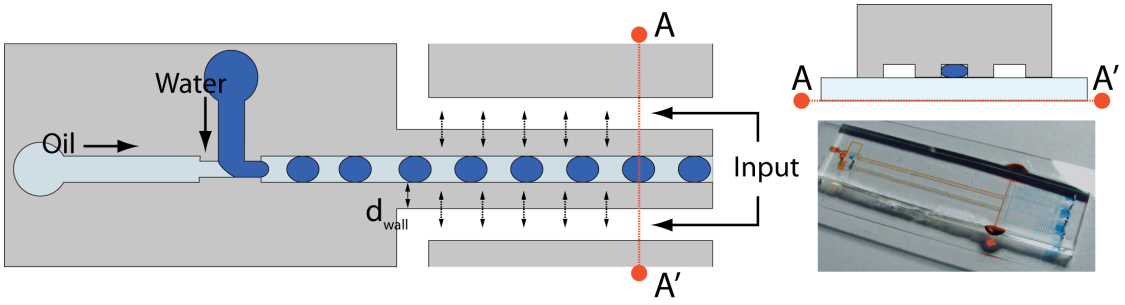

Figure 2.1: Method schematics and device design. Droplets are generated in a T-junction and then move to a channel with side-streams separated by a permeable wall.

We have developed a simple method, to manipulate droplets with mass transfer through user-controlled convection. We intend this work to be a straightforward microfabrication process and demonstrate the functional possibilities that can be gained by coupling fast response times with a thorough mass transfer analysis. Mass transfer

occurs as a result of an imposed concentration gradient between droplets and independent side channels that are separated by a narrow, permeable poly(dimethylsiloxane) (PDMS) wall (Figure 2.1). In the past, the permeation of fluid through PDMS walls has been used to create convective flow [59]. Our method allows an applied convective flow to indirectly contact droplets through PDMS while avoiding additional fluidic constraints and microfabrication steps. Because the side channels are independent from the droplets, different chemical species (both liquid and gas) can used. This system was used to manipulate droplet sizes and contents and to create significant steady and transient mass transfer responses. Mass transfer responses were thoroughly investigated and the ranged of operations of this device used to extract water from a droplet, dilute a droplet with ethanol, pack colloids, crystallize salt, perform a chemical reaction, dilution and dissociation and deliver a fluorescent dye.

2.3.2 Basic Droplet Functions

Droplet contents are controlled by mass transport between the droplet and a side channel separated by a PDMS barrier. In this case, mass transport occurs by diffusion, and manifests itself as a chemical species preferentially travelling along a concentration gradient. This process is possible because of the permeability of the continuous fluorinated oil phase and membrane (PDMS) to a given chemical species such as water or ethanol.

The convective stream and droplet interaction creates conditions for two basic manipulation operations: extracting contents from droplets and adding chemical species to droplets. These two processes are fundamentally similar and follow Ficks first law of diffusion, with diffusion occurring from a concentration gradient. However, the concentration gradient is reversed between cases. For removing liquid from droplets, droplets made of either water or half-water and half-ethanol were generated in a droplet channel. The convective side channel was exposed to dry nitrogen flowing at

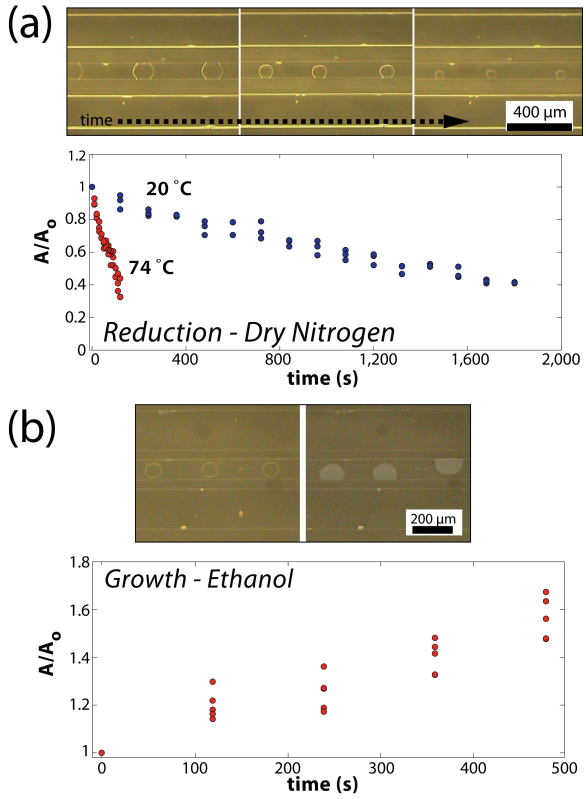

Figure 2.2: Basic droplet operations. a) Droplet evaporation. A is area, A_o is initial area and t is time. b) Droplet growth and dilution. Droplets are highlighted in the second image.

an input pressure of $P = 50 - 60$ kPa. To measure droplets, flow was halted and droplets are set in place. Droplets shrink with time because water is diffusing along the water concentration gradient through the fluorinated oil and PDMS and into the N_2 stream (Figure 2.2a). Nitrogen diffusing into the droplets from the side channel cannot cause any comparable growth of the droplets. Since the gas stream is dry and flowing, there is a constant, low concentration of water and ethanol in the gas phase and the accumulation of liquid on the sidewalls is negligible. The concentration of water at the PDMS/oil boundary is non-zero and limited by saturation concentration in PDMS. This is important to note because ethanol and water have different saturation concentrations, diffusion coefficients, and therefore different rates of mass transfer [60]. Evaporation can also be fine-tuned by temperature, which appears to

exponentially increase the rate of evaporation.

For liquid addition, water-ethanol droplets were generated in the center channel and the side channels were subsequently filled with ethanol. Droplets will grow because ethanol can diffuse into the droplet more quickly than water will diffuse out of the droplet, owing to a higher saturation concentration of ethanol in PDMS (Figure 2.2b). Droplet growth is also likely affected by the water-ethanol mixtures azeotrope of 96% ethanol. Two interesting consequences arise from diluting droplets with ethanol: First, the droplet is more difficult to resolve because ethanolx's refractive index difference causes a poorly defined droplet interface (droplets are highlighted with a white overlay). Second, because the interfacial tension of the mixture is different from the initial droplet, droplets are more attracted to the PDMS. This can be observed as droplets adhering to PDMS walls exhibit a decreasing contact angle. This result may be desirable because solvents like ethanol, cannot be normally created in nanoliter droplets because of their attraction to PDMS.

2.3.3 Combined Operations

The two operations, droplet size reduction and droplet growth, can be combined to create a time-resolved signal to stabilize droplets and oscillate their contents. The side channel input versus droplet response can be thought of as a fluid signal input and droplet output (Figure 2.3a). Droplets of cell growth medium (YPD) were stabilized at $t = 0$ and after the droplets have shrunk to a target size (Figure 2.3b). This could be desirable for long-term cultures in microdroplets, to selectively create small and concentrated droplet reactors. A complicated time-resolved droplet response was demonstrated with a square wave signal which produced oscillations in a droplets projected area by almost 40% of its original size with no appreciable lag (Figure 2.3c). The lag between signal input and droplet response is short because mass transport occurs in a microfluidic system with microscale features. For instance, the

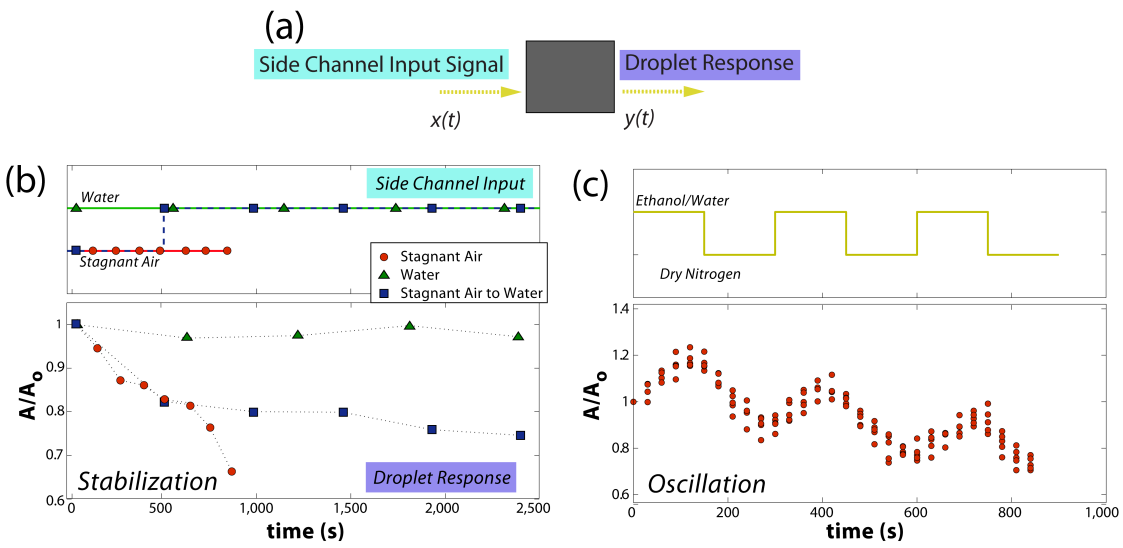

Figure 2.3: Droplet signal input and output. a) Signal-response black box system concept. b) Droplet size stabilization. A is area, A_o is initial area and t is time. Droplet size stabilization at $t = 0, t = 500$ s, and no stabilization. c) Oscillation of a droplet undergoing size reduction and growth with a time resolved signal in the second image.

diffusion time for a molecule with a diffusion coefficient of $D = 10^{-9}$ m^2/s diffusing across a 100 μm membrane is on the order of 10 s [61]. The negative overall slope for the oscillation curve is a result of the rate of growth being slower than the rate of reduction. Although droplet change is only measured by droplet size, composition is changing, favoring more ethanol in the droplet, which can create a dynamic condition that is only sustainable for a certain time. Complicated signals could conceivably be used to create dynamic droplets conditions for screening a huge range of variables by changing a convective signal. Also, this demonstrates the ability of the system to sequentially change droplet conditions and could be transferred to a system with stepwise reactions of multiple phases.

2.3.4 Mass Transport Analysis

The range of volumes that can be delivered or removed are limited by mass transfer rates versus residence times. Droplets often flow with the continuous phase and can

have residence times under 10 seconds in a microchannel. In many cases, such as for chemical reactions, delivering a relatively small number of molecules is acceptable. For example, adding 1% of a 1 M HCl solution to a pH 7 water droplet would change the droplets environment considerably. However, cases where delivering volumes closer to the overall droplet volume can be more difficult. Therefore, investigating parameters controlling mass transfer is important to investigate, and this was done using the model case of a water droplet evaporating.

2.3.4.1 Assumptions

Resistance to diffusion is negligible in the oil and primarily occurs in the PDMS. To understand the resistance of oil and PDMS on mass transfer, the permeability, defined as the product of a diffusion coefficient (D) and a maximum solubility (C_{sat}), can be compared. It can be assumed that the diffusion coefficients of water in fluorinated oil and PDMS are close. From picnometric analysis, the solubility of water in oil was measured to be 1,300 mol/m^3, around 30 times higher saturation than PDMS, suggesting that resistance to mass transfer through the oil is negligible. All transport assumptions that are used will simplify the full mass balance Equation 2.1 to derive basic equations are as follows and also can be visually seen in Figure 2.4 with all relevant variables labelled [61].

$$\frac{\delta C}{\delta t} + \vec{v} \cdot \nabla C = D\nabla^2 C + R \tag{2.1}$$

(a) Distance between the droplet and air channels, $O(10^{-4})$ m is much smaller than the distance between the droplet channel PDMS device boundary $O(10^{-2})$ m, so little mass transfer is out of the device and most mass transfer is into the air channel. (b) Assume the oil provides no resistance as compared to the PDMS. (c) Assume psuedo-steady state since the PDMS boundaries and concentration boundary conditions are fixed ($\delta C/\delta t = 0$). (d) No convection ($\vec{v} = 0$) (e) No reaction ($R = 0$)

(f) Since the oil provides little resistance to mass transfer, the end of the droplets can be assumes as a constant value with surface area equal to the height of the droplet, h, multiplied by the width of the droplet, w_{drop}. $\nabla = \delta/\delta x + \delta/\delta z$. (g) The concentration out the top is a function of the distance between droplet and air channels and will related to mass transfer out the sides for fixed droplet/air separations. This mass transfer can be represented by multiplying by an effective area. Therefore the system is simplified to one dimension, Equation 2.2. $\nabla = \delta/\delta x$.

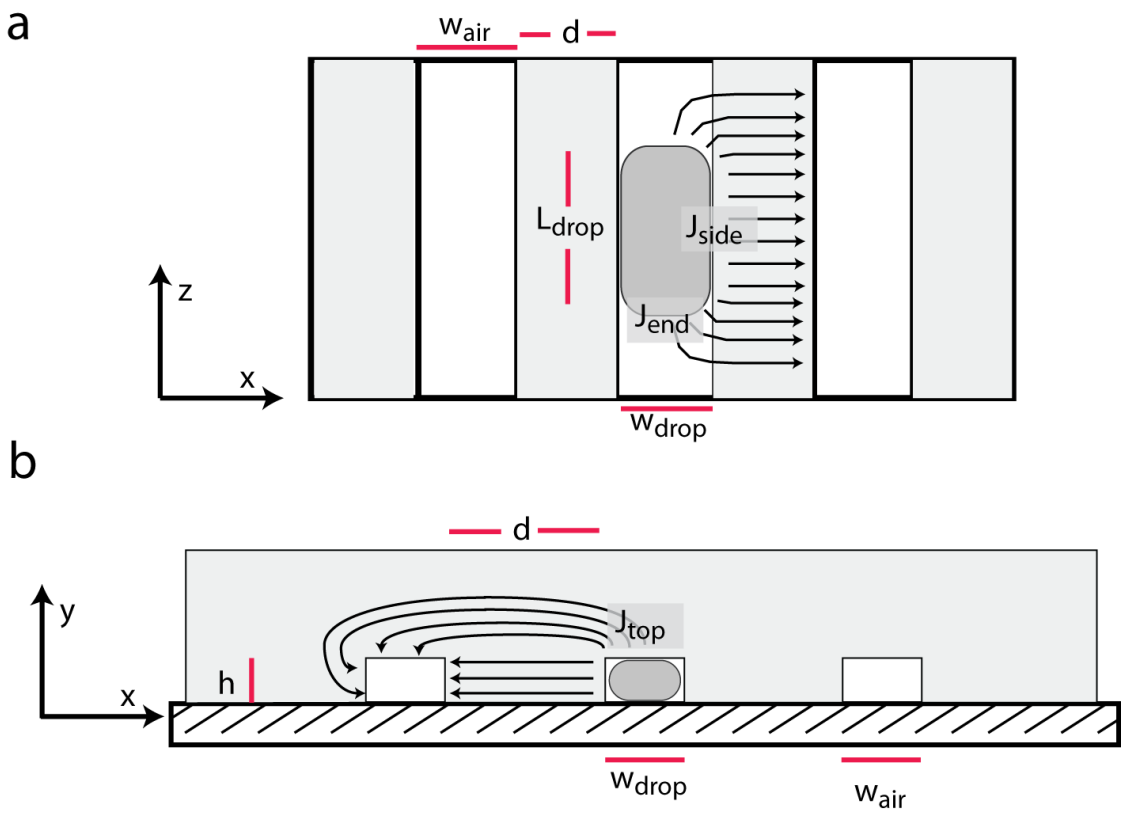

Figure 2.4: Diagram of transport with a droplet located in the channel. (a) Top view of droplet transport (b) Side view of droplet transport.

$$\frac{\delta^2 C}{\delta x^2} = 0 \tag{2.2}$$

Since all resistance occurs in the PDMS, a Ficks diffusion model is assumed for molecular diffusion flux, J. This is found by solving Equation 2.2 with boundary

conditions, Equation 2.3 and Equation 2.4.

$$C(x = 0) = C_{sat,PDMS} \tag{2.3}$$

$$C(x = d) = \frac{C_{sat,PDMS}}{C_{sat,air}} C_{air} = HC_{air} \tag{2.4}$$

Here, d is the separation between droplet and air channels, C_{air} is the concentration of water in the air channel, H is the ratio of saturation concentrations of water in PDMS versus air ($H = C_{sat,PDMS}/C_{sat,air}$), A_E is an effective surface area and multiplied by the flux is a total mass transfer rate,N, giving Equation 2.5:

$$N = A_E J = \frac{2A_E D}{d}(C_{sat,PDMS} - HC_{air}) \tag{2.5}$$

This is multiplied by 2 to represent two channels where diffusion can take place. The A_E, Equation 2.6 takes into account both transport out the side, ends and top of the droplet:

$$A_E = L_{drop}h + w_{drop}h + L_{drop}f(d) \tag{2.6}$$

Where the first term is the area of transport from the sides of the drop, the second term is the area where transport occurs from the end of the drop and the more complicated third term represents transport through the top of the channels. Transport out the top of the droplet is represented by $f(d)$. From assumption (f), it is assumed that transport out the ends of the droplet is resisted very little by the oil, so the entire end area can be considered uniform diffusing area. This A_E term also assumes that transport out the top of the device is independent to transport through the side-walls of the device. By altering different variables, the terms of Equation 2.5 can be further assessed. Volumetric transport rate can be assessed from the mole

transport rate by:

$$\dot{V} = \frac{N}{\rho MW} \tag{2.7}$$

where ρ, is density, MW, is molecular weight.

2.3.4.2 Projected Volume Measurements

The rate of diffusion can be measured by the change of a projected droplet area with respect to time. Although, a droplets change in area versus time appears linear and constant while observing changes over small transport ranges, seen by Figure 2.2 and 2.3, over a large volume change, we observe a deviation from a linear approximation (Figure 2.5a). The volumetric mass transport rate is calculated by assuming a constant mass flux (using the pseudo steady state assumption) from the top, sides and ends of the droplets along with a changing area. This derivation and model is derived assuming an approximate rectangular block shaped droplet with constant fluxes ($J_{top}, J_{end}, J_{side}$) out of each the top, the ends and the side of the drop ($A_{top}, A_{end}, A_{side}$) in Equation 2.8

$$\dot{V} = A_{top}J_{top} + A_{end}, J_{end}, +A_{side}J_{side} \tag{2.8}$$

The values of these areas are listed in Equation 2.9, Equation 2.10 and Equation 2.11. It can be seen that two of these values are linearly dependent on the projected droplet area, A.

$$A_{top} = A \tag{2.9}$$

$$A_{end} = wh \tag{2.10}$$

$$A_{side} = \frac{Ah}{w} \tag{2.11}$$

Droplet volumes can be approximated as cylindrical, for diameters greater than channel height, so the volumetric transport per second, $\dot{V}$, is the change of projected area with respect to time, $\delta A/\delta t$, multiplied by the channel height, h. Since $\dot{V} = h\delta A/\delta t$, this equation can be simplified by combining Equation 2.8 with Equation 2.9, Equation 2.10, Equation 2.11, collecting constants to, c_1 and c_2, and the result is listed in Equation 2.12:

$$\dot{V} = h\frac{\delta A}{\delta t} = c_1 A + c_2 \tag{2.12}$$

Solving this linear ODE with boundary condition Equation 2.13 results in the area versus time equation of Equation 2.17.

$$A(t = 0) = A_o \tag{2.13}$$

$$A = (A_o + \frac{c_2}{c_1}e^{c_1 t} - \frac{c_2}{c_1}) \tag{2.14}$$

Droplet sizes with projected areas of 10,000 μm^2 are used as the standard to calculate transport rates for future measurements. It is measured from the fit in Figure 2.5a that the evaporation rate linearally decreases (Figure 2.5b) as would be expected from the model.

2.3.4.3 Temperature, Channel Height and Wall Width

As a calibration, the change in droplet diffusion and evaporation was measured in a microchannel versus temperature. Since pure water droplets are affected, an Arrhenius relation (Equation 2.15) between evaporation rate and temperature was

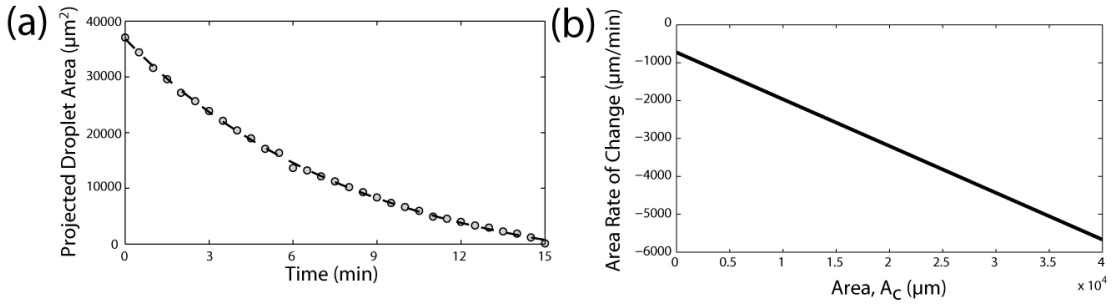

Figure 2.5: Evaporation rate of water versus projected area. (a) Droplet area versus time for large droplet sizes along with a fit based on Equation 2.6. (b) Rate of change of droplet area versus droplet area.

expected:

$$\dot{V} \propto e^{-\frac{\Delta H_{vap}}{k_b T}} \tag{2.15}$$

with the heat of vaporization (ΔH_{vap}) being that of water (40.65 kJ/mol). With linear regression and weighted least squares analysis, an activation energy of $40.5 \pm .9$ kJ/mol was measured, well within the theoretical value (Figure 2.6a).

By changing the height of the device and combining Equation 2.5 and Equation 2.6, the total rate is can be simplified into a linear equation Equation 2.16 and can be used to determine the properties of the PDMS system:

$$N = \frac{2C_{sat,PDMS}D}{d}(L_{drop} + w_{drop})h + \frac{2L_{drop}C_{sat,PDMS}D}{d}f(d) \tag{2.16}$$

In this case, side channel airflow is assumed to be sufficiently high that $C_{air} \simeq 0$ and other parameters used were d, w_{drop}, $L_{drop} = 100\mu$m and $T = 42°C$. From the slope of a best fit of data taken with varied height (Figure 2.6b), $C_{sat}D$ was found to be $1.7 \pm .1 \times 10^{-7}$ mol/m-s. In literature, $C_{sat}D$ is around $4 \times 10^{-7} - 4 \times 10^{-8}$ assuming water-PDMS diffusion of 10^{-9}-10^{-8} m^2/s [59, 62]. The value found may also be on the high-end of this range because temperature used is $17°C$ higher than room temperature. In this case, the term, $f(d)$, was determined to be $28.0 \pm .6$ μm.

COMSOL simulation datas trend is in close agreement, displaying a linear correlation with changing height ($R^2 = .9999$).

By changing the distance between channels droplet evaporation rates the dependence of mass transfer rate on channel separation can be predicted (Figure 2.6c). Rates scale inversely with the distance between droplet and air channels. Plotted in Figure 2.6c, is the measured rate, versus the predicted rate out of the side and end of the droplets (assuming $f(d)$ to be 0). It is observed that at low separations, transport out the channel sides and ends is more influential than transport out the channel top. At higher separations, transport out the top of the channel becomes increasingly greater. Also, at close separations, resistance from the oil may begin to influence transport which would decrease overall evaporation rates and be the reason why there is a crossover of the predicted side-wall transport versus total measured transport under 50 μm.

2.3.4.4 Nitrogen Flow Rate

Finally, the ratio of water concentration at the air channel/PDMS interface was changed and compared by changing the convective channel dry nitrogen flowrate with varying pressures. Water concentration in the air channel changes the magnitude of the water concentration gradient that drives water transport from the droplet channel to the air channel. Higher inlet pressures result in higher flowrates, less mass transfer time per volume of air, and therefore drier air with a steeper concentration gradient. Also, as the air flows further in the channel, and therefore is in contact with diffusing water longer, it will have a higher water concentration. The concentration of water in the air channel should be uniform because diffusion time ($t \sim w_{air}^2/4D_{air}$) is much less than the time for mass transfer of the water into the flowing air. Water in the air channel's concentration versus residence time in the air channel can be directly calculated by Equation 2.17.

$$2V_{air}\frac{\delta C_{air}}{\delta t} = N \tag{2.17}$$

Position of air in the channel, y, is related to residence time, t, by Equation 2.18.

$$y = Ut \tag{2.18}$$

Where, U, is air flow average velocity. Equation 2.17 can be changed to being dependent on position in the channel by Equation 2.19.

$$\frac{\delta C_{air}}{\delta t} = \frac{\delta C_{air}}{\delta y}\frac{\delta y}{\delta t} = U\frac{\delta C_{air}}{\delta t} \tag{2.19}$$

By combining Equation 2.17 with Equation 2.5, a separable ODE can be set up (Equation 2.20) which describes air channel water concentration versus known parameters. The boundary conditioned used is that air enters completely dry when introduced (Equation 2.21).

$$2V_{air}U\frac{\delta C_{air}}{\delta t} = \frac{2A_E D}{d}(C_{sat,PDMS} - HC_{air}) \tag{2.20}$$

$$C_{air}(y = 0) = 0 \tag{2.21}$$

The ratio A_E/V_{air} arises which is solved in Equation 2.22.

$$\frac{A_E}{V_{air}} = \frac{\frac{w_{drop}h}{L_{drop}} + h + f(d)}{hw_{air}} \tag{2.22}$$

With Equation 2.22, combined with Equation 2.20 the driving force can be solved for in Equation 2.23.

$$(C_{sat,PDMS} - HC_{air}) = C_{sat,PDMS}exp^{-\frac{\frac{w_{drop}}{L_{drop}}h+h+f(d)}{hw_{air}}\frac{HDy}{d}\frac{1}{U}} \tag{2.23}$$

And, this can be combined with expression Equation 2.5 to describes mass transfer from the droplet into the air channel (Equation 2.24).

$$N = \frac{2A_E DC_{sat,PDMS}}{d} exp^{-\frac{\frac{w_{drop}}{L_{drop}}h+h+f(d)}{hw_{air}}\frac{HDy}{d}\frac{1}{U}} \tag{2.24}$$

By changing the inlet pressure of the nitrogen stream, and estimating a velocity based on laminar ($Re < 10^3$) Pousille flow in Equation 2.25, the average velocity can be calculated from pressure.

$$U = \frac{1}{12}\frac{h^2}{\mu L_{channel}}\Delta P \tag{2.25}$$

The predicted trend is that total diffusion rate, with a fixed viewing position and geometric variables varies by $exp^{-1/U}$. This trend and the specific values match experimental data as seen in Figure 2.6d.

2.3.5 Particle Packing

Size reduction of droplets can be used for a variety of functions, such as crystallization and packing colloidal clusters [55, 63, 64]. To create particle packings, a particle solution (3 μm diameter) was loaded into droplets of uniform size and composition, and water was subsequently removed (Figure 2.7). Extracting water created a volume change forcing particle packing by increasing the density of the solution and capillary forces create a packed structure. As the droplets evaporate, they become more opaque as a direct result of the particle density in the droplets. This could also be done to crystallize large sodium chloride crystals at slow evaporation rates (Figure 2.7d).

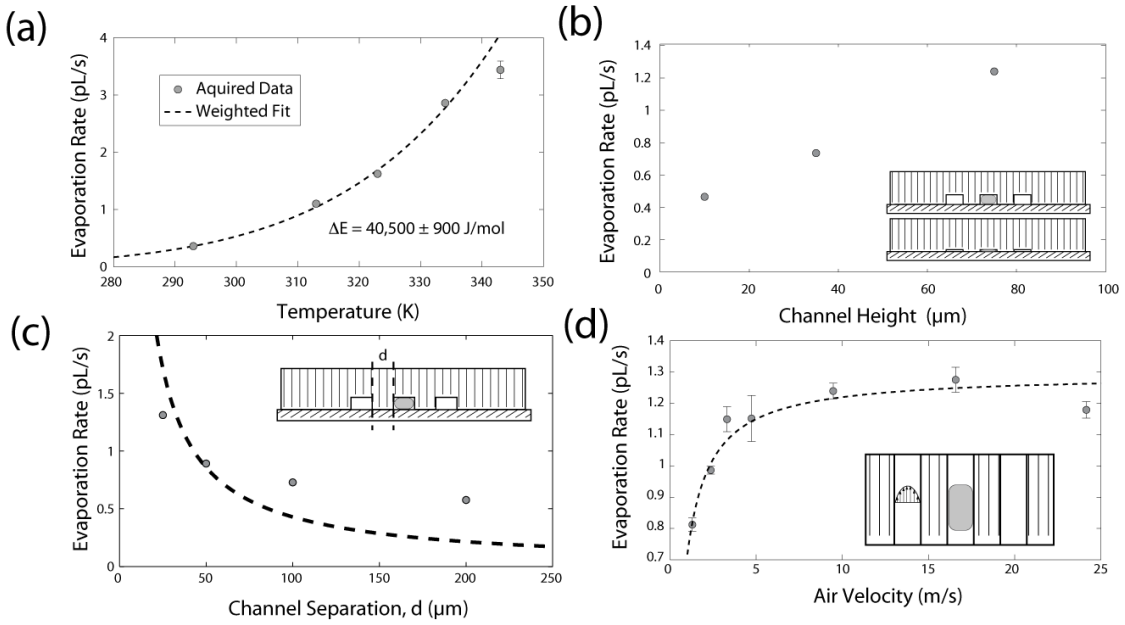

Figure 2.6: Evaporation rate of water measured at several different conditions. (a) Droplet evaporation rate versus temperature at a height of 75 μm, wall width, d, of 100 μm and 50 kPa air flow. (b) Droplet evaporation rate versus channel height with a wall width, d, of 100 μm and 50 kPa air flow (c) Droplet evaporation rate versus wall width with a channel height, h, of 35 μm and 50 kPa air flow (d) Droplet evaporation rate versus air flow with a channel height, h, of 75 μm and wall width, d, of 100 μm.

2.3.6 Chemical Processes

The primary functions of time resolved size reduction and growth were used to sequentially perform chemical processes on nanoliter droplets (Figure 2.8). First, aqueous sodium chloride (3 M, salt) flows through the side channels and 1 M aqueous silver nitrate droplets were generated. It is believed that salt diffuses into the droplets and the chlorine reacts with the silver, generating insoluble silver chloride precipitate (Figure 2.8a). Droplets without sodium chloride side channels have no precipitate. Diffusion is believed to be the mechanism of salt transport based on the fact that diffusion has been shown to occur for solvents and liquids and should be occurring on a slower timescale. We note that if droplets are made, and remain stationary before sodium chloride is introduced into the side channels, then no silver chloride crystals

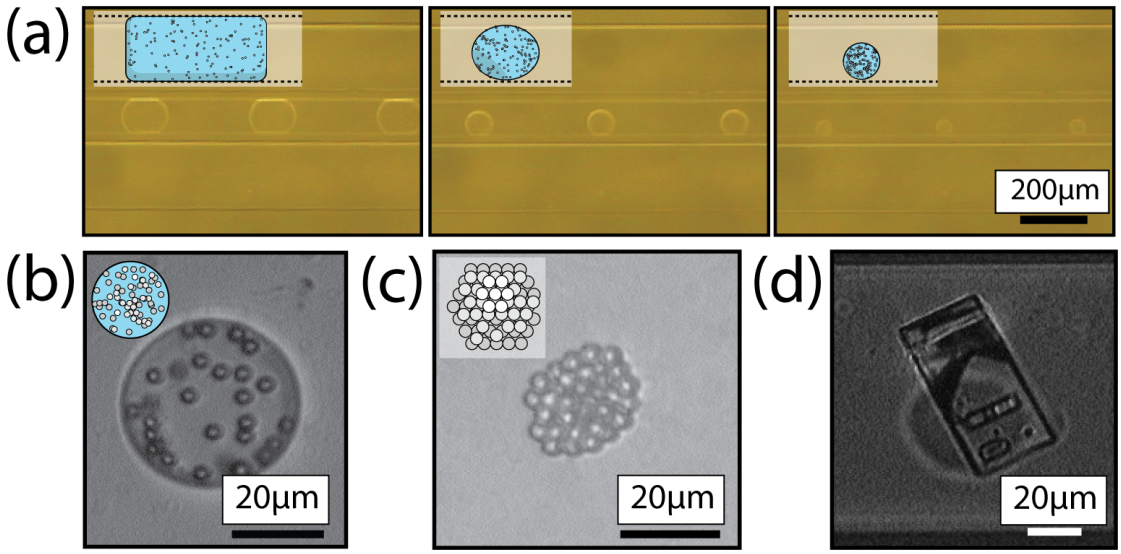

Figure 2.7: (a) Droplet shrinking initially concentrated with 0.2 wt% particles. (b) Droplet magnified prior to full evaporation. (c) Packed particles. (d) NaCl crystal.

form. We attribute this to the silver nitrate quickly leaving the droplets before the reaction occurs.

By flowing dry nitrogen, the droplet can be shrunk and the salt and silver chloride concentration will increase. This causes sodium chloride to precipitate in the droplet (Figure 2.8b). Alternatively, instead of precipitating the salt reactant, excess reactant was separated from the system to leave only product in the droplet. Water was used as the convective stream and salt is diffuses out of the droplet. Since silver chloride is solid, it does not leave the droplets. After this step and shrinking the droplet, no sodium chloride crystals form. Finally, the solid silver chloride precipitate can be extracted back into solution by setting the side channel with ammonia hydroxide, which silver chloride is soluble in (Figure 2.8c).

These reactions are dependent on ion transport and therefore the PDMS membrane and fluorinated oil must been permeable to ions, notably sodium chloride. PDMS has been previously used to transport salts and reported to have transported salts (including sodium chloride) for drug delivery applications [65, 66]. To confirm

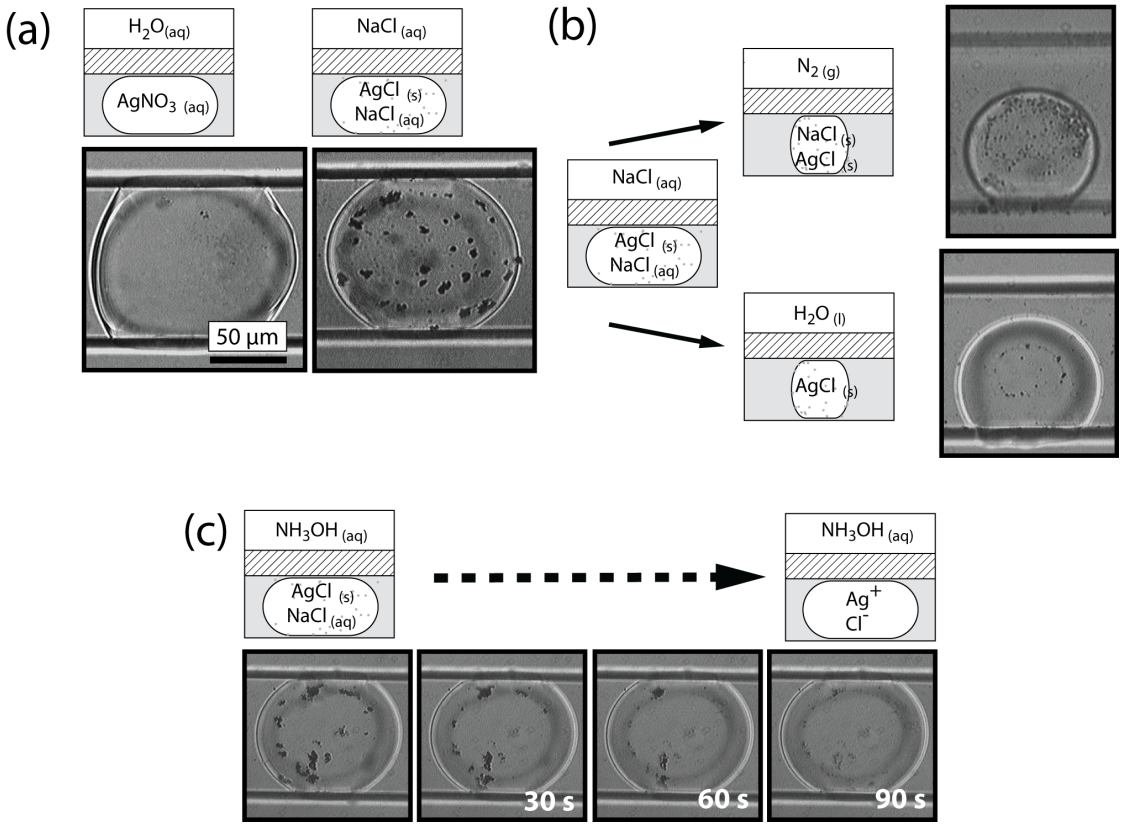

Figure 2.8: Chemical functions using signal flows. a) Aqueous silver nitrate droplets surrounded by water and with diffusing sodium chloride to precipitate silver chloride crystals. b) Salt precipitates with air in the side channels but does not with water side-channels. c) Silver chloride is soluble in ammonia hydroxide and the crystals are extracted into the droplet.

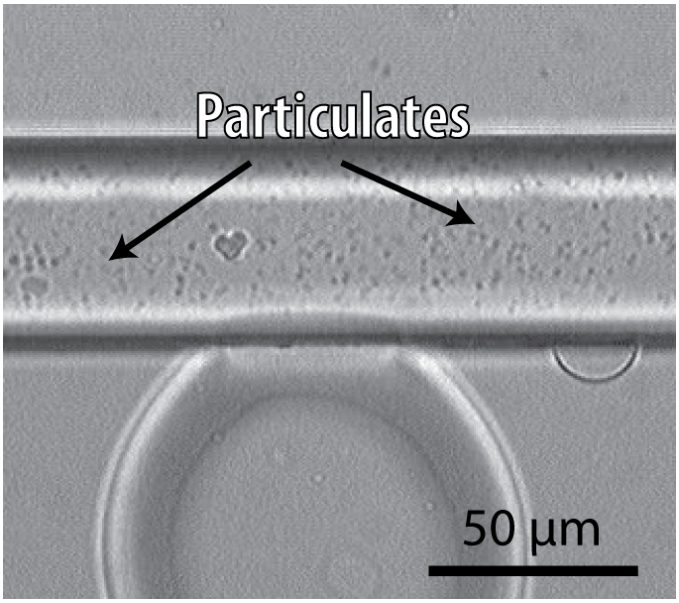

Figure 2.9: Silver chloride precipitate formed in the PDMS wall from silver nitrate droplets and a sodium chloride convective flow. Scalebar is 50 μm.

that sodium chloride is diffusing through the PDMS, the sodium chloride to silver chloride reaction was performed in the PDMS wall. Silver nitrate droplets were formed and set in the channel for under 1 minute. This should have loaded the PDMS wall with silver nitrate, at which point sodium chloride solution is loaded in the convective side channel. As expected, and seen in Figure 2.9, precipitate forms inside the PDMS wall. Ammonia hydroxide solution was later flowed in the convective side channel, and this precipitate dissolved.

This result was also confirmed to not be a convective process because pressure applied to the microchannels never compromised the separation between droplet and convective channels. Also, the uniformity of the density of particulates would undermine that salt ions travel because of a leak. This result makes it clear that transport in these systems when reactions are concerned are sensitive, flexible to the ends and must be performed carefully to have a desired reaction in the droplet instead of in the PDMS. Transport is likely a classical diffusion system, where ions suspended in water will diffuse into the PDMS to equilibrate their concentration and lower the systems

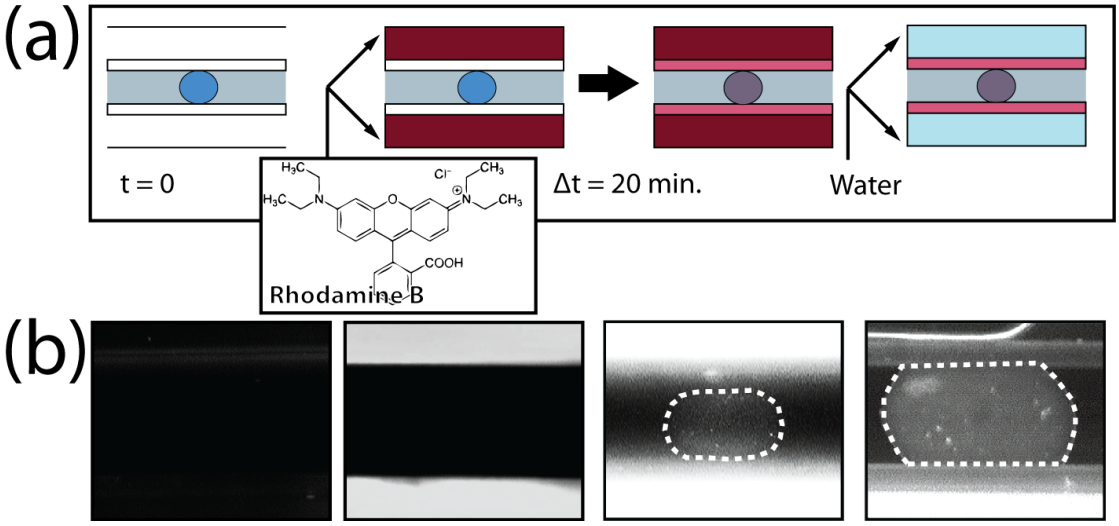

Figure 2.10: (a) Transport of rhodamine B into droplets. Flowchart of experimental procedure used to transport rhodamine B into droplets. (b) Images corresponding to the flow chart. Droplet edges are highlighted.

overall energy.

2.3.7 Transport of Small Molecules

PDMS is permeable to larger molecules, so dyes and drugs can be delivered to droplets from a convective source [67]. The fluorescent dye rhodamine B (MW = 479.01) diffused into the droplets, and was confirmed with fluorescent images of droplets with no rhodamine B, and droplets after rhodamine B was loaded into side channels (Figure 2.10). Also, as demonstrated by the fluorescent images of the system, molecules will remain in PDMS after the side stream signal has been removed. So, reactions involving different interacting reactants may be inhibited by this effect.

2.4 Conclusions

Devices combining convective fluid signals interacting with droplets have enormous potential to direct nanoliter droplet systems because of their ease of fabrication and operation, and versatility to operate with a wide range of molecules and per-

form sequential processes. From a materials standpoint, replicating this setup with different materials, like polyesters or perfluoropolyethers, and different continuous oil phases can be used to change the solubility and diffusion characteristics of molecules inside of this system [68, 69]. This can be studied to create systems that provide selective mass transport into and out of nanoliter droplets, such as with sodium chloride or other salts [55]. Variables affecting the rate of transport out of droplets have been analyzed. To achieve higher transport rates, increased temperature, minimized channel height and membrane thickness can greatly increase rate in cases where large transport volumes are required. Multiple convective channels can be added to create sequential transient steps for flowing droplets, avoiding species interacting in the membrane. This concept can be used to assist in current microfluidic devices to provide a real-time environment to perform a myriad of functions such as sequential reactions, time-dependent system probing, dilution, extraction and crystallization. Combined with creative channel layouts, systems can be integrated to perform several chemical functions on a single device.

CHAPTER III

Transverse Migration of dsDNA in Microchannel Gel Electrophoresis

3.1 Introduction

Polyacrylamide gel electrophoresis of DNA is used in a wide range of applications including genetic analysis, mutation detection, disease diagnosis, and forensic screening. This separation technique has been adapted by the emerging lab-on-a-chip systems in recent years as a principal separation component of many microfluidic-based bioanalysis systems [70–74]. Cross-linked polyacrylamide is particularly attractive mainly due to its relatively short required separation distances as compared to other matrices [75, 76]. The resolution of these systems has been optimized by several means, including electrode-compaction injection, on-chip fabricated detectors, and the introduction of buffer flow [77–79]. The resolving power has been improved to a comparable level as that achieved by linear polymer solutions but at distances considerably shorter [80].

However, there are problems associated with cross-linked polyacrylamide. For instance, we have previously observed a loss in resolution for dsDNA bands larger than 200 bp in relatively dense gels (10%T) or dsDNA bands larger than 500 bp in less concentrated gels (5%T) [75, 79]. This reduction significantly limits the resolvable size

range of dsDNA especially in microfabricated devices with pre-loaded gels. Also, the microstructure of some cross-linked gels was found to be inhomogeneous, a phenomena that could be dependent on the monomer and cross-linkers concentrations as well as the polymerization process [81, 82].

Continuous 3-D visualization of electrophoretic motion in gels can aide in understanding these and other aberrant migration patterns. De Carmejane et al. have studied long-chain DNA (T2, 164 kbp) interacting with surrounding polymer fibers (0.38% HEC, 1X TBE) in a 3-D manner by taking spatially separated cross-sectional fluorescence images and reconstructing them into a 3-D image [83]. Advancements in microscope technology make continuous 3-D visualization (xyzt) possible. Confocal Laser Scanning Microscopy (CLSM), which has been widely used in the field of molecular biology, cell biology and colloidal particle research, was also used for the detection of ssDNA electrophoresis in a slab-gel and in a microfabricated disc [84, 85]. However, these studies were limited to the observation of ssDNA on the conventional detection plane (x-y). To our knowledge, dsDNA gel electrophoresis in cross-linked gels has never been observed on a transverse plane.

We observed dsDNA motion during electrophoresis in microfabricated glass channels using CLSM. Both cross-linked and linear polyacrylamide matrices were used as well as various lengths of dsDNA. To support and better understand our findings we also developed a reptation simulation model that predicts DNAs position in small-pore gel environments during electrophoresis.

3.2 Materials and Methods

3.2.1 Microchannel Etching

Two designs of microchannel geometries were used in experiments, as shown in Figure 4.1a. Design A was only used for dsDNA electrophoresis using linear poly-

acrylamide solution. Design B (Figure 4.1b) was used for electrophoresis of all other samples. Microchannels were etched on 500 μm thick, 4-inch borofloat glass wafers (Precision Glass and Optics, Santa Ana, CA, USA). First, wafers were pre-annealed in a furnace by slowly ramping the temperature to 600°C and holding it overnight. After annealing, 500 Åof chromium followed by 3500 Åof gold were deposited on the float surface of each glass wafer. The wafers were then spin-coated with Microposit SC1827 positive photoresist (Shipley Co., Marlborough, USA), patterned with the desired channel design and developed in MF319 photoresist developer (Shipley Co., Marlborough, USA). Metal layers were etched with gold etchant TFA (Transene Co., Danvers, USA) followed by CR-14 chromium etchant (Cyantek Inc., Fremont, USA). Glass features were then etched by immersing the patterned wafer into 49% hydrofluoric acid solution for 5-15 minutes to give a series of channel depths (with channel width equal to 50 μm plus two times the channel depth). The channel depth was measured by a stylus surface profilometer and was around 50 μm for a 10-minute etch.

3.2.2 Device Assembly

After the channels were etched, holes were drilled through the reservoirs on the glass side by electrochemical spark discharge. For devices assembled with glass-to-glass thermal bonding, 500 μm thick glass wafers with etched features and 100 μm thick Pyrex 7740 glass wafers (Sensor Prep Services Inc., Elburn, USA) were cleaned in 3:1 sulfuric acid/hydrogen peroxide solution for 25 minutes. Following, both pieces were soaked in potassium hydroxide solution (40% electronic purity) at 85°C for 15 minutes then liberally rinsed with deionized water. Then, the wafers were gently dried with nitrogen, pressed together by two Macor ceramic plates (Ceramic Products, Inc, Palisades Park, NJ) and thermally bonded in an oven for 5 hours at 560°C. Thermally bonded wafers were diced into individual pieces for use. Buffer reservoirs and fittings

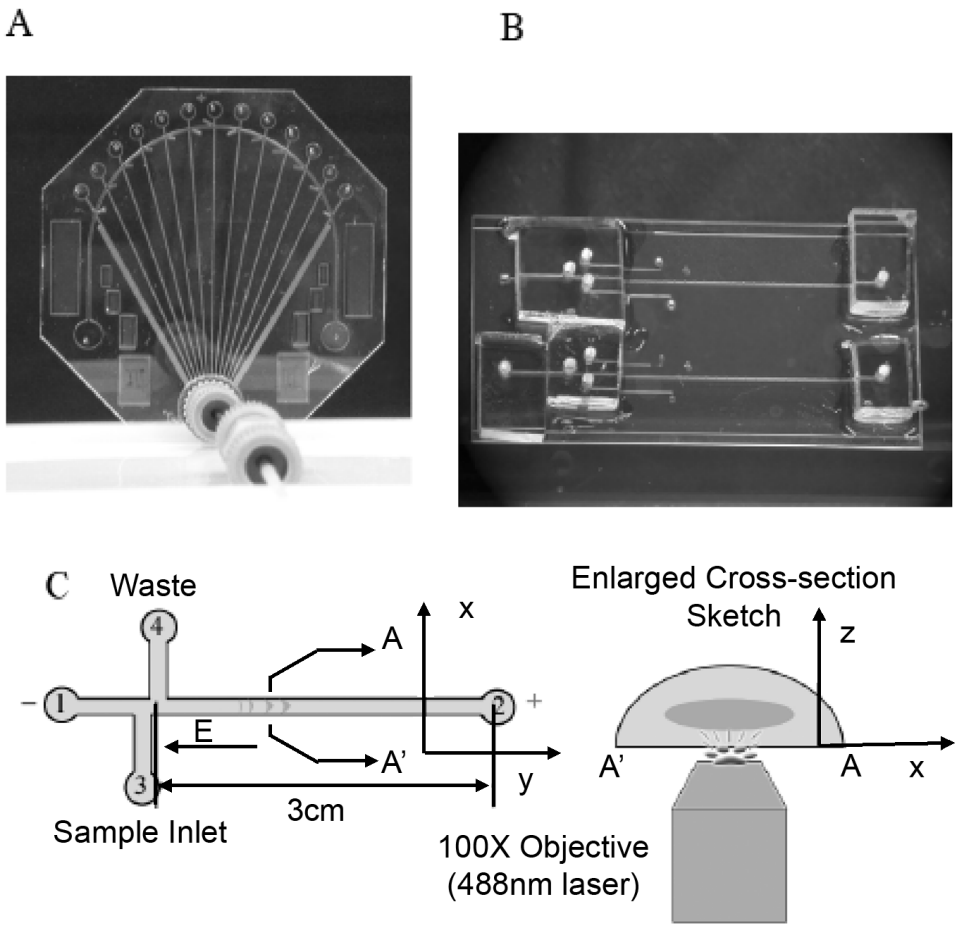

Figure 3.1: Images of the microfabricated devices used in the study of DNA electrophoresis with CLSM: (a) Design I; (b) Design II; (c) Sketch of confocal microscopy scanning mode and cross-section of microchannel with definition of coordinates: x-; y-length of the channel, z-depth of the channel.

for external electrodes were attached with SK-9 Lens Bond UV curable optical glue (Summers Optics, Fort Washington, USA). For devices assembled by UV-glue, glass wafers with etched features were first diced, then bonded to another piece of Pyrex 7740 with SK-9, and finally cured under UV-light. UV-cured devices were occasionally reused. To accomplish this, the etched glass side was separated from the bonded wafer and channels were cleaned by razorblade agitation along with water, ethanol and isopropanol.

3.2.3 Channel Treatment

Devices assembled by glass-to-glass thermal bonding were used without further cleaning. All devices assembled by UV-glue were rinsed with water followed by ethanol and dried by vacuum aspirator. All channels were pretreated following the protocol developed by Hjerten [86]. After channel treatment, the device was dried in a desiccator before use.

3.2.4 Gel Preparation

Polyacrylamide (8%T) was made from a mixture of ReprolGel^{TM} High Resolution Solutions A and B (Amersham Pharmacia Biotech, Piscataway, USA) according to the manufacturers instruction. Polyacrylamide gel of varying monomer/cross-linker concentrations was formed by diluting ReprolGel^{TM} High Resolution formula with 1X TBE buffer solution. For thermal studies, polyacrylamide with pre-mixed Rhodamine B was made by mixing 190 μL 8% ReprolGel^{TM} Solution A and B with 10 μL 0.4 mM rhodamine B (in 10X TBE buffer) to a composition of 7.6%T and .02 mM rhodamine B. Prior to UV-polymerization, freshly mixed monomer and initiator solution was degassed in a desiccator for 30 minutes. The solution was then loaded into the microchannel by pipette. A distinct gel interface was created following work previously published by Brahmasandra et al [77]. A model XL-1000 spectrolinker UV cross-linker (Spectronic Co., Westbury, USA) was used for UV-initiation and gel polymerization. The solution was first exposed to UV-light source for a 100 second pre-polymerization. Then, 10 μL 1X TBE buffer was added into the buffer tanks at both ends of the separation channel (Figure 4.1) to balance the ionic concentration and keep the gel interface moisturized during gel formation. For complete polymerization, an additional 600 seconds of UV exposure was applied. After gel polymerization, the chip was set with both ends filled with 30 μL fresh 1X TBE solution for at least 30 minutes until use. Linear polyacrylamide solution (LPA), 6%T, was degassed by

helium flow for 5 minutes and loaded into the microchannel by high pressure helium through tubing connections and NanoPortTM fittings (Upchurch Scientific, Inc., Oak Harbor, USA), as shown in Figure 4.1a.

3.2.5 Sample Preparation

20 bp and 100 bp dsDNA size-standards were commercially purchased (Bio-Rad, St. Louis, USA). Monodispersed dsDNA samples (343 bp and 462 bp) were amplified from mouse RNA by PCR and diluted with deionized water at a 1:5 ratio of DNA to water. dsDNA samples were labeled with YOYO-1 intercalating dye (Molecular Probes, Eugene, USA) at a volume ratio of 2:1 ratio of dye to DNA. All light-sensitive samples were kept in the dark after preparation.

3.2.6 LabVIEW^{TM} Controlled Injection and Electrophoresis

The electrophoresis apparatus included a computer loaded with LabVIEWTM software, data acquisition card, stage adaptor for mounting the chip on the confocal microscope stage, circuit connections and controls, a BHK-2000-20MG high-voltage power supply (Kepco Inc., Flushing, USA) and microfabricated devices. A LabVIEW^{TM} program was used for control of a three-phase, electrokinetic injection and electrophoresis process. A diagram of the system is displayed in Figure 4.1c. Prior to electrokinetic injection, a 0.5 μL sample, labeled with fluorescent dye, was loaded into port 3. To begin, a +20V potential was applied on port 4 for 2 seconds while ports 1, 2 and 3 were grounded to move the sample into the channel intersection area. Next, a +150V potential was applied on port 2 for 0.5 sec with port 1 grounded, to move the sample plug into the separation channel. Meanwhile, a +10V anti-leakage potential was applied on port 4. Finally, the +150V potential was kept on port 2 for sample electrophoresis towards port 2, while a +20V potential was applied on ports 3 and 4 to hold all uninjected sample at the intersection area and prevent tailing while

port 1 was kept grounded.

3.2.7 Detection with Confocal Microscopy

DNA and Fluorescein-Na electrophoresis were monitored by a Leica SP2 confocal laser scanning microscope (Leica Microsystems, USA) with a 100X/1.40-0.70 objective. The green fluorescent signal (YOYO-1) was excited with an Ar/ArKr laser (488nm) while the red signal (Rhodamine B) was excited with a He/Ne laser (543nm). A single or dual-channel transmission detector was used according to the detection needs. Xzt-scanning mode was used to scan the channel cross-section. The scanning speed was set at 400 MHz (1.68sec/frame), giving an image resolution of 512x512 pixels. Image gain and offset were adjusted to a proper level and kept constant for the rest of the detection. The motorized x-y stage was controlled either by a joystick, for fast movement, or knobs, for fine movement. Movement along the z-axis for scanning used the galvanometric z-stage controlled via software.

3.2.8 Image Process and Data Analysis

All the images were taken and digitalized by Leica confocal software (Leica Microsystems, USA). Image processing and profile plots were constructed with Photoshop v9.0 (Adobe, USA) and Matlab (Mathworks, Massachusetts, USA). Using Photoshop and Matlab, the intensity profile of the cross-section was plotted by selecting a measuring window, which is a rectangular covering the center area of the cross-section from the bottom to top of the channel. Subsequent distribution calculations of the extracted image were completed with Matlab.

3.2.9 Simulation of dsDNA Movement

dsDNAs transverse movement was simulated using Matlab software on a Pentium 4 desktop (Dell, USA). Random number generation was obtained from Matlabs rand

command. An electric field of 5 kV/m was used, corresponding to a 150 V potential across a 3 cm gap. The linear charge density used is 2 eV per base pair of DNA. The ambient temperature was set to 298 K, and the Kuhn length of dsDNA used was 100 nm.

3.3 Results and Discussion

3.3.1 Observation of Non-Uniform DNA Distribution

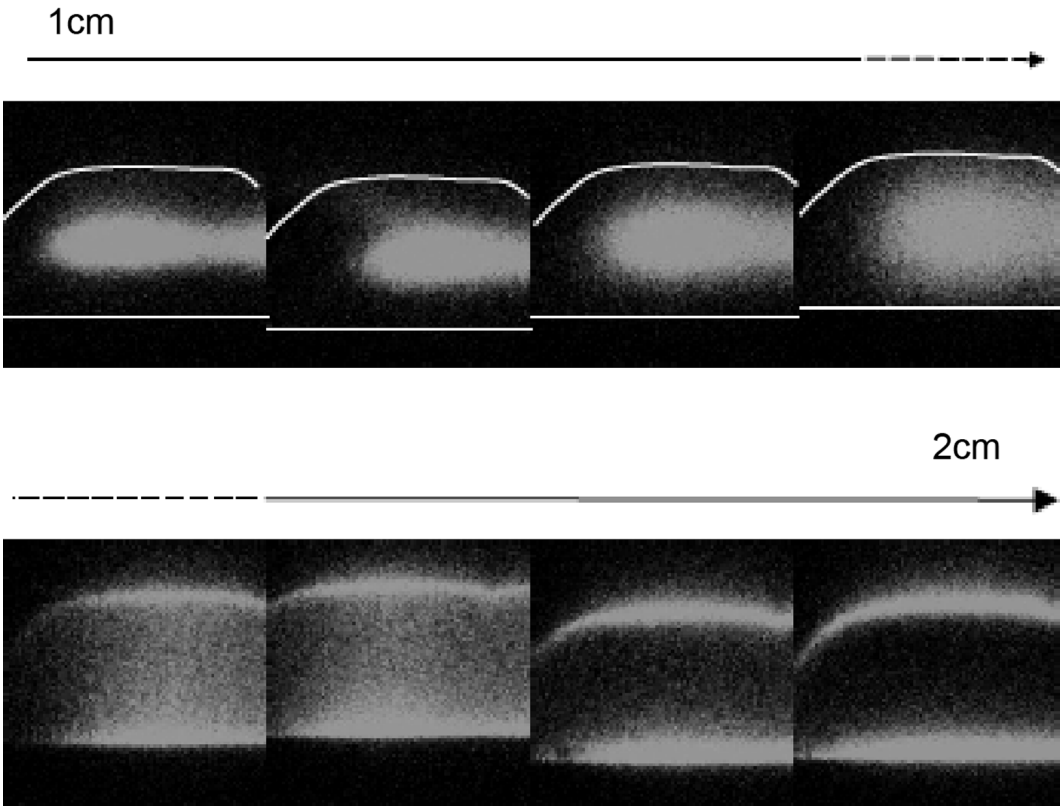

Figure 3.2: DNA distribution in the cross-sectional plane of the microchannel, and its net transverse movement as a function of y-distance (detected by moving the stage along DNA migration direction in 2min).

During electrophoresis, dsDNA is distributed non-uniformly in photopolymerized cross-linked polyacrylamide gels. We observed that as dsDNA migrates from cathode to anode it is initially concentrated in the center and then gradually separates to

the top and bottom of the gel. Figure 4.2 shows the cross-sectional migration of a 343 bp dsDNA band that displays this center-concentrated (1 cm from injection) to edge-concentrated (2 cm) transition. Similar distribution patterns were observed for both 343 bp and 462 bp dsDNA bands. This phenomena is a strong a function of DNAs migration distance and is not dependent on migration time.

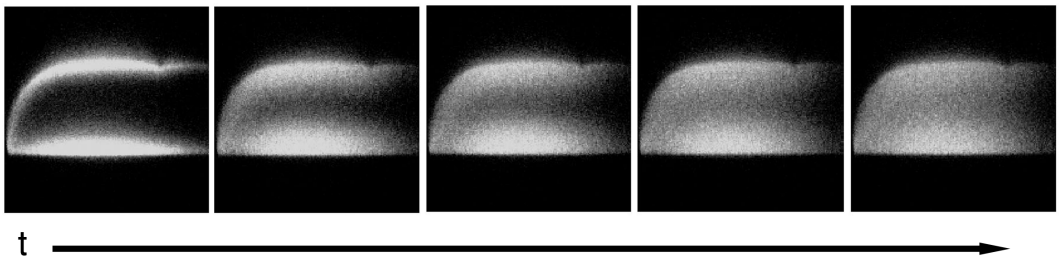

Figure 3.3: Images of self-diffusion induced distribution change when the electric field turned off. The first image is taken right after the turn-off of the electric field (e.g. $t_d = 0$ minutes) and each image is taken 1 minute after the previous one (e.g. the last image represents the distribution at the moment $t_d = 4$ minutes).

The non-uniform distribution is an active process and not a passive distribution. The edge-concentrated DNA distribution pattern of a 343 bp migrating band was monitored as the applied electric field was terminated. As seen in Figure 4.3, dsDNA immediately begins to diffuse into areas of lower concentration. In the absence of an electric field, distributed DNA patterns disperse in approximately 5 minutes. Once the field is reactivated, the DNA distribution pattern returned to its initial distribution state in both the center-concentrated (Figure 4.4a) and edge-concentrated perspectives. Note that the decay of the distribution, measured by each images variance of fluorescence intensity with respect to the vertical direction (Figure 4.4b), shows a first order decay. This functionality is different when the field is reapplied; the variance linearly increases with time.

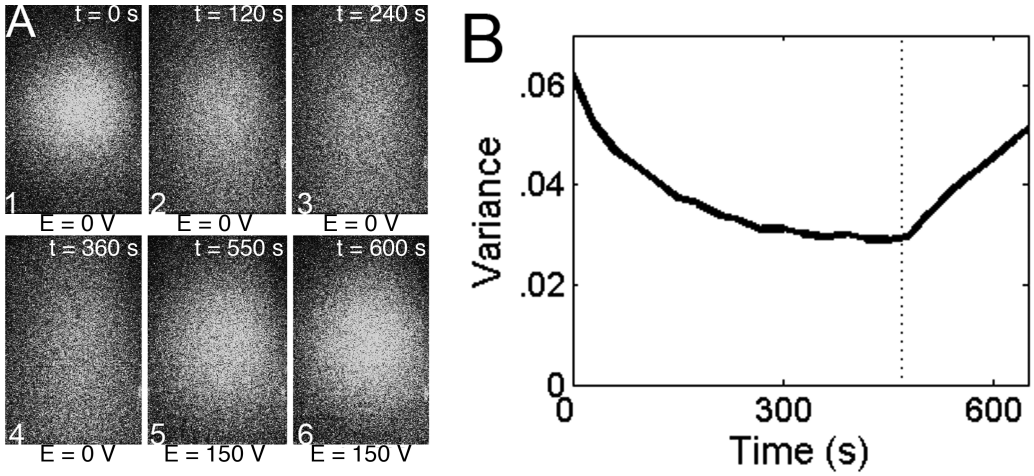

Figure 3.4: (a) Center-concentrated DNA pattern as a 150V electric field is cycles. At the first image the electric field is shut off, and half-way through the field is reapplied. (b) Variance of the images versus time. Fluorescence intensity was integrated across the width of the channel, then variance was calculated from integrated width intensity with respect to the height of the channel. The dotted line represents reapplication of the electric field.

3.3.2 Factors Influencing DNA Distribution

Interactions between migrating DNA and its surrounding gel matrix influence the distribution. We investigated several factors that might affect the migration of DNA including the DNA length, the cross-linking properties of the gel, the monomer density, electroosmotic flow, and the presence of any temperature gradients. For example, different dsDNA distribution intensities were observed using individual lengths of DNA ranging from 20 bp to 462 bp in addition to a 20 bp ladder. As seen in Figures 4.5a-d, 20 bp dsDNA strands whose lengths are on the order of the gel pore size migrate uniformly. However, as dsDNA length increases, DNA begins to migrate in a biased fashion. dsDNA, sized from 100 bp to 462 bp, display both a center-concentrated and edge-concentrated distribution bias as a function of migration distance. 100 bp dsDNA was less intensely concentrated along the gel edges than 343 bp and 462 bp strands. Note that in a more elastic network, such as 6% linear polyacrylamide solution (Figure 4.5e), we observed no concentration gradients.

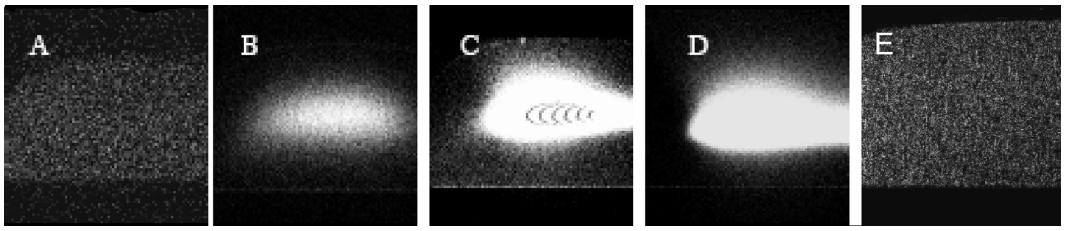

Figure 3.5: Various distribution patterns of dsDNA on the cross-sectional plane corresponding to the size of DNA strands and gel type. (a) 8%T 20 bp; (b) 8%T 100 bp; (c) 8%T 343 bp; (d) 8%T 462 bp; (e) 6% linear polyacrylamide 200bp. (a-d) are taken 1 cm downstream of starting point of the electrophoresis while (e) was chosen as a representative image.

The distribution of DNA was also a function of pore size. To vary pore sizes, gels with concentrations 7%T (larger pores) and 8%T (smaller pores) were used. Gel structures have been investigated by various groups and have been shown to have a bulk pore size, for these concentrations, ranging between 5 nm and 10 nm [37]. Displayed in Figure 6, 7%T (Figure 4.6a) and 8%T (Figure 4.6b) gels were observed to be center-concentrated at 1 cm. However, the transition from center-concentration to edge-concentration does not occur at the same distance for both systems. 2 cm after injection, in 7%T gel (Figure 4.6c), DNA is in a transition state similar to intermediate pictures seen in Figure 4.2, versus 1.5 cm for the 8%T gel.

Non-uniform DNA distribution does not appear to be a result electric field side effects such as electroosmotic flow or thermal gradients caused by Joule heating. To observe the effect of electroosmosis on dsDNA distribution, dsDNA migration patterns were studied in both a bare channel and in a channel coated to dampen electroosmosis. The distributions of a 343 bp dsDNA band were unchanged in both cases. This result can be attributed to the presence of the gel already restricting electroosmotic flow as well as the chemical similarity between the coating and the gel. Joule heating is another side effect of applying an electric field. Thermal gradients were measured using rhodamine B, a thermo-fluorescent dye. Initial fluorescence signals were compared to those taken 30 minutes after the 150 V electric current was

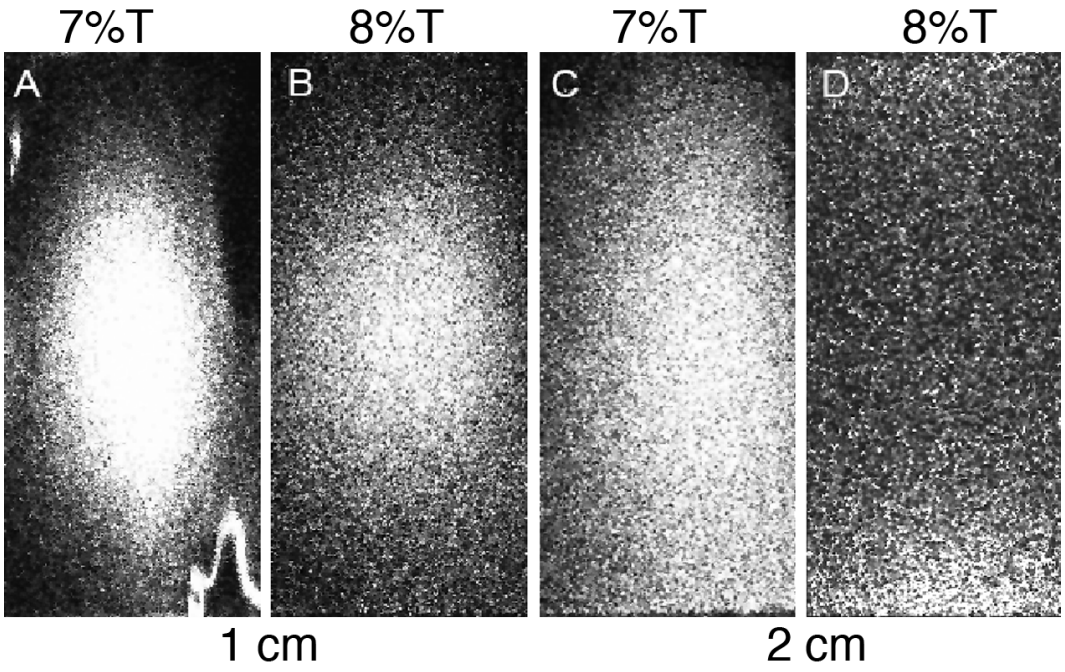

Figure 3.6: Distribution images of DNA migrating through both 7%T and 8%T polyacrlyamide gel. (a) 7%T 1 cm after injection (b) 8%T 1 cm after injection (c) 7%T 2 cm after injection; (d) 8%T 2 cm after injection

applied. There was only a slight decrease (8%) in the overall intensity, corresponding to less than 5°C increase in the gel temperature according to the slope reported by Ross et al [87].

3.3.3 Simulation of DNAs Transverse Movement

A simulation was developed that employs principles of the Biased Reptation Model (BRM) to aid in understanding the observed dsDNA distribution. The simulation models dsDNA as a strand made up of several interconnected segments [88]. Because dsDNA reptating through cross-linked polyacrylamide gel (pores 5-90 nm) has a Kuhn length (100 nm) larger than the gel matrixs pores, the motion is modeled as a rigid fluctuating head segment leading a number of other segments as they migrate through a gel [89–93].

A Boltzmann distribution based on bending and electrostatic forces determines

the probability of specific alignments of the dsDNAs head segment Equation 3.1):

$$p_i = p_{bend} \times p_{electro} \tag{3.1}$$

Where, p_i is the overall probability of a certain alignment, and p_{bend} is the directional probability based on the bending, ridgity and confinement of the DNA segment and $p_{electro}$ is the directional probability based on electrostatic alignment. p_{bend} can be described by Equation 3.2.

$$p_{bend} = \frac{exp(\sigma \Delta \hat{n}_i^2)}{\sum_{j=1}^{N} exp(\sigma \Delta \hat{n}_j^2)} \tag{3.2}$$

In Equation 3.2, σ is a dimensionless parameter that governs the bending force of a DNA segment and is equal to Equation 3.3 [91, 94, 95].

$$\sigma = \frac{b}{a} \tag{3.3}$$

b, is the persistence length of a DNA segment and, a, is the average pore size in the polyacrylamide gel. Higher values of σ represents a stiffer polymer or more highly confined polymer that requires a higher bending activation energy barrier. The $\hat{n}_i$ is a unit vector of alignment which will favor a polymer moving through a gel to stay straight and will discourage bending. The, $p_{electro}$ term can be described by Equation 3.4.

$$p_{electro} = \frac{exp(-\frac{\epsilon}{2}(1 - \hat{n}_{x,i}))}{\sum_{k=1}^{N} exp(-\frac{\epsilon}{2}(1 - \hat{n}_{x,k})} \tag{3.4}$$

where ϵ is a dimensionless parameter which describes the energy gain from electrostatic alignment and is shown in Equation 3.5.

$$\epsilon = \frac{qEa}{k_b T} \tag{3.5}$$

ϵ is a function of the segment charge, q, electric field E, pore size and temperature, T. [91, 94, 95]. The current alignment in the direction parallel to the applied electric field is preferentially favored in this case and is represented by $\hat{n}_{x,i}$.

This probability results from a strands change in energy from both disengagements with the electric field and bends between stiff interconnected segments versus thermal fluctuations. For each step, a new orientation angle and direction of movement is selected based on MatLAB random number generation versus the probability of selecting a corresponding alignment. Once an angle is selected, DNA is moved one segment length and the head alignment is reevaluated. At walls, DNA can sample fewer angles because of steric interactions, so the probability of choosing an impossible alignment is automatically set to zero. After a new alignment is chosen, the strand is moved in the direction of that alignment for one pore distance. This process is repeated for multiple DNA strands and timesteps.

Simulations show DNAs movement changes significantly between gel systems (50 μm channels) with different pore sizes (Figure 4.7). For small pores (5 nm, ϵ = .0022, σ = 16), the dsDNAs resistance to bending governs and results in slower, variable motion. For larger pores (80 nm, ϵ = .5632, σ = 1.25), the electrostatic forces dominate and the molecules align more with the field, resulting in quicker, more uniform movement. Trajectories of individual DNA molecules (data not shown) show that DNA exhibits more transverse movement in small pores than in large pores. This can also be seen in Figure 4.7, where the larger band dispersion in a small pore system is indicative of more transverse motion.

We simulated a binary-pore system and found that this produced both center-distributed and edge-distributed DNA patterns, similar to what has been observed. A binary-pore system was chosen because TEM imaging has shown that cross-linked polyacrylamide gel polymerized in enclosed glass channels form larger pores near the walls and smaller pores near the center [81]. In multipore systems, distribution results

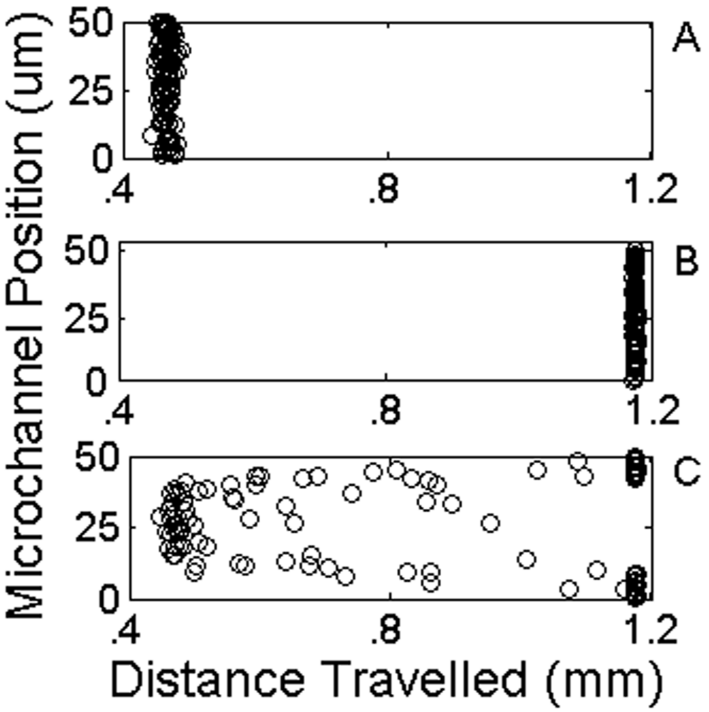

Figure 3.7: Images of 100 strands of DNA after t = 5 seconds in (a) 5 nm pores; (b) 80 nm pores; (c) 80 nm pores (10 microns on the top and bottom of the channel) and 5 nm pores (occupying the center 30 microns)

from DNA in small pores being more likely to migrate transverse to the electric field versus large pores which are more likely to align with the electric field. The results (Figure 4.7c) demonstrate that DNA on the edges travel faster and may be observed before the center DNA reaches a fixed detection point. As DNA migrates (Figure 4.8a), DNA in the smaller, center pores begins to move to the edges, creating a 3D, parabolic concentration gradient similar to what is observed in Figure 4.2. Also, the DNA distributes non-uniformly across the gel; the number of DNA molecules in the center decreases while the number of DNA molecules at the edges increase (Figure 4.8b). In addition to representing the confocal data, this simulated data also resembles separations performed earlier by Brahamasandra et. al., where they acknowledged the 2D parabolic shape to unpolymerized gel at the channel edges [77].

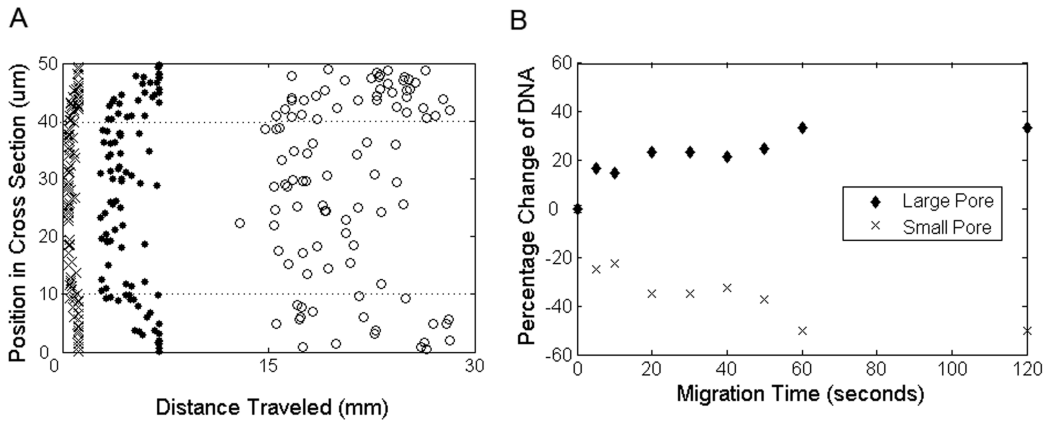

Figure 3.8: (a) DNA traveling through a stratified pore system over different time-lapses (×) 5 seconds; (•) 30 seconds; (○) 120 seconds. Dotted lines represent the large and small pore interface. (b) Number change fraction of DNA in large pores (⧫) and small pores (×) versus time.

3.4 Conclusion

We reported on our observation of transverse DNA electrophoretic migration in cross-linked polyacrylamide gel polymerized in microfabricated glass channels. With the primary gels we studied (8%T and 7%T in-situ UV-initiated cross-linked polyacrylamide), a center-biased pattern is observed for detection at a relatively short migration distance (1 cm) while an edge biased is observed at a longer migration distances (2 cm) for dsDNA. The distribution becomes weak or even disappears as the size of dsDNA decreases to the scale of the pore size or if a linear polyacrylamide solution is used. Our simulations show that a multipore gel with large pores near the walls and smaller pores in the interior will produce an edge-concentrated and center-concentrated DNA pattern. This preliminary result is also consistent with the observation that as the pore size increases (i.e., monomer concentration decreases), the transition from center-concentration to edge-concentration becomes more gradual. In addition, the observed DNA distribution is an active process (Figure 4.4b) and an inhomogenous gel may be a contributing factor. Although the experimental and simulated results coincide fairly well, neither accounts for the reversibility of DNA

distribution or the absence of the edge distribution at shorter (1 cm) distances. An initial attempt has been made to understand the complex phenomena presented here. However, there are many additional experiments and simulations that need to be performed before the exact causes of the observed DNA distributions can be stated with confidence. For instance, high-resolution imaging of the gel pore structure would help corroborate or negate the pore size arguments. In addition, other parameters such as electric field gradient and nonhomogeneous field gradients in the channels could be explored. Hopefully, additional studies will elucidate the exact cause of the nonuniformities and allow the design of more versatile and higher-resolution separations in microfluidic devices.

CHAPTER IV

Selective Arraying of Complex Particle Patterns

4.1 Introduction

Precise and accurate positioning of micro- objects, such as cells and particles is a recurring and central theme in a wide range of disciplines including biology, tissue engineering and self-assembly. For example, by isolating bacterial communities in microwells, Kim, H. J. et. al. recently showed that micro- spatial structure within microbial communities influences growth, competition and stability [96]. The intercellular structure of human liver tissue affects its efficacy and by positioning hepatocytes and endothelial cells, more viable liver tissues were created [97, 98]. In addition, cells, such as *C.Elegans*, have been isolated from a general population for individual interrogation [99, 100]. To generate uniform anisotropic particles for self-assembly, work has been dedicated to accurately patterning particle precursors using surface tension, optical tweezers, convective drag and magnetic fields [101–104]. Although all of the mentioned work was developed because the authors can generate desired structures, these methods encounter difficulties when additional features are desired. For instance, using surface tension for particle and cell positioning is accurate, but is dependent on solvent properties, is unresponsive and can result in cells exposed to air for periods of time.

There has been considerable effort to unify intricate and complex object place-

ment with flexible and responsive arrayed control using convective flow in microfluidic devices. Tan, W. H. et. al. created a system which quickly positions functionalized particles into large-scale microparticle arrays [40]. More recently, using a similar concept and a three-step flow scheme, Skelley, A. M. et. al. showed how a massive number of cells could be quickly paired for electrofusion [39]. In addition, there is a vast library of work on both chemically and physically controlling cells and particles in microfluidic devices [38, 105, 106]. However, these microfluidic channels are often planar and therefore fluidic placement results in single particle placement or consequential multi-particle patterning. Although single particle placement is used for experiments requiring simple object interrogation, expansion to more complex patterning will require a different approach to attain.

We have developed a novel method to rapidly, precisely and accurately position individual objects, such as particles, in any two-dimensional shape, spacing and frequency. Using glass and silicon microfabrication techniques, we constructed a system that uses laminar flow to position particles into complex patterns with single object resolution. With objects smaller than 5 microns were patterned with multiple object resolution. An extension was made in the fabrication and operation process to independently control particles thus increasing the scope and versatility of the microfluidic system. Furthermore, since the device operates using convective pressure-driven fluid flow, we have shown its versatility with a wide range of samples with few operational changes.

4.2 Materials and Methods

4.2.1 Device Fabrication and Construction

Devices are microfabricated with UV-lithography technology in a Class 100 cleanroom environment (Figure 4.1). Both single-control devices and multi-control devices

are fabricated on 500 μm thick double-side polished (100) silicon wafers. Wafers were front-side spin-coated with 3 μm of PR1827 photoresist and were soft-baked for 60 seconds at 110°C. The wafer was then exposed with a low vacuum contact mode using an SUSS MicroTec MA-6 mask aligner for 13 seconds and developed in MF-319 developer for 50 seconds and rinsed with DI water for 1 minute. Drains were etched with an STS deep reactive ion etcher for 35 minutes. Photoresist was then stripped in hot PRS-2000 positive photoresist stripper for 5 minutes. From this point, single- and multi- control device fabrication differs. The single-control devices were backside coated with 12 μm of AZ9260 photoresist and soft-baked for 4 minutes at 110°C. Using a SUSS MicroTec MA-6, the wafer was backside aligned, exposed with the backside pattern for 50 seconds under hard contact mode and developed in 4:1 H_2O:AZ400k for 3 to 4 minutes. The wafer was then backside mounted to a carrier wafer with PR1827 followed by a 20 minute bake at 110°C. The wafer was etched until the drains were exposed, typically for 85 minutes. The wafer was released from the carrier wafer using PRS-2000 for 20 minutes. The wafer was then diced using a dicing saw to release individual devices.

Multi-control devices are front-side spin-coated over the drains with 3 μm of PR1827 and baked for 1 minute on a 110°C hotplate. Using a SUSS MicroTec MA-6, the wafer was front-side aligned, exposed for 13 seconds under low vacuum contact mode and developed in MF-319 for 50 seconds to create the control line pattern. This pattern is then etched for 7 minutes in the STS deep reactive ion etcher. Photoresist is stripped in PRS-2000. The silicon wafer and a borofloat glass wafer are cleaned in piranha solution (3:1 sulfuric acid:hydrogen peroxide) for 20 minutes, then rinsed in DI water. Both wafers are then sonicated in acetone and isopropyl alcohol for 1 minute each and dried with filtered nitrogen. The surfaces were then activated with nitrogen plasma (500 W, 2 treatments) from a SUSS nP-12 surface activation system. The glass and silicon are anodically bonded (feature to glass) with an SB-6E bonding

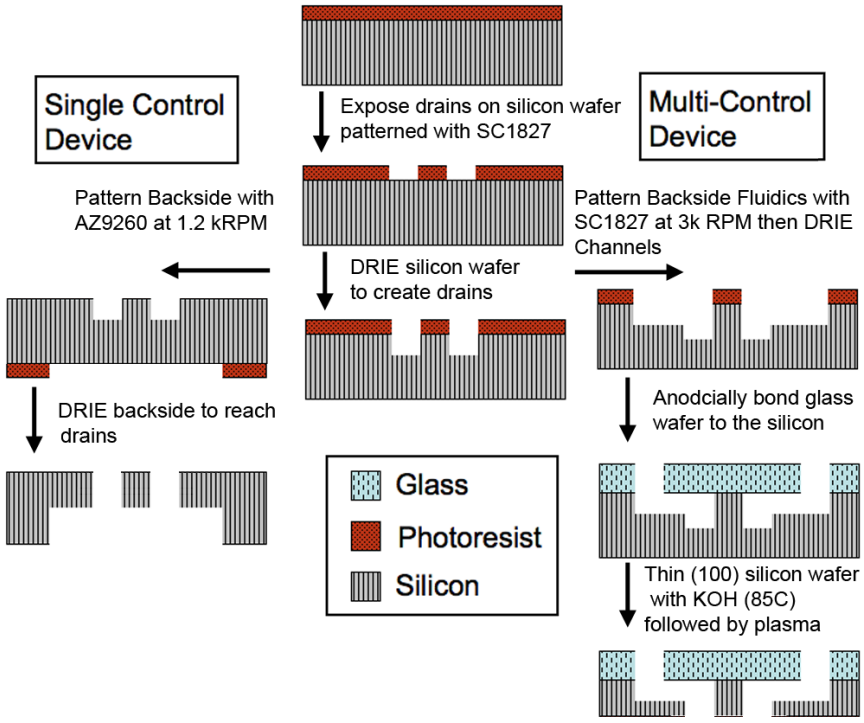

Figure 4.1: Fabrication diagram for both classes of devices for creating single component patterns or multi-component patterns. Both fabrication layouts begin the same with etching the high-resolution drain features.

unit (T=250°C , P = 10^{-4} Pa, V = -1000 V). The silicon substrate is then thinned with hot KOH (85°C) until large features are exposed. Fine control of the wafer thinning is finally completed with the STS deep reactive ion etcher until drains are exposed. The devices are then released using a dicing saw.

Glass fluidic layers are microfabricated by depositing 500 $\AA$ /3500 $\AA$ Cr/Au on piranha cleaned borofloat glass wafers using a PVD enerjet evaporator. 3 μm of PR1827 are then spin-coated and baked for 1 minute on a 110°C hotplate. The wafer is exposed with a MA-6 mask aligner for 13 seconds under hard contact mode and developed in MF-319 for 50 seconds. Gold is etched in TFA gold etchant followed by CR-14 chromium etchant. Channels are etched in HF (49%) until a desired channel depth is reached. Wafers are stripped with PRS-2000 followed by gold etchant then chromium etchant. Individual devices were released from the wafer with a dicing saw

and holes were drilled using an electrochemical spark discharge.

Prior to assembling devices, each piece is cleaned in a cleanroom environment by sonication for 1 minute in acetone followed by isopropanol. Individual pieces are assembled top-side glass to silicon followed by back-side glass to the glass/silicon by slowly wicking NOA-61 UV-curable adhesive (Norland Products). Adhesive is cured by UV-light exposure for 10 minutes each side. Fluidic connections were attached by gluing connection pillars with UV-curable adhesive, adding an 18 gauge precision tip into the connection and sealing it with epoxy followed by a 12 hour age at 80°C.

4.2.2 Fluidic Setup

Devices were controlled with a custom built fluidic system attached to a house pressure and vacuum source. Pressure was controlled by an electronic pressure regulator which leads to the inlet fluidic connections which could be controlled with a flow constricting clip on PTFE tubing. Flow was introduced from a sealed water source and filtered several times to ensure a contaminant-free solution. Vacuum was controlled with a marked needle valve, which could be set to restrict flow. Devices were imaged on a Karl Zeiss Axioskop with both 10x and 20x objectives with both bright-field and dark-field. Videos and images were directly saved to an attached hard drive.

Particles used were precision size standard 20 μm diameter polystyrene particles (Polysciences, Precision Size Standards), 10 μm diameter polystyrene particles (Polysciences, Polybead) and 20 μm diameter polymethyl-methacrylate partices (Fluka). Yeast cells used were.

4.2.3 FEM Simulations

FEM simulations were performed using COMSOL Multiphysics incompressible Navier-Stokes package. Water (ρ=1000 kg/m^3 , μ=.001 Pa-s) was used as the medium

and data was interpreted and graphed using MATLAB software.

4.2.4 Cell Culturing and Monitoring

Both *S.Cerevisiae* and *S.Ludwigii* cells were cultured in YPD growth solution. Standard autoclave and sterile laboratory practices were used while handling cells. After positioning cells, the inlets and outlets were closed, and cells were left in the device with YPD solution and grew unagitated for discrete periods of time. Cell number was calculated by transforming the image in Adobe Photoshop with the equalize, posterize and threshold functions to create a clipping mask on the original image. Images were subsequently analyzed in MATLAB.

4.3 Results and Discussion

4.3.1 Surface Patterned Device Concept

Multilayer microfluidic drain arrays convectively move particles onto precisely positioned holes (drains) across the device surface. The device has both a top side and a back side glass fluidic layer encasing a patterned silicon substrate as diagramed in Figure 4.2. Top side fluidic layers include a serpentine microfluidic channel (100 μm high) to direct flow over the drains, a fluid inlet and an outlet. The back side fluidic layer is a chamber (150 μm high) that actuates the device drains. Fluidic layers interact through the particle drains fabricated on silicon substrate. To load the drains, particles are introduced into the device as a dilute particle-liquid suspension from a positive pressure source while the outlet port is open to atmospheric pressure and vacuum is applied to the back side of the device. Since the particles are larger than the designed size of the drain, particles passing near a drain are trapped. A trapped particle will lower the hydraulic diameter of the drain, increasing the drains resistance to flow, thus decreasing the drains effect on other particles. Once a particle

suspension has been adequately loaded, additional particles are swept away to the device outlet by both increasing fluidic resistance of the drains and increasing the top side flow.

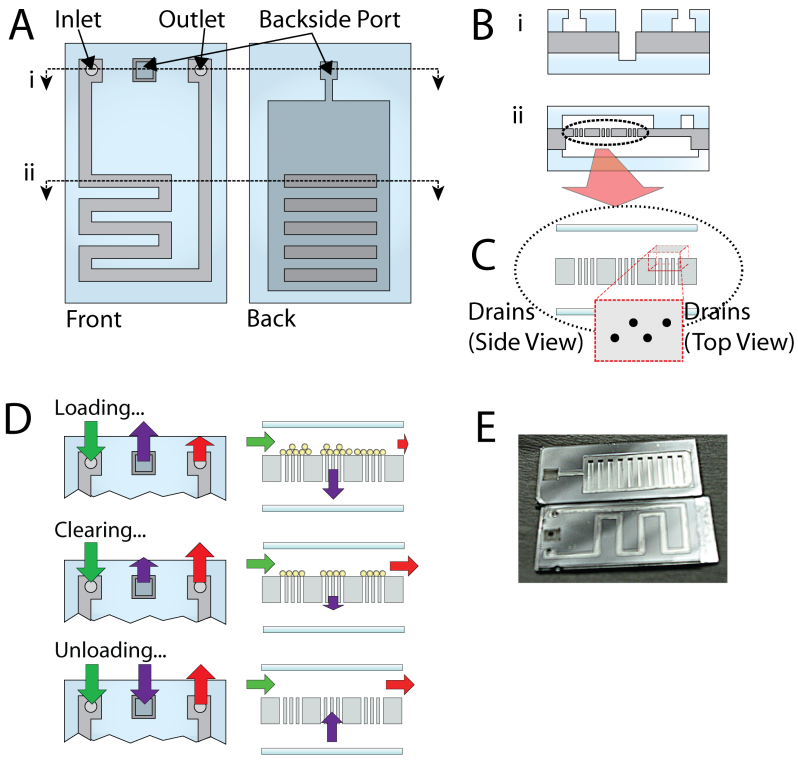

Figure 4.2: Overview and operation of the multilayer microfluidic device for positioning objects. (A) Diagram of the front and back of a multilayer microfluidic device. (B) Cross sections of selected areas from Figure 4.2A. (C) Magnified cross-section of the drains from both the side view and top. The top view image demonstrates the two-dimensional drain placement. (D) Several major operational modes. In loading, flow is restricted out the outlet which a majority of flow occurs at the inlet (positive pressure) and back side (vacuum). For clearing, flow is applied at the inlet while the outlet is opened to atmospheric pressure and the vacuum is constricted. Unloading, pressure is applied at the inlet and back side, while the outlet is open to atmospheric pressure. (E) Actual device image.

Fluid flow through drains is affected by particle presence, inlet pressure, vacuum and the back side fluidic resistance. We characterized this flow by measuring the liquid flowrate exiting the top side versus the liquid flowrate exiting the back side

in a device with 950 drains. The ratio of top side to back side flow appears to be uniform experimentally (Figure 4.3A). Simulations show that at decreasing inlet pressures, flow ratio drastically increases, attributed to nonlinearities of flow in the system. This could not be replicated experimentally because as pressure is decreased, flow decreases resulting in larger measurement errors. However, in the flow regime of interest flow ratio was uniform. After loading particles, the flow ratio increases, favoring a slightly lower flow rate through the drains. This result was more mild than expected and simulations show that, although particles may obstruct the drain flow, the location and intensity of the pressure drop in the system is never directly across the drains (Figure 4.3B). To drastically alter the flow ratio, to favor either high drain flow (loading) or low drain flow (clearing), we changed the resistance to flow through the drains, with an external needle valve. Depending on the resistance of the top side and back side channels, the device operated in difference regimes. For instance, as seen in Figure 4.3C, with high resistance of both the top and back sides, the flow ratio occurs below 1 for all cases, creating a device with easy to load drains, but hard to clear drains. However, as the resistance to the topside flow is decreased, the device begins to operate in a more variable mode that allows for controlled loading.

4.3.2 Rapid Arraying Capabilities

Using convective flow and arrayed drains, particle patterns of any arbitrary shape could be designed and constructed. For instance, Figure 4.4 shows a 100 unit array of a repeating 3 x 3 pattern of 5 μm drains (i.e., 900 total drains). The devices were fabricated with three different drain spacings: 10, 20 and 40 μm center-to-center. 10 μm polystyrene particles could be rapidly and precisely positioned on top of the drains. As long as the inter-drain spacing was greater than the particle diameter, the particles could be patterned on the substrate with a relatively high accuracy. However, as drain spacing approaches the average particle diameter, polydisperse

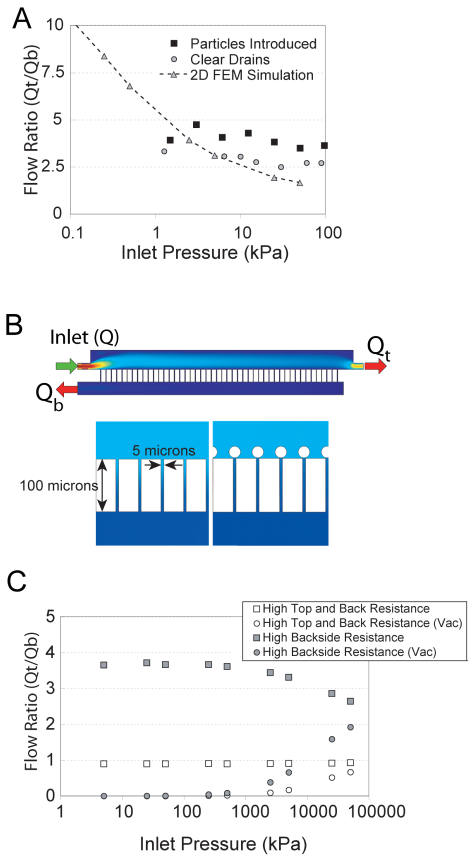

Figure 4.3: Characterization of fluid flow and drain loading. (A) Experimental fluid flow characterization graphs of flow ratio (top side flow versus back side flow) versus applied inlet pressure. Data compared devices with and without 20 μm particles positioned. The dotted line is COMSOL simulation data of a 2D system, diagramed in 2B. (B) COMSOL simulation layout diagramming simulation conditions. Zoomed in scenario with and without particles displays a pressure surface plot, while the overall schematic is a velocity surface plot. (C) Flow ratio in two systems be constricting topside and backside flow at varying flow conditions.

particle samples degrade a drains ability to limit fluid flow and result in aggregation of additional, unwanted particles (Figure 4.4C).

Particle loading and unloading can be achieved in seconds. Pressures of around 50 kPa at the top inlet and -30 kPa (i.e., partial vacuum) on the bottom chamber were used to introduce and trap the particles. These pressures result in an observed loading time of around 2 seconds (Figure 4.4D). Changing pressures and inlet solution

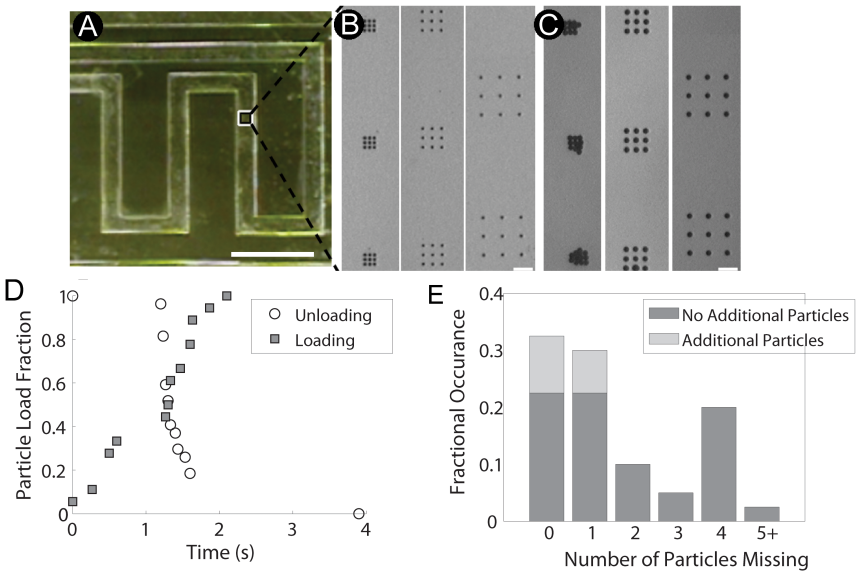

Figure 4.4: Loading particles in a 3x3 drain structure. (A) Stereoscope image of the array device and serpentine microchannel. (B) Enlarged image of the box showing arrayed 3x3 drain formation of 5 μm drains pre-particle loading. Drains are spaced 10, 20 and 40 μm apart. (C) Drains post particle loading with 10 μm polystyrene particles. Steric particle interactions result in additionally aggregated particles in the 10 μm spaced case. (D) Graph of fraction of 10 μm polystyrene particles loaded and unloaded versus time in a 3x3 array microfluidic device with respect to the viewing window. 18 drains are imaged in the loading case, and 27 drains are imaged in the unloading case. (E) Sample loading fraction from 40 sets of drains in a 3x3 drain system. (360 drains) Scale Bars: (A) 5 mm (B,C) 40 μm.

particle concentration can manipulate this loading time. Increasing particle concentration could conceivably have a negative effect on particle loading, although this was never observed in device operation. Excess particles were convectively ejected from the system by constricting the flow through the drains using a needle valve on the back-side outlet while keeping a steady fluid flow across the top of the drains. However, all extraneous particles were not cleared after this, perhaps because of surface interactions or improper seating of particles on drain openings. Complete particle removal and replacement is achieved by simply applying a positive back-side pressure along with a positive top-side pressure. Often, if all particles are not fully unloaded,

air can be introduced in the system to facilitate particle unloading. Unloading occurs as rapidly as particle loading (Figure 4.4D). We have also repeatedly used the devices by unloading the device, switching the particles, and reloading without any modifications to design or operation. Loading and unloading is identical with both large (20 μm) and small (10 μm) particles because particles load based on convective drag, which is uninhibited by the presence of a dilute particle suspension.

Particles (10 μm polystyrene) loaded on the 3x3 array surface were quantified over 40 different sets of 3x3 arrays, or 360 drains (Figure 4.4E). In the quantified run, 86% of the drains were occupied by particles and 95% of the positioned particles were in desired positions. However, only around 25% of the 3x3 patterns were perfectly formed. Considering 9 particles must be appropriately placed in order to create a perfect pattern, approximating this as the probability of 9 independent positioning the probability of an appropriate particle placement without aggregating additional particles is $.25^{1/9}$ or 86%. We noticed particle loading errors were often systematic within a given device rather than random, suggesting that uninhabited drains were caused by clogging or fabrication errors. Surface interaction and surface adhesion can also affect the complacency of particles to be swept away. We have tried different solvents with lower surface tension to move particles and noticed particles are more easily swept away. Surface charge on particles should not affect initial loading since convection governs this property, however it is foreseeable that charged particles may aggregate and compromise the system integrity. Salts and surfactants could be used in conjunction with fluid flow to address this potential materials problem. Finally, particle size versus drain size could be optimized to create more favorable loading conditions.

4.3.3 Accuracy and Precision in Object Placement

Particles were convectively positioned onto drains, creating particle patterns that accurately reproduce the pre-designed drain pattern Figure 4.5. We created particle patterns with 20 μm diameter polystyrene particles including compact triangles, high aspect ratio 5-mer particles and rings. With spherical particles and cylindrical drains, the minimum energy of a particle is at the center of each drain, and individual non-interacting spheres reach this minimum. However, observed deviations from optimal positions arise from both contact adhesion deformation and volume exclusion interactions. Position change from contact adhesion, on the 20 μm particle scale is very small and would be reasonable to neglect while volume exclusion interactions is variable between designs and is a function of particle polydispersity and drain spacing [107]. Measured deviations were around 3% the particle diameter for 5-mer patterns.

We quantified drain loading efficiency by measuring the number of particles correctly patterned versus particles erroneously patterned (Figure 4.5E). The device used were sets of 5-drain arrays with drains spaced by 20 μm, and loaded with 20 μm polystyrene particles. Each drain set occupied a unit cell spacing of 100x200 μm and can extrapolated to pack 5000 drains sets/cm^2. Most of the 5-drain arrays were fully filled with particles, and there were very few patterned with less than 3 particles. We see that 97% of the drains (of 335 drains) were occupied by particles and 86% of immobilized particles were appropriately placed, which is 9% lower than in the 10 μm non-interacting particle case. A majority of 5-drain patterns did not have unwanted particles. About 57% of the observed patterns were perfectly formed, and approximating this as the probability of 5 independent positioning the probability of an appropriate particle placement without aggregating additional particles is $.57^{1/5}$ or 89%, a very similar number to the non-interacting 10 μm particle case. Several drain arrays were discarded from the statistical analysis because there was a region

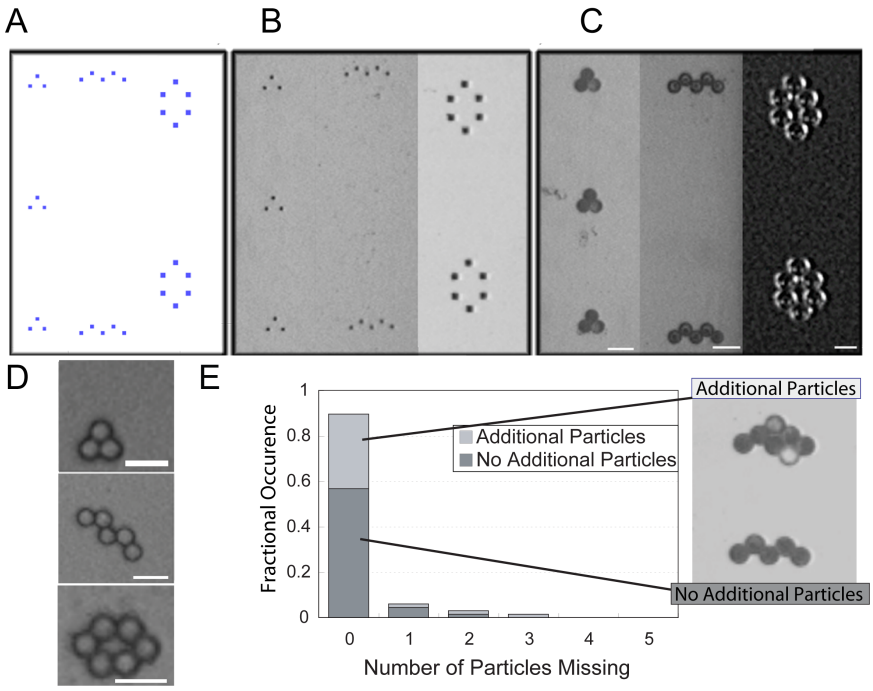

Figure 4.5: Procedure for precisely positioning particles in contact. (A) Computer design of different drains. (B) Drains fabricated on a silicon substrate (C) Particles (20 μm) convectively pulled into precise positions, forming tightly packed patterns. (D) Fused 20 μm polystyrene particles including a triangle, 5-mer zig zag and a ring. (E) Loading fraction in the case with 67 5-mer drain sets (335 drains). Scale Bar: 40 μm

of not fully formed drains caused by fabrication issues.

4.3.4 Particle Bonding

Particle patterns formed in this manner can be fused to create anisotropic particle assemblies. By positioning particles in contact (drain spacing equal to particle diameter) and heating them above the glass transition temperature, we are able to make many two-dimensional particle shapes with unique anisotropy. (Figure 4.5D) This technique is particularly attractive because the fused particles can be made in an assembly line type fashion, using the same device to create multiple sets of identical particles in parallel. With further development, these devices could be used to

create particles that self-assemble functional structures or be used as advanced drug carriers [108, 109].

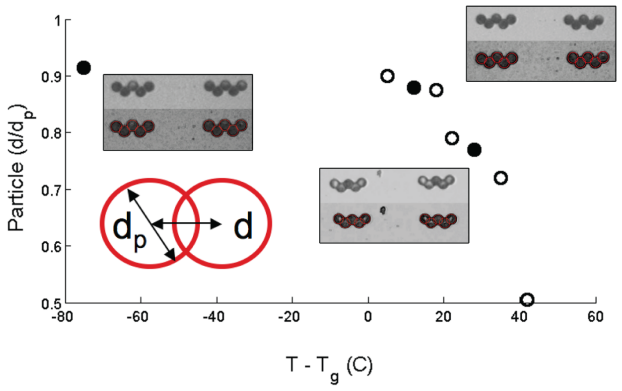

Figure 4.6: Adjacent particle coalescence d/d_p measured as a function of the temperature of the particle. Inset particle pictures correspond to filled points.

To properly bond particles, the thermal bonding of adjacent polymeric particles was investigated. By heating particles past their glass transition temperature, the polymer relaxes and becomes softer. This also increases surface energy between particles. The two effects of relaxed polymer structure and increased surface energy between these two attractive particle surfaces causes particles to deform. Particle begin to coalesce to reduce surface area while still keeping their structure intact. This deformation causes bonding of the polymeric particles [107, 110]. The degree of bonding was measured by quantifying the degree of deformation. However, relating bonding and coalescence is not entirely accurate, because once surfaces coalesce diffusion of polymer molecules across the surface adds a time dependent component to the strength of the formed bond.

Seen in Figure 4.6, as temperature increases past the glass transition temperature, particles being to show greater coalescence. Coalescence was measured by comparing the distance between particles centers, d with the diameter of an individual particle, d_p. Equation 4.1 was used to quantify this. In Equation 4.1, 1 and 2 represent two individual particles, x and y are the cartesian coordinates of the particle centers and

w and h are the width and height of a circular fit to each particle. The circular fit can be seen from the insets in Figure 4.6. Also, black dots in Figure 4.6 are the points corresponding to the poster particle pictures. At temperatures below the glass transition temperature ($T_g = 95°C$ for polystyrene), the change in particle diameter is negligible. However, after the glass transition temperature the particle size changes steeply with temperature. At around T=135°C (T-T_g = 40°C), particles begin to deform and adhere to the silicon. At this point, particles also begin to lose the "zig-zag" shape and deform to a rod.

$$\frac{d}{d_p} = \frac{4\sqrt{(x_1 - x_2)^2 + (y_1 - y_2)^2}}{w_1 + h_1 + w_2 + h_2} \tag{4.1}$$

4.3.5 Positioning Complexity

In order to create more complex patterns of both custom geometry and composition, the back-side of the device was modified to independently actuate drains (Figure 4.7). Two groups of control lines were added, allowing the individual control of two sets of drains. Drains were actuated by either applying vacuum or pressure to produce either a captured particle on a drain or a clear drain, respectively. Note that, with additional complexity such as a routing fluidics layer, more than two control lines can be used.

A demonstration of this concept in Figure 4.7 using a 5-drain system where both 2- and 3- drains are individually controlled. 5 μm drains were positioned 20 μm on-center and each set of drains were independently actuated, as shown in Figure 5C. Many different complex particle patterns can be obtained by independently controlling sets of drains. For example, a ring was made (Figure 4.7C) with the center particles controlled independently of the end particles. The control lines can be changed to accommodate any drain control scheme or positioning. In addition, the multi-component device could be used for creating even more complicated anisotropic

particles with varying composition and functionality.

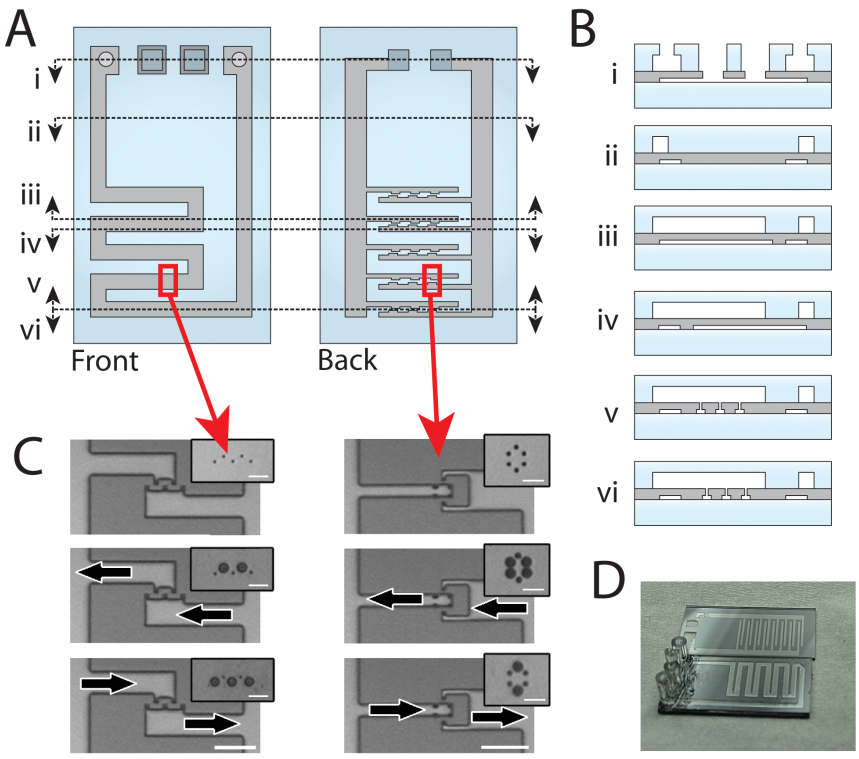

Figure 4.7: Methodology and demonstration of controlling particles individually. (A) Design of the front and back side of the device. (B) Cross sections of the multi-control device demonstrating the ability to individually actuate two sets of drains. (C) Zig-zag drain and ring drain with the backside (large) and topside (small) demonstrating the independent control. Arrows represent fluid actuation. (D) Still device image. Scale Bars: (A) 1 cm (B-D) Drains - 40 μm, Backside - 80 μm

4.3.6 Small Particle Aggregation

The multilayer device performed well with most particles. Polymeric particles of different composition (PS and PMMA) and size (10 μm and 20 μm) have been loaded into the device without any complications, and there are few foreseeable problems with particles of other materials. However, difficulties can arise from using non-spherical objects and objects smaller than the diameter of the drains. We have collected both glass microfibers and small (3-4 μm, Figure 6) non-spherical yeast cells (*S.Cerevisiae*

and *S.Ludwigii*) by forcing the objects to pack at the drain entrances. The objects do not seal the drains as they would for larger particles, but form aggregates at the top surface. For accurate single-particle positioning, the drain diameter must be smaller than the object size.

For biological systems, the aggregated cells can then be cultured. *S.Ludwigii* yeast cells were grown on a 3x3 drain array pattern (40 μm drain spacing) with a large chamber replacing the top-side serpentine channel. These cells are non-spherical, with the cell diameter being variable but smaller than the drain width. Thus, loading the cells onto the device formed cell aggregates around the drain openings. We were able to concentrate cells and dictate initial positioning and growth patterns (Figure 6B). We observed growth discrepancy between different cells; it appears that many clusters of cells did not bud. In addition, we noticed that growth occurs in three-dimensions, with clusters growing parallel and perpendicular to the substrate. By quantifying cell number on each array versus time, cell growth rates could be extracted (Figure 6C).

4.3.7 Miniaturization Limits

Drain miniaturization can be complicated by fluidic resistance increasing as the drain size decreases. Typically, for uniform conditions, flowrate through a circular pipe scales by the diameter, d, to the fourth power. Therefore, understanding the time it will take to flow a set volume of fluid through the drains is important. This can be very useful to design systems that can handle smaller particle sizes and microfabricated features.

The time, t, to drain a volume of fluid, V, is inversely proportional to the flowrate through the drain, Q_v (Equation 4.2).

$$t = \frac{V}{Q_d} \tag{4.2}$$

The flowrate can be estimated by the Pousille flow equations, Equation 4.3.

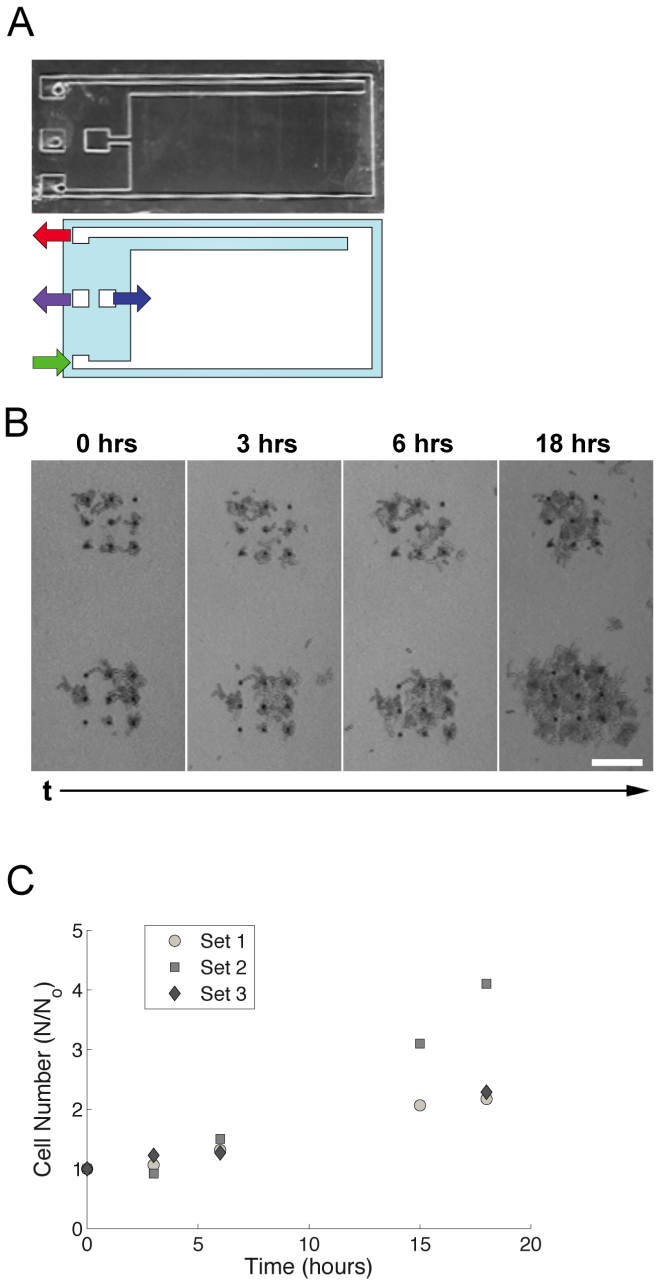

Figure 4.8: Culturing S. Ludwigii yeast cells in an alternative fluidic arrangement. A) Alternative design of an open box flow design which was used to culture cells. (B) At $t = 0$ hrs, *S.Ludwigii* cells were loaded in a 3x3 array with a box top side fluidics. All top side and back side fluidics are closed and the cells are given time to grow and culture. Time progression shows areas of cell growth and stagnation. (C) Normalized intensity of cell (*S.Ludwigii*) growth for 3 sets of drain arrays on the same run. Sets 1 and 2 are images in (B). Scale Bars: 40 μm

$$Q_v = \frac{\pi d^4}{128 \mu L} \Delta P \tag{4.3}$$

Where ΔP is the pressure differential across the drain (in this case we use 1 atm), μ, is the viscosity of the fluid (water) and L is the length of the drain (40 μm). The volume that each drain will flow is calculated by setting the density of the drains, ρ_d and height of the channel containing particles, h, seen in Equation 4.4. This is not the volume needed to position a particles, but should give a rough estimate of a time constant for a channel to drain a given volume a fluid.

$$V = \frac{4h}{\rho_d} \tag{4.4}$$

The ρ_d term is in units of drains per area. The maximum packing is where the drains are touching, so a density of $\frac{1}{d^2}$. As drains are spaced further a packing fraction, R, can be used to scale this. However, this packing causes the time for fluid to be drained to scale by d^2, not d^4. The final equation governing scaling is Equation 4.5.

$$t = \frac{1}{R} \frac{512}{\pi} \frac{L\mu}{\Delta P} \frac{1}{d^2} \tag{4.5}$$

When analyzing this (Figure 4.9), the change in time can be seen scale differently and is mostly affected by changes in drain diameter. Having smaller drains is necessary to control smaller particles. Also, as particles become smaller and smaller, Brownian motion will compete against hydrodynamic effects brought about by flow through the drains. However, this would be seen as a net drift in particle position, and the Brownian motion could be beneficial to particle loading.

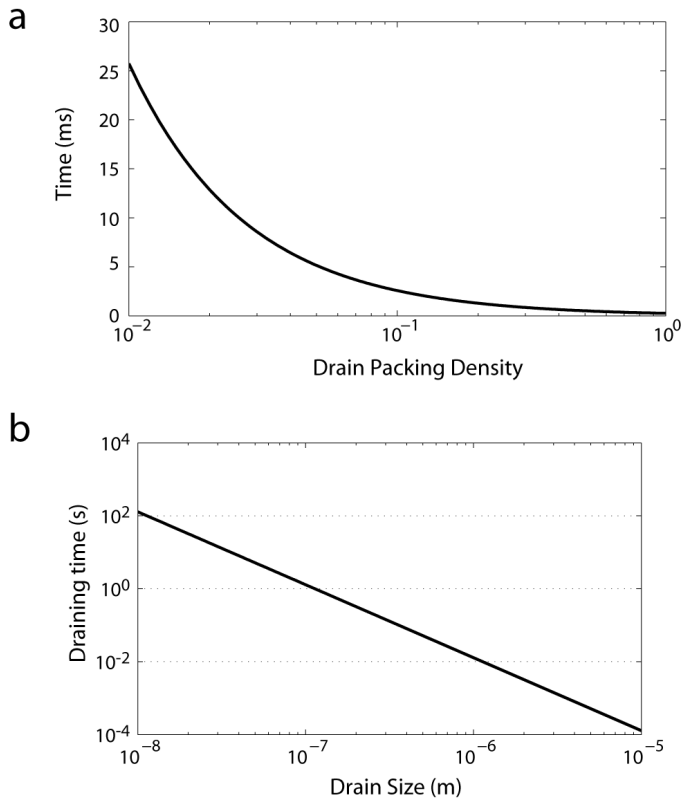

Figure 4.9: Time to drain volume based on Equation 4.5. (a) Time versus drain packing density, R. (b) Time versus drain size, d.

4.4 Conclusion

We have demonstrated that we can change the manipulated frame of reference from an indistinguishable distribution of objects to a discrete, structured and immobilized sampling. Particles were quickly and repeatedly formed into patterns with almost any two-dimensional structure. Compositions of the particles in patterns can be varied using independently controlled drain lines. Also, polymer particles as well as cell lines can be manipulated with this system. The entire array can be designed to accommodate a high drain density to study larger systems or mass-produce a product. However, there remains work to be done in improving and optimizing loading selectivity, and investigation with materials of different density, electric charge and compliance.

In the future these devices can have considerable function in a diverse range of applications from positioning mammalian cells for interaction studies and tissue engineering to anisotropic particle formation and production. With further development, micron and submicron particles should be able to be manipulated in this system for applications such as surface-enhanced plasmon resonance or nanoparticle self-assembly. For smaller particle systems, Brownian motion, higher fluid pressure drops, and particle-particle and particle-surface adhesion forces need to be taken into account. However, the current system should be able to be scaled down at least an order of magnitude without these affects significantly impacting operation.

CHAPTER V

Flows with Tunable Micro- and Nano- Structure at Short Diffusion Timescales

5.1 Introduction

Laminar flow is the characteristic flow in microfluidic channels, with fluids exhibiting stable, predictable and continuous streamlines [41]. In laminar flow, diffusion is the only mechanism for mass transport between streamlines [61]. As a result, mixing between streamlines is controllable and liquids exhibit a flowing structure. Laminar structures, such as co-flowing streams, are used for various chemical and physical processes. For instance, some chemical systems take advantage of the defined interfaces between streams. These have been used to generate particles [111] and fibers [43], to perform sequential chemical reactions such as layer-by-layer deposition [42], and to manipulate light with liquid waveguides and lenses [112, 113]. Other systems rely on known diffusion times, like sub-millisecond diffusive micromixers, which have been generated from micron-sized laminar streams [114] to study protein-folding dynamics [115]. The functionality of these co-flowing systems can benefit from the inherent scalability of microfluidic devices by multiplying stream numbers and miniaturizing stream sizes.

Lithographic processes used to create microfluidic systems and the small dimen-

sions in microfluidic systems provide a platform with which to scale microchemical processes. However, many co-flowing systems do not fully benefit from the scalability [116] in microfluidic systems due to limitations of the size and number of co-flowing streams. For example, the design and construction of a device to encapsulate oil droplets through layer-by-layer deposition limits no more than three co-flowing streams [42]. Additional co-flow has previously required a significant investment to external infrastructure [117]. Significant external infrastructures developed include microfluidic breadboards to regulate flow and a manifold concept. But both of these require external infrastructure and do not integrate into a single systems [118, 119]. This constrains the number of different layers that can be added to the final capsule to a few layers. In another example, rapid micromixers are used to study the high temporal resolution kinetics of biochemical events, such as FRET analysis of structural changes in proteins [120–122]. However, micromixer designs have been limited to a single submicron stream with an inherently small sample volume and therefore poor detection limits. With multiple parallel diffusing submicron streams, the number of mixing interfaces can be dramatically increased and subsequently a target signal can be raised. Methods that generate many co-flowing streams with the ability to actively control stream size and quality can further expand the capabilities of these systems.

We have developed a microfluidic device that scales co-flowing streams, and used it to quantify parameters that control the properties of laminar co-flows. This microfluidic device scales co-flowing streams by utilizing a three-dimensional microfluidic design. The three-dimensional design interdigitates flow from two inlets creating alternating fluid inlets. The flow is constricted along with a third inlet buffer flow to miniaturize the flow pattern over almost two orders of magnitude from the initial size. By producing 64 streams on a single device, co-flows as small as 750 nm were generated with the possibility to create much smaller flows. Design of subsequent systems were analyzed based on fluid, flow and geometric parameters. The quality

of the streams was investigated with both qualitative and quantitative analysis for both, uniformity and sharpness. These properties were shown to controlled by the contact time of the flows and angle of constriction of the flows and are limited by both diffusion and Dean flow.

5.2 Materials and Methods

5.2.1 Microfluidic Device Fabrication

Microfluidic devices were fabricated using standard microfabrication techniques (Figure 5.1). Through holes were patterned by spincoating 8 μm of AZ9260 photoresist on a 100 mm diameter silicon wafer and features were exposed with a Karl Suss MA/BA-6 mask aligner. Deep vertical sidewall trenches were etched with a Surface Technology Systems DRIE to a depth of $\sim$350 μm. The fluidics layer was patterned and etched to a target depth. Spincoating over high aspect ratios was accomplished by pouring UV-curable glue on the features, and the glue was infused in the features with a vacuum. Glue outside of the features was removed with a razor blade. The back channel layers were patterned by spincoating, and by exposing the back of the wafer with backside alignment. After the channels were etched about 100 microns Kapton Vaccum tape was used to mask the channels with the exception of the through holes. The through holes were etched until they reached the front side.

Borofloat glass wafers were electrochemically drilled to create through-hole access to the microfluidic device. Next, glass and silicon was piranha cleaned (3:1 H_2SO_4:H_2O_2) for 30 minutes, rinsed with DI H_2O, sonicated with acetone followed by 2-proponol and activated using a nP-12 nitrogen plasma source. These wafers were placed together and anodic bonded with a -1000V potential at 250°C at $1e-4$ torr. Completed devices were released using a dicing saw and fluidic connections and backside mount was attached using UV-curable adhesive. Fluidic connections

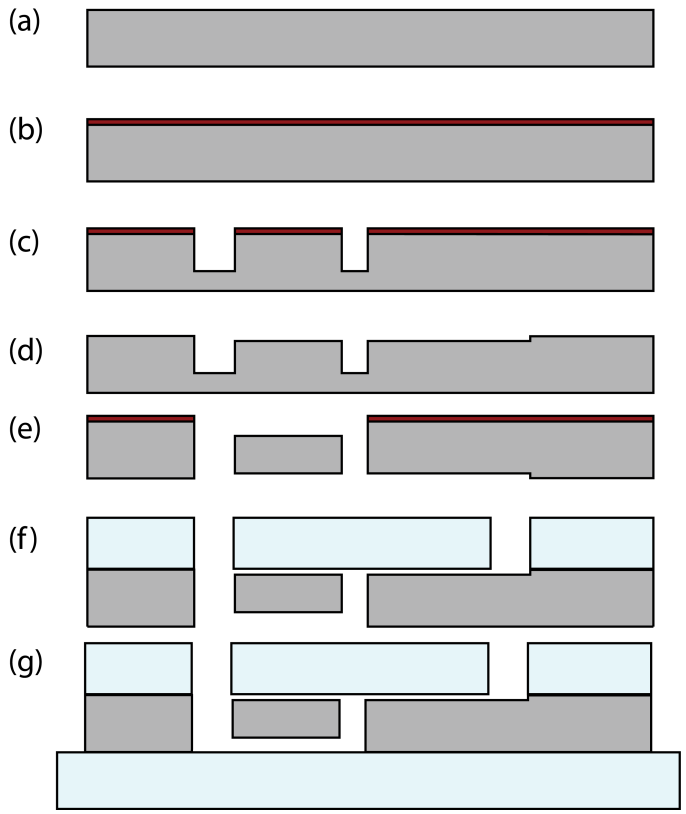

Figure 5.1: Microfabrication diagram. (a) Silicon wafer. (b) Coasted with photoresist. (c) Deep reactive ion etch deep trenches for through holes. (d) Pattern and etch top channel network. (e) Back etching channels and reaching the through holes. (f) Anodic bond glass to top channel network. (g) UV glue back of the device to glass slide.

were attached to the fittings with two part fast-cure epoxy (Norland Optics 61) and precision tips (EFD).

5.2.2 Fluid Delivery

Fluids were delivered using syringe pumps and 30 mL, 10 mL and 5 mL syringes (BD) depending on chosen flow rates. The flow rate was first calibrated using a 15 mL falcon tube and the fluid was injected using constant flow rate settings. Fluids used were denatured ethanol and benzaldehyde. Ethanol was dyed with fluorescein by in a 10:1 proportion of ethanol to ethanol saturated with fluorescein.

5.2.3 Computational Fluid Dynamics

COMSOL v3.4 was used with the 2D momentum transport Incompressible Navier-Stokes module was used to calculate flow streamlines in microfluidic channels. The density and viscosity of ethanol were assumed to be constant ($\rho = 789$ kg/m^3, $\mu =$ .0012 Pa-s). The mesh was refined several times to ensure a high-quality simulation. The direct UMFPACK solver was used to solve the simulation.

5.2.4 Imaging

Imaging was performed using a Zeiss Axioscope with a 20x objective. Images were captures from a cooled CCD camera (MTI) attached to an IFG-300 signal processing system (MTI). Gain and black levels were kept constant between analytical experiments. Fluorescent sources were excited with an HBO 100W mercury arc source and light was filtered with a high-pass fluorescent filter prior to capture. Images were processed in Adobe Photoshop and MATLAB.

5.2.5 Fiber Optic Characterization

Optical transmission across streams was captured with visible light fiber optics (FC-IR100-2, Avantes). An original optical fiber was cleaved in half and exposed fibers were inserted in etched side channels perpendicular to the stream flow. The source and detector fibers were then attached to a UV/Vis spectrophotomer (Avantes). Integration time was adjusted for an appropriate signal.

5.3 Results and Discussion

5.3.1 Three-Dimensional Architecture

We have analyzed and generated a periodic laminar flow structure in a microfluidic system microfabricated in glass and silicon. Two inlets are used to define an

alternating fluid structure by injecting separate fluids through independent bifurcating channels. These channels are on the top and back of the microfluidic device and are brought in contact using alternating through holes (Figure 5.2a). In one design, a total of sixteen streams were generated from eight, 100 μm-wide through holes. Laminar flow stabilizes flow, so the inlet conditions are maintained throughout the fluids path. Flow traveling fast enough appears uninhibited by mixing. This alternating flow pattern can be miniaturized from a constricting geometry to generate a structure with much higher resolution than the initially generated streams (Figure 5.2b). Size reduction is advantageous in the case where through holes were fabricated in silicon, because deep reactive ion etching is sensitive to etched feature size [123]. For example, a 100 μm through-hole etch might be simple from a microfabrication standpoint, but may be prohibitively difficult to etch 3 μm through holes while maintaining device quality.

A third buffer fluid is used to actively control the size of the inlet flows. The buffer gives size control outside of the geometric constraints in the microfabricated system. Buffer flow is introduced after the inlet fluids have been brought in contact and geometrically constricted to prevent backflow.

The flow structure resulting from the microfluidic design can be predicted with computational fluid dynamics software. A structure was predicted by highlighting simulated streamlines from different inlets (Figure 5.2c). As the flows are constricted, the structure transitions from an angled alternating flow to a straight alternating flow. The path of the fluid travels shrinks from 3.3 mm to .4 mm in about a 1 mm distance. The ethanol streams flow in a 70 μm silicon microchannel. By using fluorescein-dyed-ethanol and undyed-ethanol, streamlines are accurately reproduced by highlighting the inherent structure which results from the flows inlet conditions and path. The flow is also stable and, although it is moving quickly (on the order of 1 to 10 cm/s), the structure appears static. Figure 5.9 is a layout of the device dimensions with

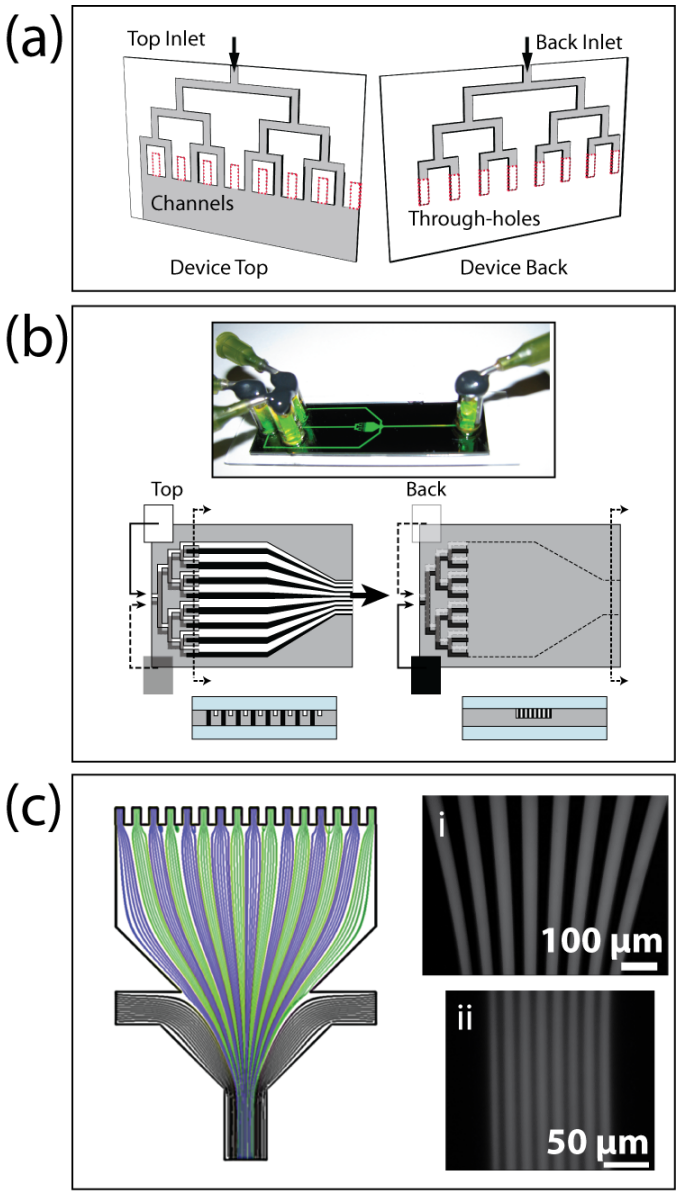

Figure 5.2: Device design for interdigitating fluid streams. (a) Front and back of a silicon wafer with bifurcating channels. Through holes connect and offset channels from the front and back of the wafer. (b) Assembled device, and schematic of flow constricting from the two inlets. (c) Computational fluid dynamics simulations of flow with inlets flow and resulting flows taken at different points in the channel. Scalebar: (i) 100 μm (ii) 50 μm.

appropriate length scales labelled.

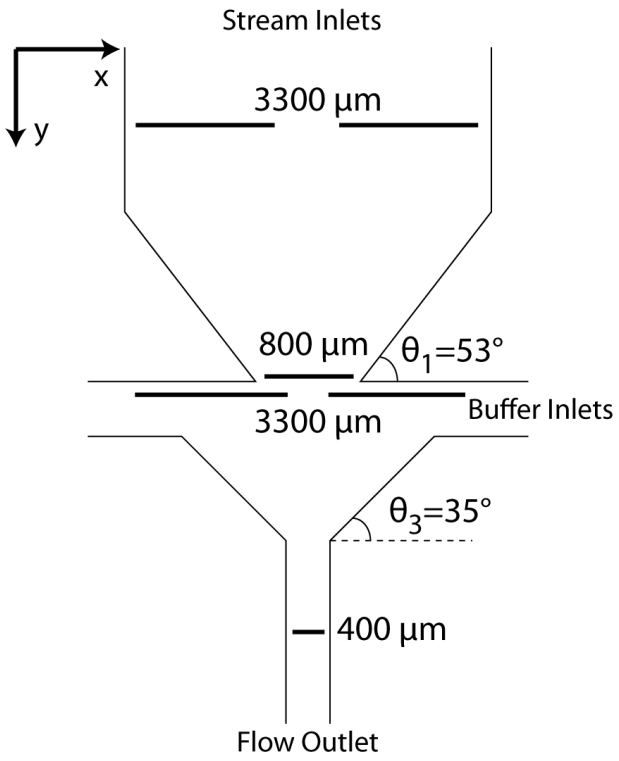

Figure 5.3: Device design with labelled dimensions.

5.3.2 Active Co-Flow Control

By altering buffer flow rates relative to inlet flow rates actively controlled stream size (Figure 5.4a). The parameter R quantifies the ratio of buffer flow rate to inlet flow rate. At high values of R, buffer flow occupies a larger channel ratio and the highlighted structure is reduced. As R is increased, the stream sizes decreases from around 12 μm (at $R = 1$) to 2.5 μm (at $R = 8$, Figure 5.4b). The reduced stream size as a function of R is predicted by a geometric relationship (Equation 5.1), where d_s is stream width, N is the number of streams, and w_c is the constriction width. Further, changes in stream size due to buffer flow control are reflected in the stream geometry within seconds.

$$d_s = \frac{w_c}{N(R+1)} \tag{5.1}$$

In the constructed devices, the upper limit for R that was used is 8, for two reasons.

First, the flow from the buffer is much greater than flow from the inlets, which causes backflow. The syringe pumps used were not able to manage this discrepancy. Future designs can account for this by creating a buffer flow resistance much greater than the inlet flow resistance. Second, although structure may be present, imaging of the stream structure becomes difficult as R is increased because of the high aspect ratio features. Imaging one focal plane causes out of focus fluid structure to blur. When shrinking channel depths, the clarity of small features increased.

5.3.3 Uniformity

In Figure 5.4b, the stream widths have small standard deviations. The flows path conditions, like angle of constriction, are important to control the uniformity of streams. To promote uniformly thick layers, it is optimal for the fluid in the channels to travel roughly equal distances, thereby having equal fluidic resistance and equal flow. However, fluid traveling from inlets that are offset from the constrictions center travel further than fluid inlets that originate at the center. This creates a condition where flow on the outside channels encounters more resistance and therefore flows less. This issue is diagramed in Figure 5.5. As a result, microfabricated constrictions were designed to be steep ($\theta > 30°$), such that the fluid distance travelled from inlet to constriction is long compared to the inlets maximum centerline offset.

Stream uniformity was analyzed by imaging intensity profiles of fluorescent streams and by a fluidic resistance calculation. This analysis is primarily concerned with the distance different packets of fluid must travel from the inlets to the outlet. In this case since the height of the channel, h is much greater than the width of the channel, w, it is assumed the laminar parabolic profile with respect to the x-coordinates is negligible. Also, flows are considered to flow in straight lines as seen in Figure 5.5, and the only source of deviation in path length occurring at the constrictions. Finally, because of symmetry along the y-axis, only half the system will be calculated, with

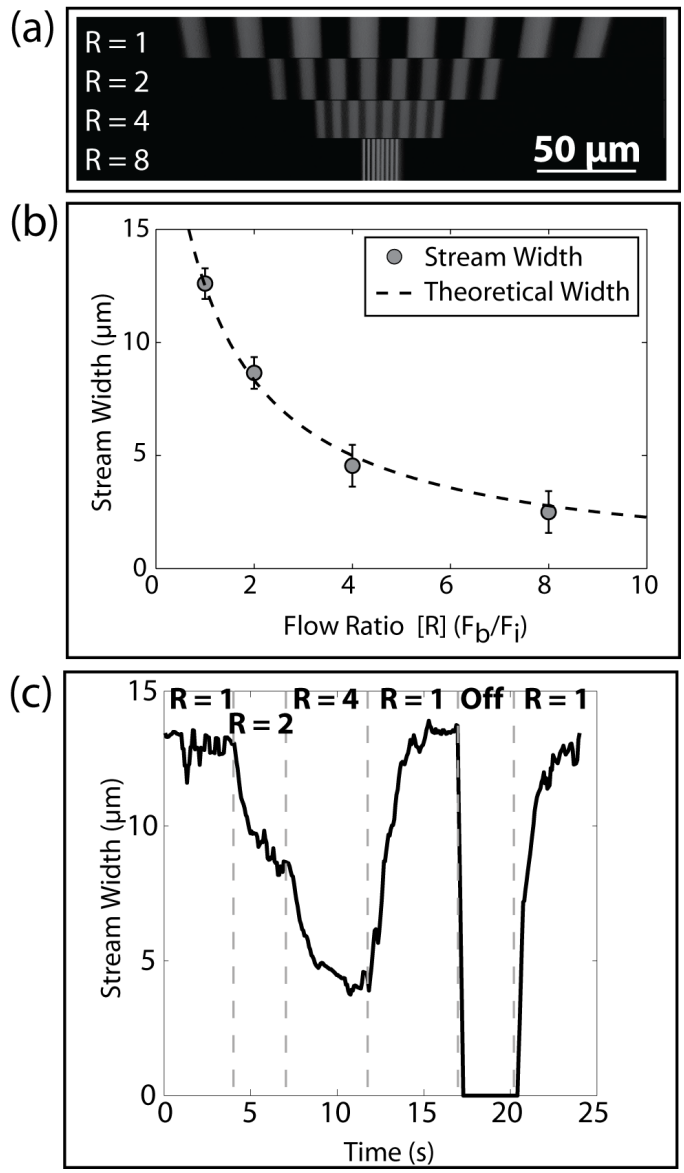

Figure 5.4: Active flow size scalability. (a) Images of streams shrunk at different ratios of buffer flow to inlet flow. Scalebar: 50 μm. (b) Measured stream width at different flow ratios and calculated streams width.

$N = 8$ streams.

With fluidic resistance, fluid flows are treated as in the same ways as electronic flows. Resistance to flow brought on by channel geometry and fluid viscosity are the cause of resistance, a pressure differential (ΔP) is analogous to an applied electric potential, and flow rate, Q, is used instead of current [21]. Similar to Ohm's Law, fluidic resistance (R_{hyd}) is defined by Equation 5.2:

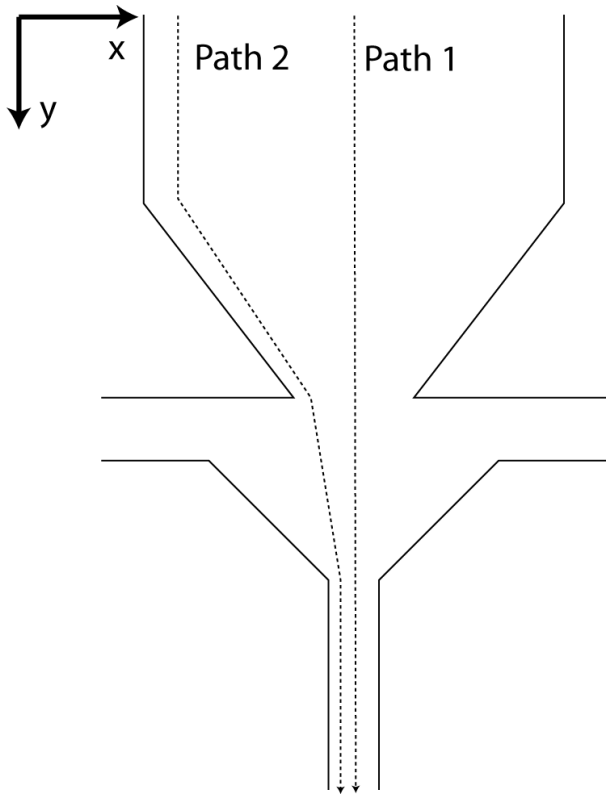

Figure 5.5: Comparison of two possible flow paths by inlet flows.

$$\Delta P = R_{hyd} Q \tag{5.2}$$

Where the resistance is proportional to the travel distance, L. And this travel distance for fluid stream, i, is a function of the x- and y- distance (δx, δy) that the flow will travel (Equation 5.3).

$$L_i = \sqrt{(\delta x_i)^2 + (\delta y_i)^2} \tag{5.3}$$

The δy term is simply a constant that represents the y-distance the fluid has to travel. Depending on the x-position the fluid is in the channel, the δx term changes. The x-position of each stream, x_i, can be known based on the width of every stream, $d_{s,i}$. A width of a stream can be calculated from Equation 5.4. Equation 5.4 is derived from the idea of modeling several resistors in parallel. Flow will proportionally travel

different paths based on resistance [21].

$$d_{s,i} = \frac{w_c}{2}\frac{L_i}{\sum L} \tag{5.4}$$

In this case, w_c is the x-dimension of the channel the streams are located in. The x-position of the center of each stream can be calculated from this information. $x = 0$ is set to be the centerline where the streams converge so the maximum x-value that can be obtained is half the channel width. For instance, for the stream furthest from the centerline (Stream 1), the center of the stream will be half the stream width away from the wall, Equation 5.5.

$$x_1 = w_c - \frac{d_1}{2} \tag{5.5}$$

Subsequent streams will have positions further from the wall based on the width of previous streams as seen in Equation 5.6.

$$x_i = w_c - \frac{d_1}{2} - \sum_{j=1}^{i-1} d_j \tag{5.6}$$

This information can be used to calculate a δx from a channel of size 1, $w_{c,1}$ to a smaller channel of size 2, $w_{c,2}$. This is found by comparing the the value of x_i calculated for $w_{c,1}$, to a ratio comparing the two channel widths, seen in Equation 5.7.

$$\delta x_i = x_i - x_i \times \frac{w_{c,2}}{w_{c,1}} \tag{5.7}$$

By combining the previous equations to solve for L_i what results is Equation 5.8.

$$L_i = f(L_1, L_2, L_3, L_4, L_5, L_6, L_7, L_8) \tag{5.8}$$

This cannot be analytically solved for, so a numerical iterative method was used. A

result was typically converged upon after 5 iterations after an initial guess of uniform stream sizes. From this calculation, streams were predicted to have a parabolic profile, where streams further from the center flowed less, and were not as wide as streams towards the center. A uniformity can be quantified by plotting the ratio of the standard deviation of the stream widths against average stream width, Figure 5.6a. This was compared to the slope of the converging channels with constant channel widths. Steeper channels (higher θ) resulted in more uniform flow and over a 30° slant should result in under 10% deviation. This occurs because as the channels become steeper, the y-distance travelled becomes greater and begins to significantly outweigh differences in flow caused by a centerline offset. Also. it is important to note that streams are more uniform as the R value is increased. This is because as streams encounter more buffer flow, they are miniaturized at a steeper angle than with lower buffer flows.

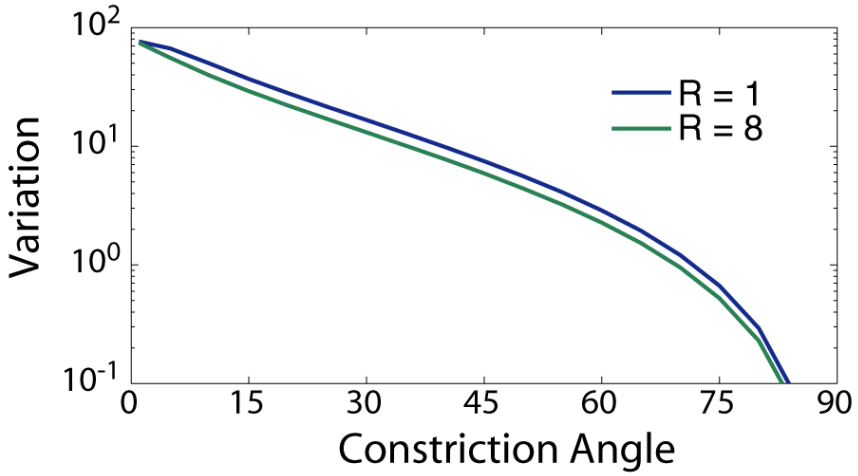

Figure 5.6: Uniformity of stream widths. (a) Calculated stream width uniformity. (b) Experimental stream intensity versus x-position (y-position held constant) after constriction.

Plotting the experimental intensity of streams reflects the theoretical finding that streams in the center will flow higher than streams on the ends (Figure 5.6). This can be seen through the slightly parabolic intensity profile of the streams, where center

streams are more prominent than edge streams. It could be argued that the light source used may not have a uniform intensity exposure, however that cannot account of the fact that at all size scales this parabolic profile is prominent. According to theory, for this system, the intensity of size variation should be on the order of several percent. Therefore, although this possible effect is apparent, it is not overwhelming. Finally, it appears that stream sizes become less uniform as R is increased. This is not in agreement with prediction and could be a result from having more sensitive flows, fabrication inhomogeneities or less accurate imaging.

5.3.4 Miniaturization

A second device was constructed in which the number of streams was increased to 64 streams by adding two bifurcations to the fluid inlet channels. Through holes were also fabricated to be 50 μm wide. In Figure 5.7a, 47 of the streams are imaged as they traveled through the constriction. Interestingly, some streams appear to be brighter than others, and brightness is a function of fluorescein concentration and stream sizes. This could be because of higher flow rates from specific stream inlets. Also, as the number of bifurcations increase, the probability for fabrication inhomogeneities increase, which may be reflected in the streams.

From Equation 5.1, as the number of streams increase from 16 to 64, the effective resolution of the system increases four-fold for constant R values and channel widths. Miniaturizing the streams in the constriction at R = 4 for this system results in calculated fluid streams of $\sim$ 750 nm. These cannot be easily resolved using standard imaging techniques (Figure 5.7b). To circumvent lack of resolution and interrogate streams below available imaging capabilities, streams are expanded after they are constricted to sub-micron sizes (Figure 5.7c). Since the streams clearly exist after expansion, a property of laminar flow is that it is reversible, and can be used to conclude that streams were present in the constriction, and persisted at a width of

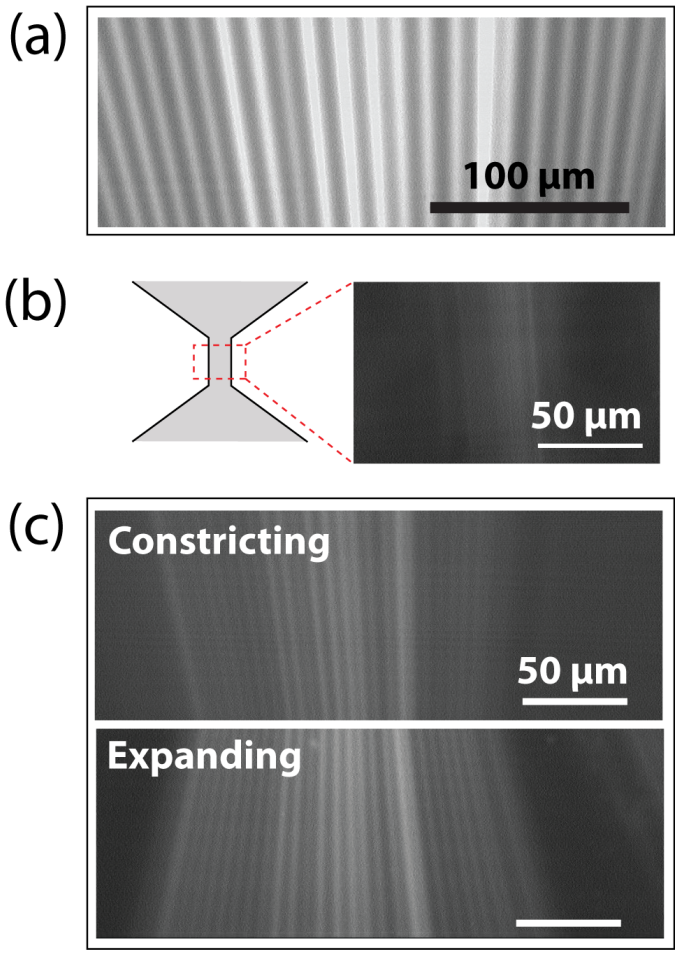

Figure 5.7: Stream number increase and stream miniaturization. (a) Screenshot of a 64 streams device. 47 streams are shown in this image. Scalebar: 100 μm (b) Imaged constriction with flowing streams. Scalebar: 50 μm. (c) Stream showing clear structure before full miniaturization and clear structure on expansion. Scalebar: 50 μm.

750 nm with negligible effects from diffusion. This was created with a total stream inlet flowrate of about 5 mL/hr or around 100 μL/min.

Streams ($N = 16$) were also manipulated in the channel to create non-uniform patterns. By microfabricating a circular obstruction in the flowpath, streamlines were curved and created a pattern similar to the classic Stokes flow around a sphere, Figure 5.8 [124]. Similar to the case of 64 streams, as flow was miniaturized (R = 2), the streams could not be easily resolved and after the expansion, the presence of streams confirmed high resolution structured flow around the circle.

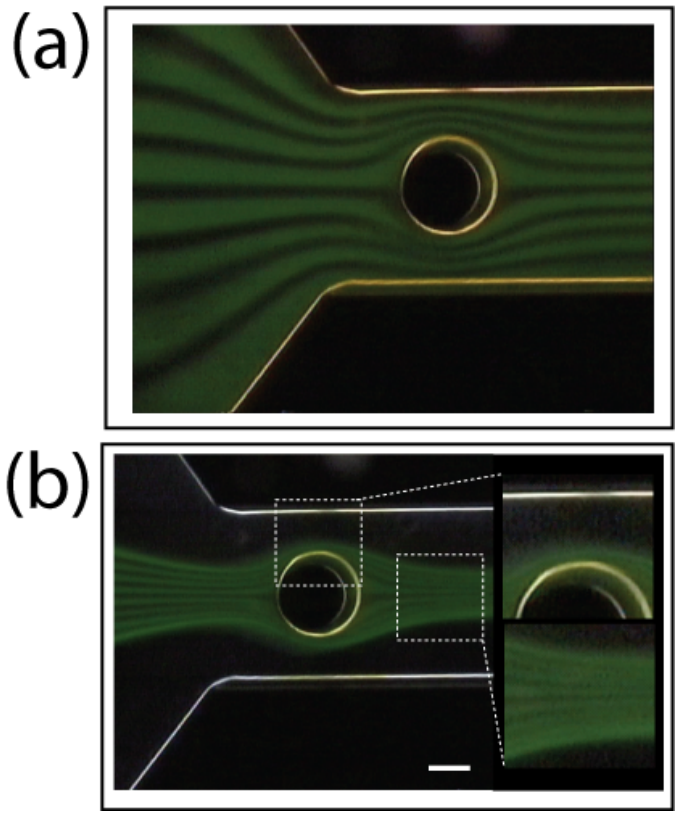

Figure 5.8: Structured flow around a cylinder imaged with a stereoscope and color CCD camera. (a) Flow at R = 0. (b). Flow at R = 2 with magnified sections around the side of the cylinder and after passing the cylinder. Scalebar: 250 μm.

5.3.5 Stream Quality - Diffusion

A model was developed, based on low relative diffusion time, which accurately predicts flow rates required to keep any desired stream quality. The distance molecules diffuse is proportional to $t^{\frac{1}{2}}$, where t is diffusion time, so as stream size decreases diffusion time greatly decreases with it [61]. For instance, a 1 μm stream of ethanol and fluorescein (diffusion coefficient, $D_f = 5 \times 10^{-10}$ m^2/s) [125] has a characteristic diffusion time (63% diffuse) of about 125 μs, while a 10 μm stream will diffuse in about 12.5 ms. By adapting the diffusion times and residence times for our converging flow system, diffusion of the streams can be predicted.

Diffusion of fluorescein between streams was calculated assuming a time-dependent

1D diffusion perpendicular to flow. At relatively short diffusion times, this equation can be linearized to a simple expression Equation 5.9 representing a characteristic diffusion time, t_d.

$$t_d = \frac{d_s(l)^2}{4D_f} \tag{5.9}$$

In this case, d_s is the stream width. Since stream width is dependent on position in the microchannel, and is uniform, d_s is a function of the position in the microchannel, l. Each stream is bounded on each side by another stream, and the characteristic size is actually half a stream width since diffusion occurs on two fronts. Stream size is considered to be uniform. In addition, the stream width is dependent on the whether the channel has no buffer flow (Equation 5.10) which happens at the larger stream sizes earlier in the channel, or if the channel has buffer flow Equation 5.11 further in the channel.

$$d_s(l) = \frac{w(l)}{N} \tag{5.10}$$

$$d_s(l) = \frac{w(l)}{N(R+1)} \tag{5.11}$$

The width of the channel, $w(l)$ will determine stream size. To predict the amount of diffusion that takes place, the diffusion time, t_d, must also be compared to the contact time of the laminar co-flows residence time in the system (Equation 5.15). Residence time, t_r is inversely proportional to flow velocity. Because flow is incompressible and satisfies mass conservation the velocity is a function of the width of the channel, $w(l)$. As flows are narrowed and constricted, the flows speed up. Channel height, h, remains constant.

$$t_r = \frac{V}{Q_v} = \frac{lhw(l)}{Q_v} \tag{5.12}$$

Q_v is the volumetric flowrate at the measured position in the microchannel. The flowrate is also a function of buffer flow addition, where Q_T is the total flow entering the system. Q_v is dependent on whether or not a section is being calculated with or without buffer flow. Without buffer flow is Equation 5.13 and with buffer flow is Equation 5.14.

$$Q_v = \frac{Q_T}{R+1} \tag{5.13}$$

$$Q_v = Q_T \tag{5.14}$$

The ratio of the diffusion time versus the residence time, integrated for the system, can give us a value representing how diffuse the system is. Using our systems specific geometry, we can solve for this ratio resulting in Equation 5.16. The geometry is calculated from 4 sections that must be integrated separately, Equation 5.15.

$$\frac{t_r}{t_d} = \sum_{i=1}^{4} (\frac{t_r}{t_d})_i \tag{5.15}$$

An diagram of the device with labelled regions is displayed in Figure 5.9. The four sections are color-coded differently and the specific widths and lengths are appropriately labelled. The first and last sections are straight channels with constant widths and the second and third sections are slanted channels that geometrically constrain the flow and have variable width. Also, the third and fourth sections differ from the first two because they include buffer flow.

$$\frac{t_r}{t_d} = \frac{4D_f N^2 h}{Q_T}(R+1)(\frac{l_1}{w_1} + \int_{l_1}^{l_2} \frac{\delta l}{w_2(l)} + (R+1)\int_{l_2}^{l_3} \frac{\delta l}{w_3(l)} + (R+1)\frac{l_4}{w_4}) \tag{5.16}$$

The two quantities of $w_2(l)$ and $w_3(l)$ are linear equations. They are listed as,

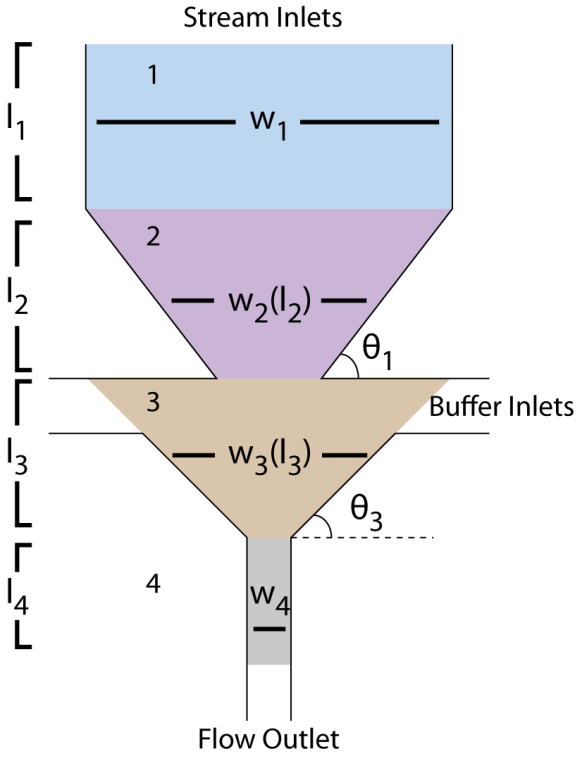

Figure 5.9: Sectioned and labelled device, separated into 4 quarters for separate integration to find predicted diffusion.

Equation 5.17 and 5.18.

$$w_2(l) = \frac{w_2(l_1 + l_2) - w_2(l_2)}{l_2} l + w_2(l_1) \tag{5.17}$$

$$w_3(l) = \frac{w_3(l_2 + l_3) - w_3(l_3)}{l_3} l + w_3(l_2) \tag{5.18}$$

This dimensionless time fraction is then used as an exponential decay to estimate a percent diffusion, D_p from Equation 5.19.

$$D_p = 100 \times (1 - exp^{-\frac{t_r}{t_d}}) \tag{5.19}$$

The dimensionless inverse Pèclet number arises and relates convection to diffusion (Equation 5.20). Minimizing this number is important to achieving the sharpest

features possible because convection will be much greater than diffusion. Although diffusion time scales by the diffusion distance squared, co- flows diffusion scales linearly. This is because as features become smaller through a geometric constriction, flow velocity increases. The contact time for these streams linearly decreases while the diffusion time quadraticly increases.

$$\frac{1}{Pe} = \frac{4D_f N^2 h}{Q_T} \tag{5.20}$$

Theory and experimental results were compared by imaging a uniform stream size (R value) and changing the flow rates. As flow rates decreased, the contact and diffusion time increases, which is observed by the stream interfaces blurring (Figure 5.10a). Diffusion percent was measured as the average maximum intensity of the fluorescent streams versus the minimum intensity in the non-fluorescent streams. We see that this developed theory compares closely to the data (Figure 5.10b). For this system, the $1/Pe = 5.12 \times 10^{-11}$ with $D_f = 5 \times 10^{-10}$ m^2/s, $h = 100$ μm and $N = 16$ streams. The shape factors were calculated based on an w_1 and l_1 of 3300 μm and 1933 μm respectively. w_4 and l_4 (distance past constriction where measurements were taken) of 400 μm and 300 μm respectively. The two constrictions used were the widths of two lineally constricting segments. The width, $w_2(l)$, was calculated from a width shrinking from 3300 μm to 800 μm over a distance of 1700 μm. The width, $w_3(l)$, was calculated from a width shrinking from 3300μm to 400μm over a distance of 1025 μm.

The value of the geometric parameters from Equation 5.16 were analyzed more in depth versus channel constriction angle. This resulted in essentially changing l_2 and l_3 of the geometric parameter. It is expected that a steeper system results in longer residence times and therefore the geometry's contribution to diffusion will greater. Plotted in Figure 5.11 is the effect of geometry versus constriction angles. Four lines plotted represent the diffusion effect from the four sections of the device (Figure 5.9).

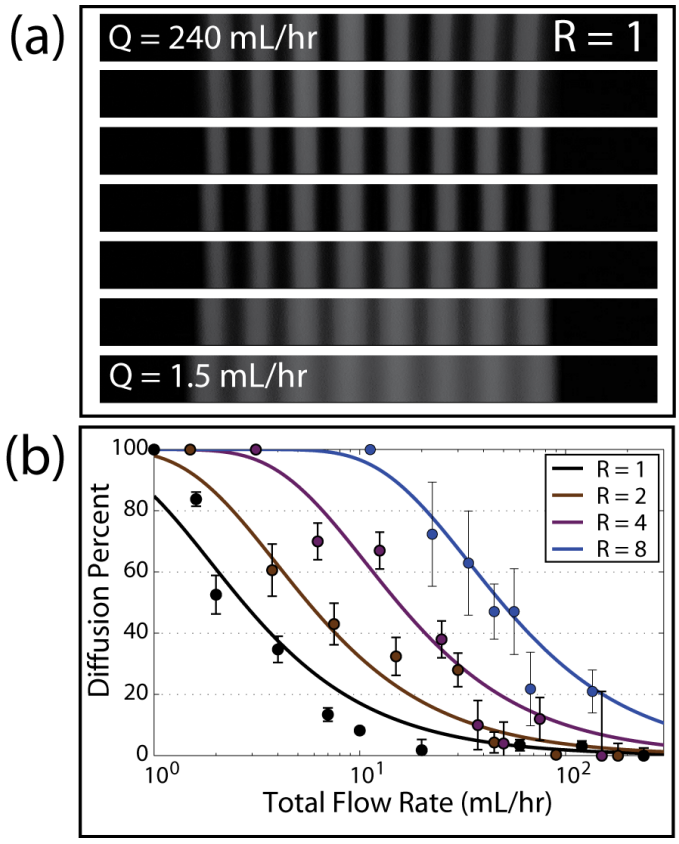

Figure 5.10: Stream quality from diffusion. (a) Images of constant sized streams blurring with decreasing flow rates and increased residence time. (b) Calculated and measured diffusion percentages for streams of varying size versus flow rate.

The straight channel sections have uniform contributions based on angle, and both stay under 1. Sections 2 and 3, as expected, have increasing diffusion contributions as angle increases. Around 60 degrees, the diffusion contribution of the constrictions begins to rapidly increase past two. It is also important to note that sections 3 and 4 are scaled by $(R+1)^2$, so this increase will be more prominent. Therefore, these results suggest that angles must be low enough to account for diffusion. However, at higher Pe numbers, this shape effect may still be insignificant.

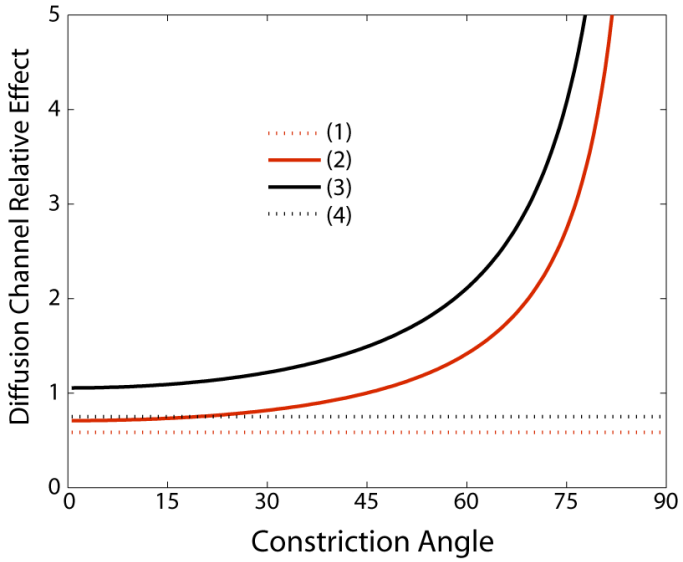

Figure 5.11: The relative effect of channel geometry on diffusion with a changing constriction angle.

5.3.6 Stream Quality - Dean Flow

Miniaturizing streams can also give rise to Dean flow, a rolling flow perpendicular to axial flow [126]. By flowing two different miscible fluids (ethanol and benzaldeyde) Dean flow was observed (Figure 5.12a). Dean flow is caused by velocity gradients related to centripetal acceleration and is amplified by fluids with unequal densities. Although no curvature was explicitly designed in our system, the act of converging flow in this micronozzle creates very slight curves, which are prominent at low R-values (Figure 5.12b). At some flowrates necessary to create distinct microstructure, like 120 mL/hr, curves with high radius of curvature begin to slightly roll, exhibiting a three-dimensional structure upon imaging. Depending on the application, this structure can be desired. In fact, it has been used before to create a curved fluidic microlens [127]. Regardless, to obtain a straight smooth structure, an upper flow limit, characterized by the Dean number is present (Equation 5.21). In the Dean number, R_c is the radius of curvature in the flow, $_d$ is the characteristic dimension of the flow (in this case the channel height) and other parameters are the velocity,

U, density, ρ, and viscosity, μ. Dean flow was reduced by actively lowering the Reynolds number. This was demonstrated by slowing down flow rate and seeing this phenomena diminish (Figure 5.12c). However, lowering flow rate to mitigate Dean flow will increase diffusion between streams. Another way to mitigate Dean flow is to increase the constriction distance and constriction angle. This will cause flow to have a larger radius of curvature on constriction. However, again, this will promote more diffusion, but may also promote uniformity.

$$De = \frac{\rho U d}{\mu}\sqrt{\frac{d}{2R_c}} \tag{5.21}$$

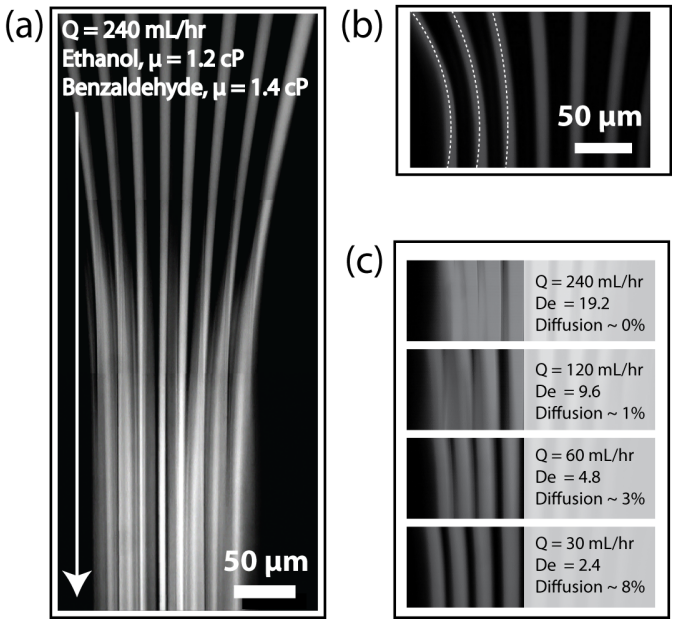

Figure 5.12: Dean flow. (a) Images stitched together from three frames of ethanol and benzaldehyde flowing through a constriction at 240 mL/hr, with R = 2 in a 70 μm high device. Ethanol is highlighted with fluorescein. Scalebar: 50 μm (b) Curvature of the streams at R = 1. Scalebar: 50 μm (c) Decreasing flowrate with a constant R value changing the clarity of the streams as diffusion increases.

5.4 Conclusions

A three-dimensional microfluidic method has been developed to scale and co-flowing microfluidic streams both in number and size, and the physical phenomena controlling streams quality in scaled co-flows has been investigated. An idea for upper and lower bounds have been proposed and can be considered when designing systems that converge laminar coflows. Further investigation should be done to connect theoretical derivations for stream uniformity and diffusion versus constriction angle more closely to experiment so definitive parameters are known. Also, in-depth investigation of Dean flow with respect to viscosity and density of several streams could be an interesting and worthwhile endeavor, especially for developing micromixers or high-flow systems [126].

This method, creating miniaturized co-flows, can expand current capabilities in microfluidic systems to use co-flows for applications from optics to material generation. For instance, we demonstrated the ability to make submicron streams with controlled diffusion, set curvature from Dean flow. These could be used to assist in production of proposed metamaterials that require geometric curvature and gradient index of refraction, like extreme-angle broadband lenses [128, 129]. Also, coflows can be combined with current co-flow material polymerization techniques to produced new complex materials with curvatures based on complex flow patterns. These systems, with integrated fiber optics, can be used to probe microsecond chemical processes with high fidelity. The scalability of streams can possibly be capitalized on as an alternative to using nano-channels. Demonstrated submicron streams, can be used to probe oligomers while avoiding large pressure drops that can occur in these channels.

CHAPTER VI

Conclusions and Continuing Work

6.1 Conclusions

The goal of this dissertation was to enhance microchemical handling in microfluidic systems and to exploit properties in microfluidic systems to create structured materials. To enhance chemical handling, a method to interface continuous flows to nanoliter droplets was developed and polyacrylamide gel electrophoresis in microchannels was studied. Structured materials were generated in microfluidics using convective flows to position particles and cells on a two dimensional array of holes and co-flowing laminar streams were arrayed to create a flow sub-micron alternating fluid structure.

To actively control the contents of nanoliter droplets, a device was designed and characterized to remove and deliver reagents from nanoliter droplets. This was accomplished using a convective flow which diffuses through a semi-permeable membrane into and out of droplets. This membrane was found to be permeable to water, organic solvent, salts and fluorescent dyes and, as a result, subsequent reactions and separations were performed on-chip. Methods to control nanoliter droplet contents were traditionally predetermined by a specific inlets and geometry with little latitude for broad designs. Also, these methods were primarily used to introduce high volumes of reagents by merging droplets. With this membrane methodology, a simple

1-step fabrication was developed that can continuously address droplet contents and is flexible towards desired functions.

Polyacrylamide gel electrophoresis of dsDNA was analyzed in glass microfluidic channels using confocal laser scanning microscopy. A net motion of the DNA to the top and bottom edges of the polyacrylamide gel was observed. This effect was seen to be a reversible process that was a function of the type of gel used to separate the dsDNA as well as the length and ridgity of the dsDNA molecules. This is the first reported instance of the phenomena and it was speculated that a gel pore size inhomogeneity can be attributed to the preferential migration of the dsDNA to the pore edges. Non-uniform DNA migration can deteriorate resolution of electrophoretic separations and hinder microscale separation performances. With this information, methods to form gels in microfluidic channels can be more carefully crafted with the aim of creating higher resolution electrophoresis separations.

Complex two-dimensional particle patterns were formed using a non-planer microfluidic system. By fabricating through-holes on a silicon substrate, convective flow driven by a pressure differential was used to position particles directly onto through-holes. Since microfabrication controls through-hole placement, the resolution and size of particle patterns was only limited by microfabrication resolution. Previously, particle and cell placement resolution has been either one-dimensional and limited to single particles, or circumstantially two-dimensional. With this method, there is now a rapid and direct technique to position particles and cells which can be used to culture cells from an initial starting position, create complex particle patterns for building up larger particles or to array particles with two dimensional precision.

By connecting two bifurcating channel networks with through-holes, alternating co-flows were produced. The design of this microfluidic system inherently allowed for the number and size of the subsequent co-flows to be easily scaled and controlled. This was demonstrated by generating 64 co-flowing fluid streams and submicron size scales.

Also, parameters governing the performance and quality of coflows was investigated. Previously the number of streams, and consequently the size of the streams, was limited by the external architecture of the microfluidic system. This technology will enable current work using co-flowing streams to be greatly scaled and subsequently expand on the functionality of these coflows. Specific applications include enhancing microfluidic materials generation, creating unique optofluidic flows and expanding capabilities of rapid micromixers.

6.2 Continuing Work

6.2.1 Particle Filter to Visually Detect DNA Hybridization

The particle microarraying technology presents an platform with which to array functionalized particles to undergo a biochemical reaction such as the ligase detection reaction (LDR) [130]. LDR can be used to detect single nucleotide polymorphisms (SNP). By creating varying sized particles with different DNA primers, SNPs can be rapidly screened. Since the through-holes are fabricated based on a certain size, these can be used as a particle sieve, separating and sequestering particles based on size. This two-dimensional particle array can be used to position relatively few particles over a large area. By functionalizing particles based on size along with use of quantum dots, different size-selective regions can be visually inspected for a positive reaction. This setup, diagrammed in Figure 6.1, has several engineering challenges associated with it.

First, figuring out how to position particles on drains while allowing smaller particles to pass through is not trivial. As previously seen with *S.Ludwigii* cells which are smaller than the drain size, they can clog drains and not pass through. When dealing with particles that should pass and should not pass, a creative flow scheme should be devised either by using alternating pulsing flows or by figuring out a critical density

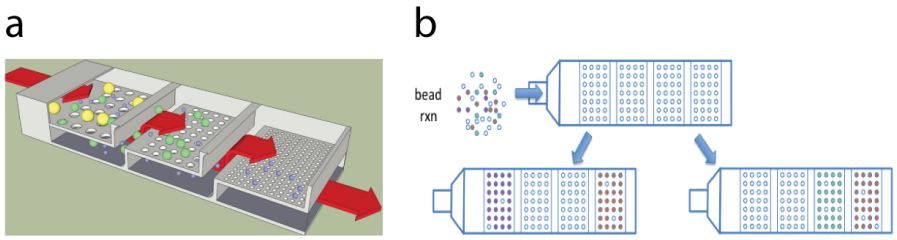

Figure 6.1: Bead-based array to separate and place particles based on sizes. (a) Design of particles flowing from large holes to small holes. (b) Visual readout of the system.

with which to operate this system. This will also require analysis of a separation efficiency that is deemed acceptable for the purposed of this system. Also, laminar flow occurring in a microfluidic system is reversible. So alternating flow may not be entirely effective and may require a more thoughtful solution to selectively array particles. From a reactions perspective, achieving appropriate chemical flows to all of the particles may prove to be a difficult task.

6.2.2 Continuous Separation and Infrared Detection of Nanoliter Samples

Using the inherent preferential separation of organic solvent through a PDMS membrane coupled with an integrated infrared fiber, volatile organics can be identified and quantified. This method is diagrammed and prototype devices are shown in Figure 6.2. With this method, nanoliter droplets will move next to a chamber where a steep concentration gradient exists and is held constant because of a nitrogen flow. An open chamber is located between the nitrogen flow and droplet channel, and the flux of molecules from the droplet to the nitrogen channel should be measured by the FTIR signal.

Problems will arise mainly from the sensitivity of this system. Since the measurement chamber's volume is on the order of nL and the maximum signal can be very low. Also, a question that must be addressed is how low of a concentration of organ-

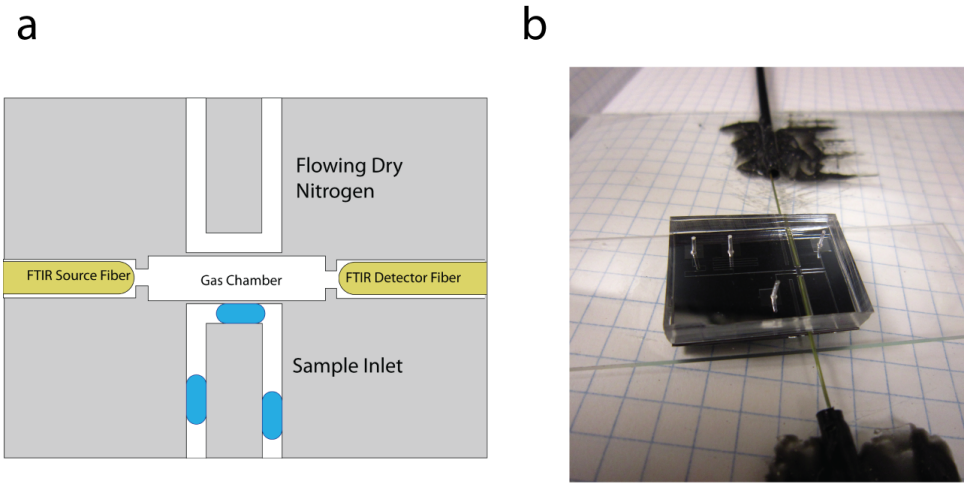

Figure 6.2: Nanoliter sample interrogation using an infrared fiber optic integrated to a microfluidic device. (a) Concepts of the device, where droplets will flow and permeate through a thin wall and contents will travel into a nitrogen channel. Between the droplet and nitrogen channel is a detection chamber which is bounded by source and detector fibers. (b) Image of the microfabricated device with fiber optics.

ics can be measured from FTIR chamber. This may be a function dependent on the signal integration time, flow rate of droplets, intensity of the concentration gradient, chemical's being interrogated and concentration of a target chemical species in the droplet phase.

6.2.3 Integrated UV/vis Fiber Optic to Stream Flows

The fluid co-flow setup has been shown to be able to make curved structures with sub-micron resolution and diffuse features. Some of these properties are unique to current materials and have the potential to create structures that are unique and unable to generate by simple solid processing alone. The properties of combining a gradient index of refraction with geometric curvature has been theoretically shown to open possibilities to make unique light-guiding materials [129]. The optical properties of these fluids can be interrograted by integrating a UV/vis fiber across the path of the fluid. Measuring a simple Bragg Interference filter would be a target first goal

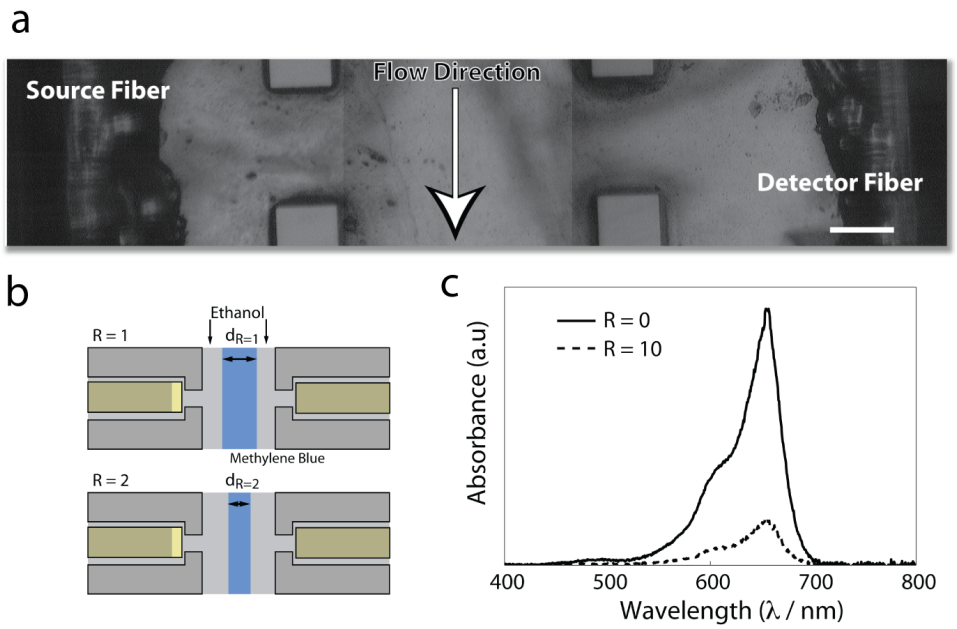

Figure 6.3: Integrated UV/vis fiber optic. (a) Image of microfabricated device with cleaved source and detector fiber placed across the path length. (b) Diagram of a sample experiment where methylene blue stream is measured based and signal is changed based on the stream width. (c) Transmission results of varying width methylene blue streams which can be predicted from the Beer-Lambert absorption law.

with this system. Further steps can include polymerizing the fluid structure in situ. However, the features must be uniform to achieve a strong optical effect. Achieving small, uniform features that are not diffuse could be a design optimization challenge.

BIBLIOGRAPHY

BIBLIOGRAPHY

[1] G.M. Whitesides. The origins and the future of microfluidics. *Nature*, 442(7101):368–373, 2006.

[2] W.C. Tian and E. Finehout. Introduction to microfluidics. *Microfluidics for Biological Applications*, pages 1–34, 2009.

[3] J.C. Venter, M.D. Adams, E.W. Myers, P.W. Li, R.J. Mural, G.G. Sutton, H.O. Smith, M. Yandell, C.A. Evans, R.A. Holt, et al. The sequence of the human genome. *science*, 291(5507):1304, 2001.

[4] E.S. Lander, L.M. Linton, B. Birren, C. Nusbaum, M.C. Zody, J. Baldwin, K. Devon, K. Dewar, M. Doyle, W. FitzHugh, et al. Initial sequencing and analysis of the human genome. *Nature*, 409(6822):860–921, 2001.

[5] F.E. Regnier, B. He, S. Lin, and J. Busse. Chromatography and electrophoresis on chips: critical elements of future integrated, microfluidic analytical systems for life science. *Trends in biotechnology*, 17(3):101–106, 1999.

[6] SC Truxal, Y.C. Tung, and K. Kurabayashi. A pdms-on-silicon deformable grating for spectral differentiation of mixed wavelength signals. In *Solid-State Sensors, Actuators and Microsystems Conference, 2007. TRANSDUCERS 2007. International*, pages 1087–1090. IEEE, 2007.

[7] M.J. Madou. *Fundamentals of microfabrication: the science of miniaturization*. CRC, 2002.

[8] G.M. Whitesides, E. Ostuni, S. Takayama, X. Jiang, and D.E. Ingber. Soft lithography in biology and biochemistry. *Annual Review of Biomedical Engineering*, 3(1):335–373, 2001.

[9] M.A. Unger, H.P. Chou, T. Thorsen, A. Scherer, and S.R. Quake. Monolithic microfabricated valves and pumps by multilayer soft lithography. *Science*, 288(5463):113, 2000.

[10] M.A. Burns. Everyone's a (future) chemist. *Science*, 296(5574):1818, 2002.

[11] M.A. Burns, B.N. Johnson, S.N. Brahmasandra, K. Handique, J.R. Webster, M. Krishnan, T.S. Sammarco, P.M. Man, D. Jones, D. Heldsinger, et al. An integrated nanoliter dna analysis device. *Science*, 282(5388):484, 1998.

[12] M. Yang, R. Lin, BN Johnson, N. Srivastava, SZ Razzacki, KJ Chomistek, DC Heldsinger, RM Haque, VM Ugaz, PK Thwar, et al. An integrated microfluidic device for influenza and other genetic analyses. *Lab on a Chip*, 5(10):1024–1032, 2005.

[13] C. Zhang and D. Xing. Miniaturized pcr chips for nucleic acid amplification and analysis: latest advances and future trends. *Nucleic acids research*, 35(13):4223, 2007.

[14] N. Srivastava and M.A. Burns. Analysis of non-newtonian liquids using a microfluidic capillary viscometer. *Analytical chemistry*, 78(5):1690–1696, 2006.

[15] J. Homola. Present and future of surface plasmon resonance biosensors. *Analytical and bioanalytical chemistry*, 377(3):528–539, 2003.

[16] A. Bange, H.B. Halsall, and W.R. Heineman. Microfluidic immunosensor systems. *Biosensors and Bioelectronics*, 20(12):2488–2503, 2005.

[17] P.S. Dittrich, K. Tachikawa, and A. Manz. Micro total analysis systems. latest advancements and trends. *Analytical Chemistry*, 78(12):3887–3908, 2006.

[18] D.J. Beebe, G.A. Mensing, and G.M. Walker. Physics and applications of microfluidics in biology. *Annual review of biomedical engineering*, 4(1):261–286, 2002.

[19] H.A. Stone, A.D. Stroock, and A. Ajdari. Engineering flows in small devices. *Annu. Rev. Fluid Mech.*, 36:381–411, 2004.

[20] M.A. Burns. Microfluidic chemical analysis. *Annual Review of Chemical and Biomolecular Engineering*, 2(1), 2011.

[21] H. Bruus. *Theoretical microfluidics*, volume 18. Oxford University Press, USA, 2008.

[22] A.E. Herr, A.V. Hatch, D.J. Throckmorton, H.M. Tran, J.S. Brennan, W.V. Giannobile, and A.K. Singh. Microfluidic immunoassays as rapid saliva-based clinical diagnostics. *Proceedings of the National Academy of Sciences*, 104(13):5268, 2007.

[23] B.H. Weigl and P. Yager. Microfluidic diffusion-based separation and detection. *Science*, 283(5400):346, 1999.

[24] S. Takayama, J.C. McDonald, E. Ostuni, M.N. Liang, P.J.A. Kenis, R.F. Ismagilov, and G.M. Whitesides. Patterning cells and their environments using multiple laminar fluid flows in capillary networks. *Proceedings of the National Academy of Sciences*, 96(10):5545, 1999.

[25] A.D. Stroock, S.K.W. Dertinger, A. Ajdari, I. Mezić, H.A. Stone, and G.M. Whitesides. Chaotic mixer for microchannels. *Science*, 295(5555):647, 2002.

[26] B. Kuswandi et al. Optical sensing systems for microfluidic devices: a review. *Analytica chimica acta*, 601(2):141–155, 2007.

[27] ET Lagally, I. Medintz, and RA Mathies. Single-molecule dna amplification and analysis in an integrated microfluidic device. *Analytical chemistry*, 73(3):565–570, 2001.

[28] F. Wang and M.A. Burns. Performance of nanoliter-sized droplet-based microfluidic PCR. *Biomedical microdevices*, 11(5):1071–1080, 2009.

[29] R. Mukhopadhyay. When microfluidic devices go bad. *Analytical chemistry*, 77(21):429–432, 2005.

[30] N.T. Nguyen and Z. Wu. Micromixers—a review. *Journal of Micromechanics and Microengineering*, 15:R1, 2005.

[31] A.R. Abate, T. Hung, P. Mary, J.J. Agresti, and D.A. Weitz. High-throughput injection with microfluidics using picoinjectors. *Proceedings of the National Academy of Sciences*, 107(45):19163, 2010.

[32] S.Y. Teh, R. Lin, L.H. Hung, and A.P. Lee. Droplet microfluidics. *Lab on a Chip*, 8(2):198–220, 2008.

[33] A.B. Theberge, F. Courtois, Y. Schaerli, M. Fischlechner, C. Abell, F. Hollfelder, and W.T.S. Huck. Microdroplets in Microfluidics: An Evolving Platform for Discoveries in Chemistry and Biology. *Angewandte Chemie International Edition*, 49:5486, 2010.

[34] J. Nie and R.T. Kennedy. Sampling from nanoliter plugs via asymmetrical splitting of segmented flow. *Analytical chemistry*, 2010.

[35] G.T. Roman, M. Wang, K.N. Shultz, C. Jennings, and R.T. Kennedy. Sampling and electrophoretic analysis of segmented flow streams using virtual walls in a microfluidic device. *Analytical chemistry*, 80(21):8231–8238, 2008.

[36] J.P. Landers. *Handbook of capillary electrophoresis*. CRC Pr I Llc, 1997.

[37] Z. Chen. *Improving electrophoretic resolution in microfabricated bioanalysis devices*. PhD thesis, UNIVERSITY OF MICHIGAN, 2007.

[38] D. DiCarlo, L.Y. Wu, and L.P. Lee. Dynamic single cell culture array. *Lab on a Chip*, 6(11):1445–1449, 2006.

[39] A.M. Skelley, O. Kirak, H. Suh, R. Jaenisch, and J. Voldman. Microfluidic control of cell pairing and fusion. *Nature methods*, 6(2):147–152, 2009.

[40] W.H. Tan and S. Takeuchi. A trap-and-release integrated microfluidic system for dynamic microarray applications. *Proceedings of the National Academy of Sciences*, 104(4):1146, 2007.

[41] K. Loutherback, J. Puchalla, R.H. Austin, and J.C. Sturm. Deterministic microfluidic ratchet. *Physical review letters*, 102(4):45301, 2009.

[42] C. Kantak, S. Beyer, L. Yobas, T. Bansal, and D. Trau. A 'microfluidic pinball'for on-chip generation of layer-by-layer polyelectrolyte microcapsules. *Lab Chip*, 2011.

[43] W. Jeong, J. Kim, S. Kim, S. Lee, G. Mensing, and D.J. Beebe. Hydrodynamic microfabrication via"[rising dbl quote] on the fly" photopolymerization of microscale fibers and tubes. *Lab on a Chip*, 4(6):576–580, 2004.

[44] C. Monat, P. Domachuk, and BJ Eggleton. Integrated optofluidics: A new river of light. *Nature Photonics*, 1(2):106–114, 2007.

[45] A. Huebner, S. Sharma, M. Srisa-Art, F. Hollfelder, J.B. Edel, and A.J. demello. Microdroplets: A sea of applications? *Lab on a Chip*, 8(8):1244–1254, 2008.

[46] J.J. Agresti, E. Antipov, A.R. Abate, K. Ahn, A.C. Rowat, J.C. Baret, M. Marquez, A.M. Klibanov, A.D. Griffiths, and D.A. Weitz. Ultrahigh-throughput screening in drop-based microfluidics for directed evolution. *Proceedings of the National Academy of Sciences*, 107(9):4004, 2010.

[47] E. Brouzes, M. Medkova, N. Savenelli, D. Marran, M. Twardowski, J.B. Hutchison, J.M. Rothberg, D.R. Link, N. Perrimon, and M.L. Samuels. Droplet microfluidic technology for single-cell high-throughput screening. *Proceedings of the National Academy of Sciences*, 106(34):14195, 2009.

[48] H. Song, D.L. Chen, and R.F. Ismagilov. Reactions in droplets in microfluidic channels. *Angewandte chemie international edition*, 45(44):7336–7356, 2006.

[49] H. Song and R.F. Ismagilov. Millisecond kinetics on a microfluidic chip using nanoliters of reagents. *J. Am. Chem. Soc*, 125(47):14613–14619, 2003.

[50] D. Belder. Towards an Integrated Chemical Circuit. *Angewandte Chemie International Edition*, 48(21):3736–3737, 2009.

[51] L.H. Hung, K.M. Choi, W.Y. Tseng, Y.C. Tan, K.J. Shea, and A.P. Lee. Alternating droplet generation and controlled dynamic droplet fusion in microfluidic device for CdS nanoparticle synthesis. *Lab on a Chip*, 6(2):174–178, 2006.

[52] L.H. Hung, S.Y. Teh, J. Jester, and A.P. Lee. PLGA micro/nanosphere synthesis by droplet microfluidic solvent evaporation and extraction approaches. *Lab on a Chip*, 10(14):1820–1825, 2010.

[53] L. Frenz, A. El Harrak, M. Pauly, S. Bégin-Colin, A.D. Griffiths, and J.C. Baret. Droplet-Based Microreactors for the Synthesis of Magnetic Iron Oxide Nanoparticles. *Angewandte Chemie International Edition*, 47(36):6817–6820, 2008.

[54] B. Zheng, L.S. Roach, and R.F. Ismagilov. Screening of protein crystallization conditions on a microfluidic chip using nanoliter-size droplets. *J. Am. Chem. Soc*, 125(37):11170–11171, 2003.

[55] J. Shim, G. Cristobal, D.R. Link, T. Thorsen, Y. Jia, K. Piattelli, and S. Fraden. Control and measurement of the phase behavior of aqueous solutions using microfluidics. *J. Am. Chem. Soc*, 129(28):8825–8835, 2007.

[56] J. Shim, S.N. Patil, J.T. Hodgkinson, S.D. Bowden, D.R. Spring, M. Welch, W.T.S. Huck, F. Hollfelder, and C. Abell. Controlling the contents of microdroplets by exploiting the permeability of pdms. *Lab Chip*, 2011.

[57] D.C. Duffy, J.C. McDonald, O.J.A. Schueller, and G.M. Whitesides. Rapid prototyping of microfluidic systems in poly (dimethylsiloxane). *Anal. Chem*, 70(23):4974–4984, 1998.

[58] T. Thorsen, R.W. Roberts, F.H. Arnold, and S.R. Quake. Dynamic pattern formation in a vesicle-generating microfluidic device. *Physical Review Letters*, 86(18):4163–4166, 2001.

[59] G.C. Randall and P.S. Doyle. Permeation-driven flow in poly (dimethylsiloxane) microfluidic devices. *Proceedings of the National Academy of Sciences of the United States of America*, 102(31):10813, 2005.

[60] J.N. Lee, C. Park, and G.M. Whitesides. Solvent compatibility of poly (dimethylsiloxane)-based microfluidic devices. *Anal. Chem*, 75(23):6544–6554, 2003.

[61] W.M. Deen. *Analysis of transport phenomena*. Oxford University Press New York, 1998.

[62] JM Watson and MG Baron. The behaviour of water in poly (dimethylsiloxane). *Journal of membrane science*, 110(1):47–57, 1996.

[63] O.D. Velev, A.M. Lenhoff, and E.W. Kaler. A class of microstructured particles through colloidal crystallization. *Science*, 287(5461):2240, 2000.

[64] V.N. Manoharan, M.T. Elsesser, and D.J. Pine. Dense packing and symmetry in small clusters of microspheres. *Science*, 301(5632):483, 2003.

[65] R. Schirrer, P. Thepin, and G. Torres. Water absorption, swelling, rupture and salt release in salt-silicone rubber compounds. *Journal of materials science*, 27(13):3424–3434, 1992.

[66] G.D. Colo. Controlled drug release from implantable matrices based on hydrophobia polymers. *Biomaterials*, 13(12):850–856, 1992.

[67] M.W. Toepke and D.J. Beebe. PDMS absorption of small molecules and consequences in microfluidic applications. *Lab on a Chip*, 6(12):1484–1486, 2006.

[68] R. Mukhopadhyay. When PDMS isn't the best. *Analytical chemistry*, 79(9):3248–3253, 2007.

[69] G.S. Fiorini, R.M. Lorenz, J.S. Kuo, and D.T. Chiu. Rapid prototyping of thermoset polyester microfluidic devices. *Anal. Chem*, 76(16):4697–4704, 2004.

[70] L.C. Waters, S.C. Jacobson, N. Kroutchinina, J. Khandurina, R.S. Foote, and J.M. Ramsey. Microchip device for cell lysis, multiplex PCR amplification, and electrophoretic sizing. *Anal. Chem*, 70(1):158–162, 1998.

[71] J. Khandurina, T.E. McKnight, S.C. Jacobson, L.C. Waters, R.S. Foote, and J.M. Ramsey. Integrated system for rapid PCR-based DNA analysis in microfluidic devices. *Anal. Chem*, 72(13):2995–3000, 2000.

[72] E.T. Lagally, J.R. Scherer, R.G. Blazej, N.M. Toriello, B.A. Diep, M. Ramchandani, G.F. Sensabaugh, L.W. Riley, and R.A. Mathies. Integrated portable genetic analysis microsystem for pathogen/infectious disease detection. *Anal. Chem*, 76(11):3162–3170, 2004.

[73] C.W. Kan, C.P. Fredlake, E.A.S. Doherty, and A.E. Barron. DNA sequencing and genotyping in miniaturized electrophoresis systems. *Electrophoresis*, 25(21-22):3564–3588, 2004.

[74] R. Pal, M. Yang, R. Lin, BN Johnson, N. Srivastava, SZ Razzacki, KJ Chomistek, DC Heldsinger, RM Haque, VM Ugaz, et al. An integrated microfluidic device for influenza and other genetic analyses. *Lab on a Chip*, 5(10):1024–1032, 2005.

[75] V.M. Ugaz, R. Lin, N. Srivastava, D.T. Burke, and M.A. Burns. A versatile microfabricated platform for electrophoresis of double-and single-stranded DNA. *Electrophoresis*, 24(1-2):151–157, 2003.

[76] L. Koutny, D. Schmalzing, O. Salas-Solano, S. El-Difrawy, A. Adourian, S. Buonocore, K. Abbey, P. McEwan, P. Matsudaira, and D. Ehrlich. Eight hundred-base sequencing in a microfabricated electrophoretic device. *Anal. Chem*, 72(14):3388–3391, 2000.

[77] S.N. Brahmasandra, V.M. Ugaz, D.T. Burke, C.H. Mastrangelo, and M.A. Burns. Electrophoresis in microfabricated devices using photopolymerized polyacrylamide gels and electrode-defined sample injection. *Electrophoresis*, 22(2):300–311, 2001.

[78] V. Namasivayam, R. Lin, B. Johnson, S. Brahmasandra, Z. Razzacki, D.T. Burke, and M.A. Burns. Advances in on-chip photodetection for applications in miniaturized genetic analysis systems. *Journal of Micromechanics and Microengineering*, 14:81, 2004.

[79] Z. Chen and M.A. Burns. Effect of buffer flow on DNA separation in a microfabricated electrophoresis system. *Electrophoresis*, 26(24):4718–4728, 2005.

[80] O. Salas-Solano, D. Schmalzing, L. Koutny, S. Buonocore, A. Adourian, P. Matsudaira, and D. Ehrlich. Optimization of high-performance DNA sequencing on short microfabricated electrophoretic devices. *Anal. Chem*, 72(14):3129–3137, 2000.

[81] R. Rüchel, R.L. Steere, and E.F. Erbe. Transmission-electron microscopic observations of freeze-etched polyacrylamide gels. *Electrophoresis*, 166(2):563–575, 1978.

[82] F. Ikkai and M. Shibayama. Inhomogeneity control in polymer gels. *Journal of Polymer Science Part B: Polymer Physics*, 43(6):617–628, 2005.

[83] O. de Carmejane, Y. Yamaguchi, T.I. Todorov, and M.D. Morris. Three-dimensional observation of electrophoretic migration of dsDNA in semidilute hydroxy-ethylcellulose solution. *Electrophoresis*, 22(12):2433–2441, 2001.

[84] Z. Djouadi, S. Bottani, M.A. Duval, R. Siebert, H. Tricoire, and L. Valentin. Dynamics of single-stranded DNA migration in denaturing polyacrylamide slab-gel electrophoresis. *Electrophoresis*, 22(16):3527–3532, 2001.

[85] C.A. Emrich, H. Tian, I.L. Medintz, and R.A. Mathies. Microfabricated 384-lane capillary array electrophoresis bioanalyzer for ultrahigh-throughput genetic analysis. *Anal. Chem*, 74(19):5076–5083, 2002.

[86] S. Hjerten. High-performance electrophoresis:: Elimination of electroendosmosis and solute adsorption. *Journal of Chromatography A*, 347:191–198, 1985.

[87] D. Ross, M. Gaitan, and L.E. Locascio. Temperature measurement in microfluidic systems using a temperature-dependent fluorescent dye. *Anal. Chem*, 73(17):4117–4123, 2001.

[88] O.J. Lumpkin, P. Déjardin, and B.H. Zimm. Theory of gel electrophoresis of DNA. *Biopolymers*, 24(8):1573–1593, 1985.

[89] J.L. Viovy. Electrophoresis of DNA and other polyelectrolytes: Physical mechanisms. *Reviews of Modern Physics*, 72(3):813–872, 2000.

[90] O.J. Lumpkin and B.H. Zimm. Mobility of DNA in gel electrophoresis. *Biopolymers*, 21(11):2315–2316, 1982.

[91] AN Semenov, TAJ Duke, and J.L. Viovy. Gel electrophoresis of DNA in moderate fields: The effect of fluctuations. *Physical Review E*, 51(2):1520–1537, 1995.

[92] TAJ Duke, AN Semenov, and JL Viovy. Mobility of a reptating polymer. *Physical review letters*, 69(22):3260–3263, 1992.

[93] AN Semenov and AV Subbotin. Orientation effects in DNA during gel-electrophoresis. *Polymer Science USSR*, 32(6):1208–1214, 1990.

[94] AN Semenov and AV Subbotin. Mobility of deoxyribonucleic acid in a fine-pore gel in a constant electric field. *Polymer Science USSR*, 31(12):2811–2818, 1989.

[95] A.V. Subbotin and A.N. Semenov. Theory of gel electrophoresis of DNA: Orientational effects. *Electrophoresis*, 17(6):1018–1026, 1996.

[96] H.J. Kim, J.Q. Boedicker, J.W. Choi, and R.F. Ismagilov. Defined spatial structure stabilizes a synthetic multispecies bacterial community. *Proceedings of the National Academy of Sciences*, 105(47):18188, 2008.

[97] S.R. Khetani and S.N. Bhatia. Microscale culture of human liver cells for drug development. *Nature Biotechnology*, 26(1):120–126, 2007.

[98] C.T. Ho, R.Z. Lin, W.Y. Chang, H.Y. Chang, and C.H. Liu. Rapid heterogeneous liver-cell on-chip patterning via the enhanced field-induced dielectrophoresis trap. *Lab on a Chip*, 6(6):724–734, 2006.

[99] K. Chung, M.M. Crane, and H. Lu. Automated on-chip rapid microscopy, phenotyping and sorting of C. elegans. *Nature Methods*, 5(7):637–643, 2008.

[100] C.B. Rohde, F. Zeng, R. Gonzalez-Rubio, M. Angel, and M.F. Yanik. Microfluidic system for on-chip high-throughput whole-animal sorting and screening at subcellular resolution. *Proceedings of the National Academy of Sciences*, 104(35):13891, 2007.

[101] Y. Yin and Y. Xia. Self-assembly of monodispersed spherical colloids into complex aggregates with well-defined sizes, shapes, and structures. *Advanced Materials*, 13(4):267–271, 2001.

[102] A. Terray, J. Oakey, and DWM Marr. Fabrication of linear colloidal structures for microfluidic applications. *Applied Physics Letters*, 81(9):1555–1557, 2002.

[103] K.E. Sung, S.A. Vanapalli, D. Mukhija, H.A. McKay, J.M. Millunchick, M.A. Burns, and M.J. Solomon. Programmable fluidic production of microparticles with configurable anisotropy. *J. Am. Chem. Soc*, 130(4):1335–1340, 2008.

[104] T. Sawetzki, S. Rahmouni, C. Bechinger, and DWM Marr. In situ assembly of linked geometrically coupled microdevices. *Proceedings of the National Academy of Sciences*, 105(51):20141, 2008.

[105] S.M. Kim, S.H. Lee, and K.Y. Suh. Cell research with physically modified microfluidic channels: A review. *Lab on a Chip*, 8(7):1015–1023, 2008.

[106] M.C. Park, J.Y. Hur, K.W. Kwon, S.H. Park, and K.Y. Suh. Pumpless, selective docking of yeast cells inside a microfluidic channel induced by receding meniscus. *Lab on a Chip*, 6(8):988–994, 2006.

[107] KL Johnson, K. Kendall, and AD Roberts. Surface energy and the contact of elastic solids. *Proceedings of the Royal Society of London. Series A, Mathematical and Physical Sciences*, 324(1558):301–313, 1971.

[108] J.A. Champion, Y.K. Katare, and S. Mitragotri. Making polymeric micro- and nanoparticles of complex shapes. *Proceedings of the National Academy of Sciences*, 104(29):11901, 2007.

[109] S.C. Glotzer and M.J. Solomon. Anisotropy of building blocks and their assembly into complex structures. *Nature materials*, 6(8):557–562, 2007.

[110] P. Somasundaran. *Encyclopedia of surface and colloid science*, volume 3. CRC Press, 2006.

[111] D. Dendukuri, T.A. Hatton, and P.S. Doyle. Synthesis and self-assembly of amphiphilic polymeric microparticles. *Langmuir*, 23(8):4669–4674, 2007.

[112] D.B. Wolfe, R.S. Conroy, P. Garstecki, B.T. Mayers, M.A. Fischbach, K.E. Paul, M. Prentiss, and G.M. Whitesides. Dynamic control of liquid-core/liquid-cladding optical waveguides. *Proceedings of the National Academy of Sciences of the United States of America*, 101(34):12434, 2004.

[113] X. Mao, S.C.S. Lin, M.I. Lapsley, J. Shi, B.K. Juluri, and T.J. Huang. Tunable liquid gradient refractive index (l-grin) lens with two degrees of freedom. *Lab Chip*, 9(14):2050–2058, 2009.

[114] J.B. Knight, A. Vishwanath, J.P. Brody, and R.H. Austin. Hydrodynamic focusing on a silicon chip: mixing nanoliters in microseconds. *Physical Review Letters*, 80(17):3863–3866, 1998.

[115] D.E. Hertzog, X. Michalet, M. Jager, X. Kong, J.G. Santiago, S. Weiss, and O. Bakajin. Femtomole mixer for microsecond kinetic studies of protein folding. *Analytical chemistry*, 76(24):7169–7178, 2004.

[116] HA Stone and S. Kim. Microfluidics: basic issues, applications, and challenges. *AIChE Journal*, 47(6):1250–1254, 2001.

[117] S.R. Kim, H.J. Oh, J.Y. Baek, H.H. Kim, W.S. Kim, and S.H. Lee. Hydrodynamic fabrication of polymeric barcoded strips as components for parallel bio-analysis and programmable microactuation. *Lab Chip*, 5(10):1168–1172, 2005.

[118] K. Sun, Z. Wang, and X. Jiang. Modular microfluidics for gradient generation. *Lab Chip*, 8(9):1536–1543, 2008.

[119] T. Thorsen, S.J. Maerkl, and S.R. Quake. Microfluidic large-scale integration. *Science*, 298(5593):580, 2002.

[120] D.E. Hertzog, B. Ivorra, B. Mohammadi, O. Bakajin, and J.G. Santiago. Optimization of a microfluidic mixer for studying protein folding kinetics. *Analytical chemistry*, 78(13):4299–4306, 2006.

[121] S.S. White, S. Balasubramanian, D. Klenerman, and L. Ying. A simple nanomixer for single-molecule kinetics measurements. *Angewandte Chemie*, 118(45):7702–7705, 2006.

[122] E.A. Lipman, B. Schuler, O. Bakajin, and W.A. Eaton. Single-molecule measurement of protein folding kinetics. *Science*, 301(5637):1233, 2003.

[123] C.K. Chung. Geometrical pattern effect on silicon deep etching by an inductively coupled plasma system. *Journal of Micromechanics and Microengineering*, 14:656, 2004.

[124] J.O. Wilkes. *Fluid mechanics for chemical engineers/by James O. Wilkes, with contributions by Stacy G. Bike.* Prentice Hall, 1999.

[125] S.A. Rani, B. Pitts, and P.S. Stewart. Rapid diffusion of fluorescent tracers into staphylococcus epidermidis biofilms visualized by time lapse microscopy. *Antimicrobial agents and chemotherapy*, 49(2):728, 2005.

[126] A.P. Sudarsan and V.M. Ugaz. Fluid mixing in planar spiral microchannels. *Lab Chip*, 6(1):74–82, 2005.

[127] X. Mao, J.R. Waldeisen, B.K. Juluri, and T.J. Huang. Hydrodynamically tunable optofluidic cylindrical microlens. *Lab on a Chip*, 7(10):1303–1308, 2007.

[128] DR Smith, JJ Mock, AF Starr, and D. Schurig. Gradient index metamaterials. *Physical Review E*, 71(3):036609, 2005.

[129] N. Kundtz and D.R. Smith. Extreme-angle broadband metamaterial lens. *Nature Materials*, 9(2):129–132, 2009.

[130] M. Khanna, W. Cao, M. Zirvi, P. Paty, and F. Barany. Ligase detection reaction for identification of low abundance mutations. *Clinical Biochemistry-New York*, 32(4):287–290, 1999.